EXPLORATION OF $CsSnI_3$: UNCOVERING OPTICAL AND ELECTRICAL PROPERTIES FOR PHOTONIC DEVICE APPLICATIONS

by

CHONGLONG YU

A dissertation submitted to the Graduate Faculty in Physics in partial fulfillment of the requirements for the degree of Doctor of Philosophy,

The City University of New York

2013

This manuscript has been read and accepted by the
Graduate Faculty in Physics in satisfaction of the
dissertation requirement for the degree of Doctor of Philosophy.

Date	Prof. Kai Shum Chair of Examining Committee
Date	Prof. Steven Greenbaum Executive Officer

Prof. Micha Tomkiewicz

Prof. Andong Shen

Prof. Vinod M. Menon

Prof. Gregory S. Boutis

Supervision Committee

THE CITY UNIVERSITY OF NEW YORK

ABSTRACT

EXPLORATION OF $CsSnI_3$: UNCOVERING OPTICAL AND ELECTRICAL PROPERTIES FOR PHOTONIC DEVICE APPLICATIONS

By

Chonglong Yu

This thesis is about the exploration of the optical properties of perovskite compound $CsSnI_3$ (CSI), a newly identified semiconductor material. Based on what have been discovered so far, we believe that it has a great potential for photonic device applications. The exploration starts with the determination of the atomic and electronic structures of CSI and continues with the fundamental understanding of the optical properties revealed by spectroscipic measurments. One of the most fascinating optical properties associated with the unique atomic structuture of CSI is the superfluorecence from the correlated two-dimensional excitons naturally formed in the planes of SnI_4 tetragons.

After a brief introduction on the prior and recent research activities on CSI, the atomic structures and structural phase transitions of CSI were investigated using the first-principles approach. With the detailed structural information, the full electronic eigen states of CSI in its γ phase, commonly accessible by the full optical spectrum from near infrared to ultraviolet, have been calculated. A few key charcteristics of the electronic structure were identified and discussed in view of their optical consequences, such as the much larger effective mass of electrons than that of holes, and the existence of the two lowest parallel conduction bands with an energy separation of 64 meV.

In the chapters of 4, 5 and 6, the exploration continues with the understanding of interesting optical properties and the associated physics processes. The abnormal temperature dependence of the energy band gap of CSI is explained by the two combined effects: 1) the neglegible contribution of direct electron-phonon interactions to the band gap change due to the unusual large electron effective mass, and 2) the positive thermal expansion effect to the band gap change calculated by the first-principle approach. Pronounced two-LO-phonon features in both Raman scattering and photoluminescence excitation spectra are interpreted as the resonantly enhanced two-LO-phonon emission processes, originated by the unique electronic band structure of CSI: the two lowest parallel conduction bands with the energy separation close to the energy of two LO phonons.

The final part of my thesis in the chapters of 7 and 8 is devoted to the one of most exciting and abstruse phenomena in photonics: superfluorescence (SF). After revisiting Dicke's initial superradiance theory and combining the characteristics of SF, we have developed a model to capture the essential physics, especially on the dynamic time evolution of SF. This model predicts the bi-exponential decay behavior when considerable dephasing is present. Meanwhile, the intensity of SF burst, delay time, and decay rate are also studied with the model. The SF in CSI is revealed through the power and temperature dependences of time resolved photoluminescence. The measured photoluminescence characteristics are shown to match all the SF features predicted by our model, such as the bi-exponential decay, the inverse relation of delay time over the number of exciton (N), the linear relation of decay rate over N, and the temperature dependence of decay rate. The natural formation of two dimensional excitons in the parallel planes of SnI_4 tetragons is argued to be the reason for the SF to occur in CSI.

ACKNOWLEDGEMENTS

Looking back to the last five years study pursuing my Ph.D. degree in Physics at the City University of New York, I want to give my special gratitude to my adviser, Prof. Kai Shum. Without his patient guidance and mentoring, there is no way for me to complete this dissertation and finish the Ph.D. program. I always felt lucky to work with Prof. Shum, who has both broad intensive knowledge in the semiconductor field and sharp sense of physics for experimental data. I still remember the clear introductions from him when I just joined his research group, the detailed modifications and patient guidance for my first paper, and the encouragements and insightful suggestions whenever I got stuck in my research work.

I want to give my special thanks to our group member, Zhuo Chen, for teaching me how to operate all the experimental apparatuses in our laboratories. I appreciate his useful suggestions, hands-on helps, and especially, his friendship.

I also want to thank Dr. Cai Wei and Prof. Yuhang Ren for all the useful discussions. I would like to acknowledge the committee members for both my second exam and final defense: Prof. Micha Tomkiewicz, Prof. Aidong Shen, Prof. Vinod M. Menon, Prof. Gregory S. Boutis, Prof. Igor L. Kuskovsky, and Dr Jim Wang. I would also express my appreciation to Dr. Piao Liu and Dr. Jawad Qureshi for their assistance during my thesis work.

Finally, I want to thank all the love and support from my family, particularly, my wife Chuan Wang. She is always there with me going through all the joys and frustrations in my Ph.D. study.

Contents

List of Tables

List of Figures

CHAPTER 1: Introduction

1.1 Prior research activities on $CsSnI_3$

$CsSnI_3$ (CSI) belongs to a family of perovskite crystals with the chemical formula of ABX_3. It consists of a network of BX_6 octahedra, where the B atom is a metal cation, X is a mono-valent anion, and the cation A is incorporated to balance the total charge, stabilizing the structure. The schematic diagram of CSI crystal is shown as in Fig. 1.1. An early study on the structural information of $CsSnI_3$ compound in form of powders was reported by Scaife *et al* [1] in 1974. A few years later, a yellow, needle-like $CsSnI_3$ microcrystal was synthesized and its crystal structure was independently studied by Mauersberger and Huber [2]. The BX_6 octahedrons of yellow CSI are edge-connected, while those of black CSI are corner-linked. No additional information was available until the discovery of three sub-phases (α, β, and γ) of black CSI in 1991 by Yamada et al [3]. After this work, the research on $CsSnI_3$ had no progress and the electrical and optical properties of CSI held back due to the lack of high quality samples in bulk or thin-film form. Recently, it was reported by our group in 2010 that the high-quality thin films of $CsSnI_3$ were synthesized by the evaporation method [4]. This was the first time that $CsSnI_3$ was confirmed to be a direct band-gap semiconductor.

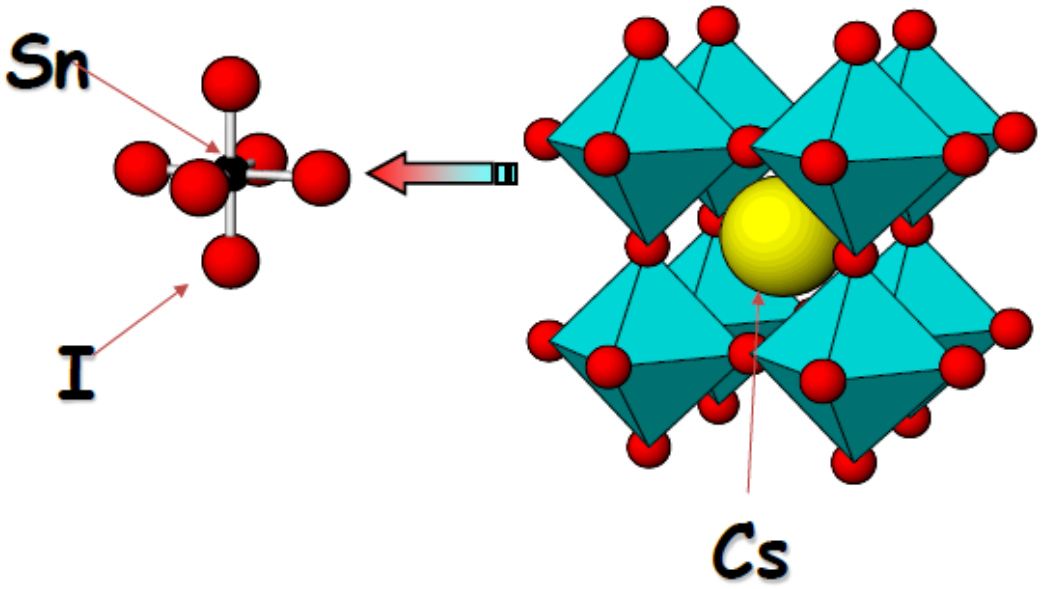

Fig. 1.1 Schematic structure of $CsSnI_3$ is shown. Cs atom (yellow) is in the center of eight octahedra, each of them is formed by one Sn atom (black) and six I atoms (red).

1.2 Motivation of our research on $CsSnI_3$

New materials have been the key drivers to the innovation and development of science and technology. The discovery and developments of various semiconductors in the past several decades have been the basis of the "digital age". The Si-based integrated circuit is the fundamental component in almost all the electronics in the modern world. The success of epitaxially grown GaAs-, InP-, and GaN-based nanostructures has led to many different applications such as semiconductor lasers, light-emitting diodes (LED), modulators, waveguides, planar light-wave circuits, and integrated photonic circuits. These devices form the foundation for the modern telecommunication industry as well as other developing industries such as solid state lighting and solar energy conversion. Therefore, the discovery and research of new semiconductor materials is crucial in technological innovations.

Semiconductors also play increasingly important roles in solving the energy crisis that is due to the accelerated depletion of the limited resources such as coal, oil, and natural gas. Photovoltaic energy conversion panels generate free electricity by converting the sunlight into electricity. The use of solar panels to generate energy provides many benefits, which include reductions in the costs associated with generating electricity. Solar panels also provide pollution-free power sources. The semiconductor in solar cells absorbs the sun light and converts photons to electron-hole pairs that are then separated by the internal filed of the p-n junction. One of the most important criterions for evaluating a solar cell is the efficiency. With higher efficiency, the solar cells could generate more electricity with fewer panels, and thus reducing the installation cost, which is one of the major expenses in the application of solar cells. Many research teams around the world are working on improving solar cell efficiency — within universities, governmental research institutes, and companies. To achieve high efficiency of solar cells, the semiconductor chosen for a solar cell has to absorb as many photons as possible in the full solar spectrum to generate photocurrent; therefore, a low band gap is desirable. On the other hand, the build-in voltage determined by the band gap is desired to be as large as possible, requiring a large band-gap material. The trade-off criteria between the absorption efficiency and build-in voltage leads to the discovery of the optimum band gap of 1.3 - 1.35 eV and maximum theoretical efficiency 33% for a perfect single p-n junction solar cell. This maximum efficiency is referred as the Shockley Queisser (SQ) Limit, as it was first calculated by William Shockley and Hans Queisser in 1961.

The records for all kinds of solar cell efficiency achieved in laboratories are shown as in Fig. 1.2. According to the graph, substantial progress has been made on the traditional Si-based solar cells, the thin-film solar cells, as wells as the multi-junction solar cells. The best efficiency for single junction Si-based solar cells is 27.6%. However, the upward potential is limited because of the relatively low band gap (1.1 eV). Although crystalline Si is

currently the dominant material for making solar cells, new solar cells using thin films have been emerging due to their high competitiveness in cost reduction, as shown in the Fig. 1.2 that the efficiency records for the emerging solar cells improves greatly in the past decade. New and transformative materials have also gained lots of attentions lately, for instance, assemblies composed of quantum dots and/or wires in which quantum confinement is used as a design parameter. Dye-sensitized solar cell and organic PVs are also being pursued as affordable and low-cost solutions. Therefore, new suitable materials for solar cells are of great interest in both academic and industrial arena.

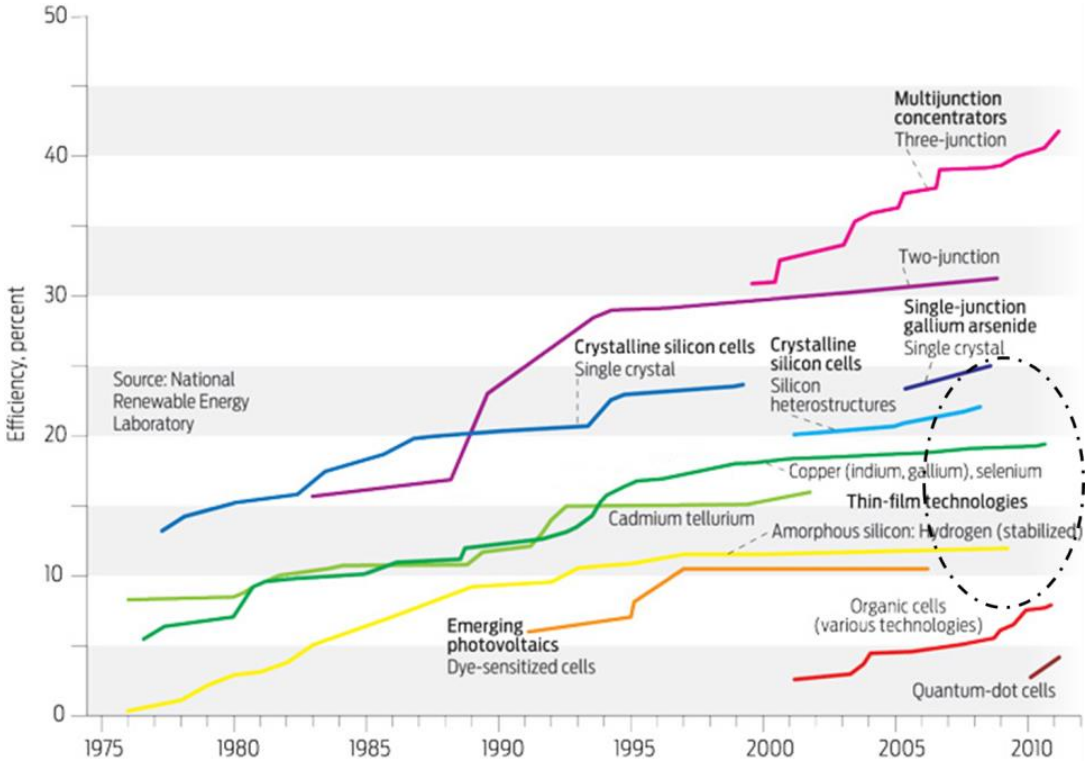

Fig. 1.2: Solar cell efficiencies achieved in laboratory over time by NREL. The black circle represents for the place where the solar cells based on CSI could be.

In our preliminary study of the $CsSnI_3$ material, we measured extraordinarily strong photoluminescence (PL) signal peaked at 950 nm at room temperature. We further identified that $CsSnI_3$ possesses a direct band-gap of 1.32 eV at room temperature, right in the narrow region of optimal band gaps for the Shockley-Queisser maximum efficiency limit of a solar

cell. Meanwhile, $CsSnI_3$ thin films can be inexpensively synthesized onto various large-area substrates, such as glass and plastics, through its intrinsic characteristics of self-assembly and self-limiting instead of using expensive epitaxial growth technologies, such as molecular beam epitaxy (MBE) and metal-organic chemical vapor deposition (MOCVD). This is huge advantage in the large scale industrial production. Our research in $CsSnI_3$ may be helpful in producing the next generation of solar cells based on $CsSnI_3$. The place of the anticipated energy conversion efficiencies are shown within the black circle in Fig. 1.2 for polycrystalline CSI thin film based solar cells. Recently the all solid dye-sensitized solar cell using CSI as a hole-conduction material was reported with the efficiency of 10.2 percent [5].

Besides the great potential for the application in solar cells, it may find other applications such as light-emitting diodes and sensitive photo-detectors. We have surveyed more than one hundred materials, including single crystalline (epitaxial) semiconductors such as InGaAs/GaAs multiple quantum wells (MQWs), GaAs/AlGaAs MQWs, InP, CdTe, poly-crystalline semiconductors, powders, and organic-inorganic hybrid materials, and we have not found any other material which gives comparable PL efficiency in the wavelength range of 900 to 1100 nm. The closest one is a 2" InP wafer doped with Sulfur (resistivity ~ 10^{-3} ohm-cm with an electron density of ~ 2×10^{18} cm^{-3}), which has only about 0.2 % of the PL intensity of that of a typical $CsSnI_3$ film on glass substrate as shown in Fig. 1.3 under the same excitation and PL collection conditions.

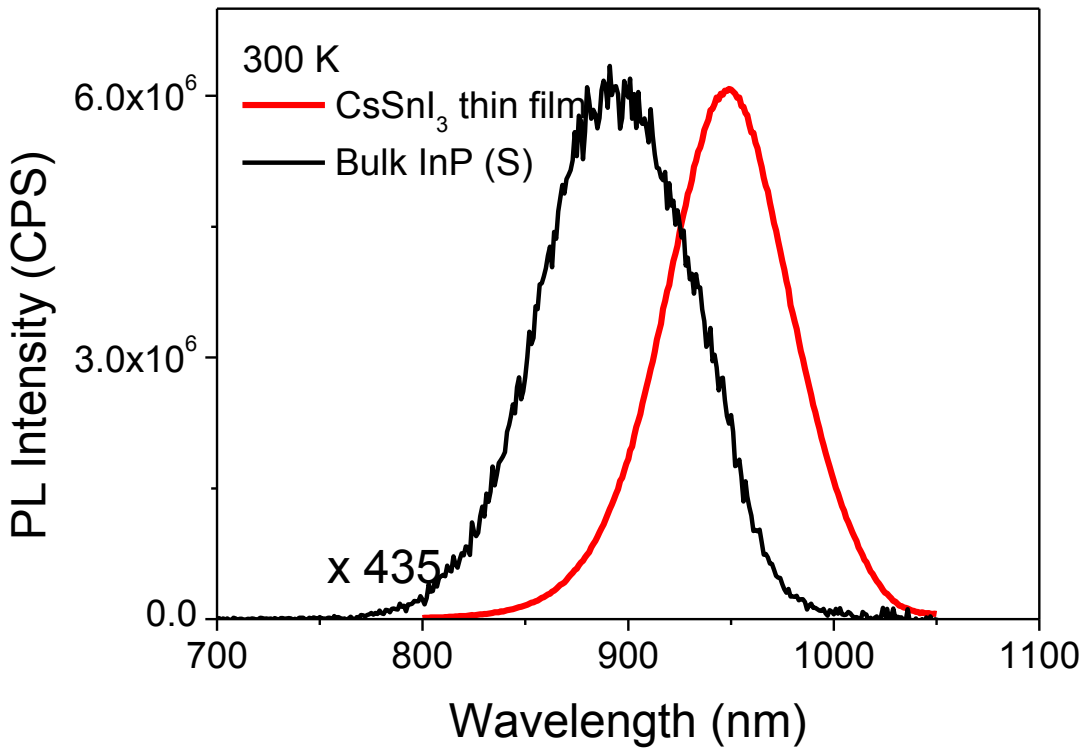

Fig. 1.3 PL spectra from a n-type InP(S) sample and a $CsSnI_3$ film on glass substrate at 300 K. Excitation source was a Xe lamp with power density of ~ 20 mW/cm² at 500 nm with bandwidth of 5 nm selected by the excitation spectrometer. Same detector (Hamamatsu PMT R2658P) was used.

In summary, the excitement of exploring new materials, the great potential in application of $CsSnI_3$ based solar cells, and the interesting optical properties have motivated me to focus my research on the exploration of this material. I expect my work on the interesting properties of $CsSnI_3$ will attract more attentions from the semiconductor community to push the exploration of $CsSnI_3$ forward.

1.3 Recent research activities on $CsSnI_3$

After our first paper on the synthesis and characterization of $CsSnI_3$ thin film, there have been some exciting progresses in the research and application of CSI. In 2012, Chung *et al.* fabricated [5] the all solid state dye-sensitized solar cells using CSI, and achieved energy conversion efficiencies of up to 10.2 percent. The CSI is suitable as a hole-conductor in this type of solar cell because of the direct band gap 1.3 eV and the remarkably high hole-mobility of 585 $cm^2V^{-1}s^{-1}$ at room temperature.

Meanwhile, the research of CSI has also inspired to explore other perovskite materials with similar structures. Cs atoms could be replaced by some organic structures such as CH_3NH_3, Sn atoms could be replaced with Pb, Cd, and I atoms could be replaced by Br, Cl, and F. The inorganic-organic hybrid hetero-junction solar cells containing the inorganic-organic compound $CH_3NH_3PbI_3$ were successfully fabricated with a cell efficiency of 12%. Just a few months ago, the solar cell efficiency of $CH_3NH_3PbI_3$ has reached to 15% [6].

Topological materials, either insulators or semiconductors, are becoming one of the most studied classes of novel materials because of their great potential for applications ranging from spintronics to quantum computers. Recently, a search model for identifying TI developed by Kesong Yang *et al.* [7] has suggested that CSI is a good candidate that may behave as a topological semiconductor.

1.4 Brief summary on the synthesis of $CsSnI_3$

The first synthesis method of CSI was reported by Scaife et al in 1974 [1]. The CSI single crystal was obtained in a silica tube using an equimolar amount of SnI_2 and CsI by the method of the Bridgman technique. The products were lustrous black power. No major progress of synthesis method of CSI has been reported until the discovery of the vacuum-based evaporation method of producing CSI thin film by our group in 2010 [4]. Besides the evaporation method, other synthesis method of CSI, such as the solution based method and solution-sintering hybrid method have also been developed by our group. The detailed descriptions of all the methods have been included in the thesis of the other graduate student of our group, Zhuo Chen. In this thesis, the CSI thin film samples were synthesized by the evaporation method which is briefly introduced in the next paragraph.

The evaporation method uses a typical two-step approach that includes the production of the material precursors separately and a following heat treatment. This method allows us to get a better control at each step. High-purity (99.99% purity) multiple layers of SnI_2 and CsI are deposited in vacuum (~10^{-5} Torr) on glass, ceramic, silicon or other substrates by a combination of thermal and e-beam evaporators, respectively. The design of the multiple layers is to make sure that SnI_2 and CsI could fully react during an annealing process. The CsI power has to be compressed into pellets to avoid being scattered around by the electron beam. The optimum thickness of SnI_2 and CsI is determined to be 130 nm and 150 nm, after tremendous amount of trials with the samples quality checked by PL and SEM. Six layers of CsI/SnI_2 with total thickness around 800 nm are deposited with the deposition speed 5 Å per second.

The cross section of the CSI thin film deposited on a ceramic substrate using evaporation method is shown in Fig. 1.4. The domain size of the CSI thin film is typically 300 nm. We are still developing new synthesis method of CSI to overcome some quality issues of our CSI

samples, such as the instability problem. The latest CSI sample synthesized by the solution-sintering hybrid technique is shown as in Fig. 1.5.

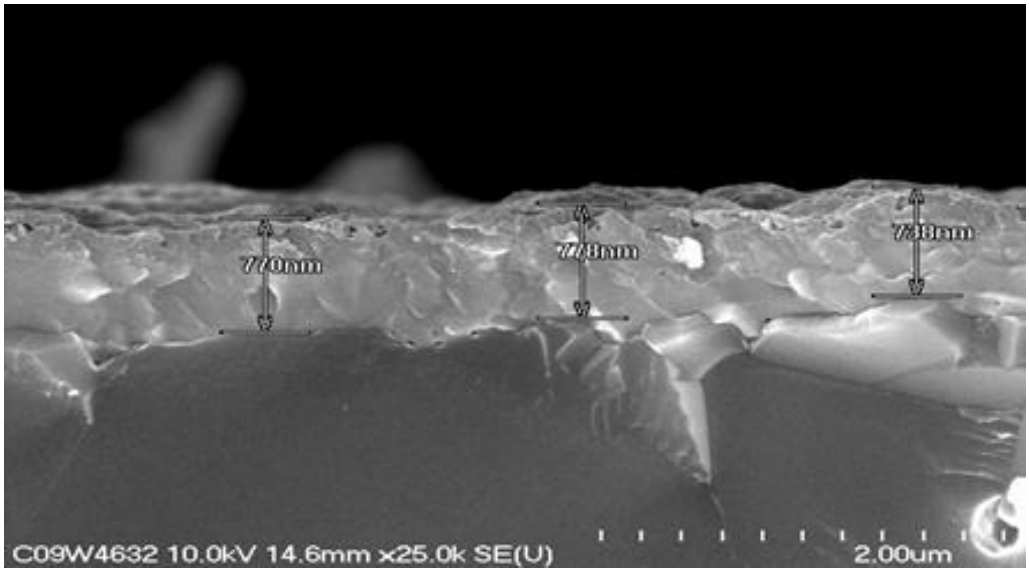

Fig. 1.4 Polycrystalline CSI thin film deposited on a ceramic substrate, showing grains with typical size of 300 nm.

Fig. 1.5 Photo is shown above for a polycrystalline CSI ingot which was synthesized by the sintering technique.

1.5 Scope of the dissertation

In this chapter, the background research information on CSI has been introduced. The rest of chapters of my thesis are briefly described below.

In chapter 2, the atomic structure and structural phase transitions of black CSI are investigated using the first principles approach.

In chapter 3, the electronic band structure of CSI is presented.

In chapter 4, the abnormal temperature dependence of the band gap is interpreted. The combined contribution of electron-phonon interaction and thermal expansion to the band gap change is discussed.

In chapter 5, the extraordinary large second-order Raman scattering efficiency is explained. I will show how the unique band structure results in the resonantly enhanced second order Raman scattering process.

In chapter 6, the photoluminescence excitation (PLE) spectrum of CSI is studied. The two-LO-phonon feature in the PLE spectrum is identified and closely related to the electronic conduction band structure of CSI.

In chapter 7, our model of the time evolution for superfluorescence is presented.

In chapter 8, the evidences of the superfluorescence in CSI are given through power and temperature dependence of time resolved photoluminescence. The experimental data is compared with the theoretical prediction using our model described in chapter 7.

Finally, chapter 9 presents a few conclusions of this dissertation.

Chapter 2: Atomic structural phase transitions of black CSI studied by first-principles calculations

2.1 Current understanding of CSI structure and phase transitions

$CsSnI_3$ is known to have two types of polymorph: yellow and black CSI, which are named because of the appearance of their respective colors. The SnI_6 octahedrons of yellow CSI are edge-connected, while those of black CSI are corner-linked. The black CSI consists of three sub-phases: α phase with cubic structure (space group Pm3m), β phase with tetragonal structure (space group P4/mbm), and γ phase with orthorhombic structure (space group Pnam). The phase transitions from α to β, and from β to γ were experimentally studied using the temperature dependence of XRD and the DTA analysis in 1991 by Yamada et al [3]. Their research work suggests that the yellow phase CSI can be transformed to the black CSI at high temperature above 450 ^{o}K. During the cooling process, the black CSI undergoes a phase transition from α to β phase at 425 ^{o}K, followed by another transition from β to γ phase at 351 ^{o}K. This kind of phase transitions in CSI is typical, as similar phase transitions have been observed experimentally in other ABX_3 perovskite materials. For example, $CaSiO_3$ was reported to have a phase transition from cubic to tetragonal structure under high pressure over 20 Gpa. More similarly, the space group and crystal structure of $CaTiO_3$ undergoes transitions from cubic to tetragonal, and finally to orthorhombic structure with decreasing temperature. Even though there are plenty of observations of the phase transitions [8-10], the underlying mechanisms and transition pathways, have not been fully understood.

In this chapter, we use the first-principles calculations to reveal the phase transition mechanisms for the three sub-phases of black CSI. There has been no theoretical treatment of the phase transitions in CSI, due to the difficulty of mathematical representation of the

transition pathway that relates to the detailed coordinates of all atoms during transition processes. The complexity of the orthorhombic unit cell containing 20 atoms also increases the difficulty. The rest of the chapter is organized as follows: A model for the CSI crystal structure is presented which describes the transition pathway under the assumption that the SnI6 octahedra in CSI remain regular during the phase transition processes, briefly followed by a description of our computation method. The calculated results are then discussed on the minimized total energy per unit cell at each intermediate state and the detailed unit cell coordinates of α, β, and γ phase crystal structure are identified and compared with available experimental data. And finally, the transition mechanisms associated with the lattice expansion/contraction and Cs position offsets are further elucidated.

2.2 Crystal structure of black CSI phases and Computation method

In order to relatively compare the minimum total energy per unit cell among α, β, and γ phases, as well as the transition intermediate states, we use the 20-atom orthorhombic structure with space group Pnam to represent all the states. The unit cell is shown as Fig. 2.1 (a). There are two distinct positions for I atoms, as labeled as I_1 and I_2, and we define the bond angle of Sn-I_1-Sn as θ_{xy} and the Sn-I_2-Sn bond angle as θ_z. To represent the α structure in the 20-atom basis, the angles of θ_{xy} and θ_z must equal to 180^o since there is no distortion of the SnI_6 octahedral structure. In addition, the lattice constant follows: $a = b = \frac{\sqrt{2}}{2} c$ **;** one of the coordinates for I_1 and I_2 are(0.75, 0.25, 0), (0.5, 0, 0.25) respectively, and the rest of I coordinates could then be determined by the Pnam symmetry. The Cs atom is at the center of the surrounding eight SnI_6 octahedrons. With these conditions satisfied, we can visualize the cubic unit cell inside the 20-atom basis, as shown in Fig. 2.1 (b). The unit cell of α structure

consists of 5 atoms: 1 Cs, 1 Sn, and 3 I atoms, so each 20-atom basis contains four α unit cells. The β structure can be also represented in the 20-atom basis in the same way. The conditions and coordinates of α, β, and γ in the 20-atom basis are presented in Table 1.

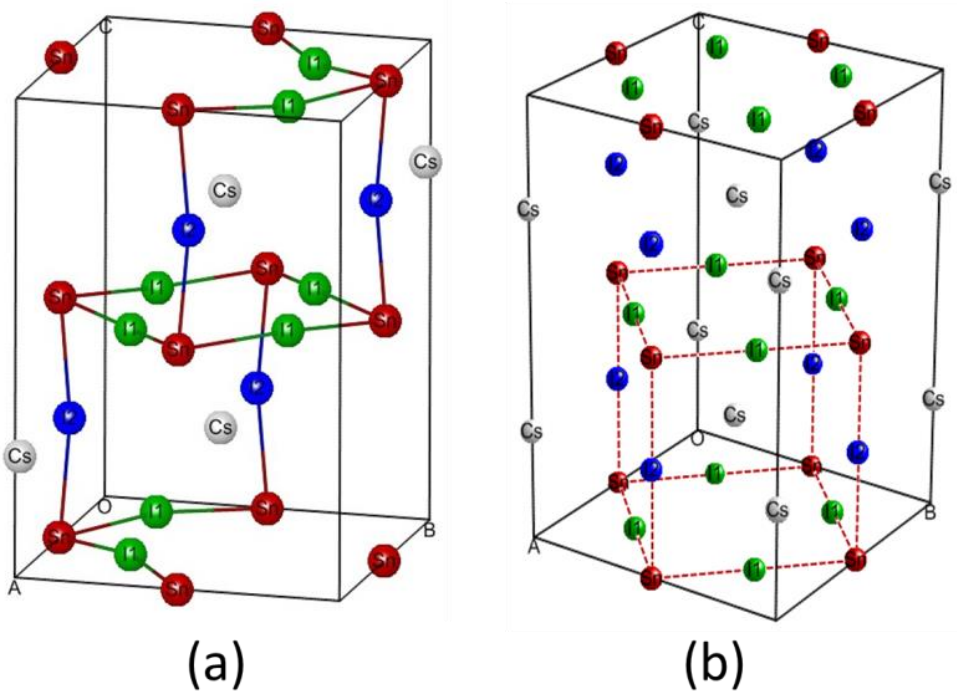

Fig.2.1 (a) 20-atom orthorhombic structure with space group Pnam is shown. The bonds between Sn and I within the unit cell are depicted. The bond angle of Sn-I_2-Sn is denoted as θ_z, while Sn-I_1-Sn as θ_{xy}, respectively. (b) The unit cell for α structure is illustrated in orthorhombic structure with θ_{xy} and θ_z both equals to 180^o.

Since each β unit cell consists of 10 atoms, each 20-atom basis contains two β unit cells. In this treatment, we can compare the total energy per unit cell for the three different phases under the same calculation framework.

The next step is to mathematically model the general 20-atom basis, so that we could input the structure parameters into our calculation software tool to be discussed later. There are ten undetermined parameters as given in Table 1. These are: seven deviations of I_1, I_2, and

Cs coordinates (x, y, z, u, v, CsX, and CsY) and there lattice constants of the unit cell *a*, *b*, and *c*.

Phase	**α**	**β**	**γ**
θ_z and θ_{xy}	$\theta_z = 180^o$,	$\theta_z = 180^o$,	**$\theta_z \neq 180^o$**
	$\theta_{xy} = 180^o$	$\theta_{xy} \neq 180^o$	**$\theta_{xy} \neq 180^o$**
Lattice Constant	$a = b = \frac{\sqrt{2}}{2}c$	$a = b \neq \frac{\sqrt{2}}{2}c$	**$a \neq b \neq \frac{\sqrt{2}}{2}c$**
Cs	(0, 0, 0.25)	(0, 0, 0.25)	**(CsX, CsY, 0.25)**
Sn	(0, 0.5, 0)	(0, 0.5, 0)	**(0, 0.5, 0)**
I_1	(0.75, 0.25, 0)	(x, y, 0)	**(x, y, z)**
I_2	(0.5, 0, 0.25)	(u, v, 0.25)	**(u, v, 0.25)**

Table 1 The detailed structure parameters of α, β and γ phase in the 20-atom orthorhombic structure.

To simplify the calculation, we use the assumption that the SnI_6 octahedra remain regular shape for all the intermediate states, while the size of SnI_6 octahedra could be scaled with lattice constants. This assumption is consistent with the experimental observation of phase transitions observed by Yamada *et al* [3]. It is also common in other ABX_3 materials, such as $YMnO_3$, $LaMnO_3$ [11] and organic-inorganic perovskites [12].We use a set of bond angle of θ_{xy} and θ_z to represent each intermediate states. When θ_{xy} and θ_z both equals to 180^o, the unit cell represents the α structure. And if $\theta_z = 180^o$ and $\theta_{xy} \neq 180^o$, the unit cell represents the β structure. To further modeling the 20-atom basis, we need to derive the coordinates of I_1 and I_2 in terms of θ_{xy} and θ_z based on the assumption that all SnI_6 remain regular. Let *b/a* = m, *c/a* = n, and treat θ_{xy} and θ_z as known variables, the following two expressions are then derived:

$$\cos\theta_{xy} = \frac{(x-0.5)(x-1)+m^2y(y-0.5)+n^2z^2}{\sqrt{(x-0.5)^2+m^2y^2+n^2z^2}\times\sqrt{(x-1)^2+m^2(y-0.5)^2+n^2z^2}} \quad (2.1)$$

$$\cos\theta_z = \frac{(u-0.5)^2+m^2v^2-n^20.25^2}{(u-0.5)^2+m^2v^2+n^20.25^2} \quad (2.2)$$

Based on our assumption that the SnI_6 octahedra will maintain regular during phase transition processes, we can get the following five equations. The requirement of bond angle of I_1-Sn-I_1 in x-y plan to be 90^o gives rise to:

$$(x-1)(x-0.5)+m^2y(y-0.5)+n^2z^2=0 \quad (2.3)$$

The fact that the length of all Sn-I bond remains equal gives rise to：

$$(x-0.5)^2+m^2y^2+n^2z^2=(x-1)^2+m^2(y-0.5)^2+n^2z^2 \quad (2.4)$$

$$(x-0.5)^2+m^2y^2+n^2z^2=(u-0.5)^2+m^2v^2+0.25^2n^2 \quad (2.5)$$

Another requirement of the bond angle of I_2-Sn-I_1 to be 90^o gives rise to:

$$(u-0.5)(x-0.5)+m^2vy+0.25n^2z=0 \quad (2.6)$$

$$(u-0.5)(x-1)+m^2v(0.5-y)+0.25n^2z=0 \quad (2.7)$$

By solving these seven equations, we can express *x*, *y*, *z*, *u*, *v*, *m*, and *n* in terms of θ_{XY} and θ_Z. In particular, the relations of *m* and *n* are given by $m=\sqrt{(1-\cos\theta_z)/2}$, and $n=\sqrt{\frac{(1-\cos\theta_z)(3-\cos\theta_z)}{2(1-\cos\theta_{xy})}}$, respectively. It should be emphasized that not all states could have solutions to these seven equations, only an angle set that satisfies the condition of $m^2+\cos\theta_{xy}\geq 0$ will lead to the CSI crystal structures with regular SnI_6 octahedra.

For each bond angle set of θ_{xy} and θ_z, we can determine the coordinates of I_1 and I_2, as well as the ratios (m and n) between lattice constants. However, in order to get the full description of the unit cell, we still need two more factors to fully count for ten variables: a scaling factor and the coordinates of Cs. We use the lattice constant *c* as the scaling factor. Lattice constants of *a, b* could then be determined using *m* and *n*. To get the minimum total energy for each bond angle set of (θ_{xy}, θ_z), we need to compare the total energy of the 20-atom unit cell with different scaling factors and Cs coordinates. This is accomplished in our calculation by the following two steps. First, we take the Cs position offsets as zero and calculate the 20-atom unit cell total energy with various lattice constant *c*. In this case, we find the optimum lattice constant at which the total energy per unit cell is at a minimum for each bond angle set. Second, we change the Cs position offsets of CsX and CsY, and fix the scaling factor to be the optimum lattice constant. Therefore, for each bond angle set of (θ_{xy}, θ_z), by changing scaling factor and Cs atom offset, we will be able to find the minimum total energy for that state. Additionally, we have found that the effect of lattice scaling factor and Cs position offset on the minimum total energy is independent in the range of interest: lattice constant *c* from 12.1 to 12.6 Å and Cs position offset from - 0.05 to 0.05 Å. This independence between lattice constant and Cs offset effect justifies our calculation treatment.

All the calculations were performed with the CASTEP simulation tool [13], which is based on the density function theory. The Perdew−Burke−Ernzerhof (PBE) parameterization of the generalized gradient approximation (GGA) was employed, and core-valence electron interactions were described using Troullier-Martin [14] norm-conserving pseudo-potentials. The cutoff for the plane wave basis was 400 eV and a $3\times \mathbf{3} \times \mathbf{2}$ Monkhorst-Pack grid [15] was chosen for sampling the Brillouin Zone.

2.3 Minimum total energy per unit cell

The minimum total energies per unit cell at a set of possible bond angles have been calculated and are plotted in Fig. 2.2. The calculation reflects quantum-mechanically permitted atomic arrangements at zero temperature. However, any higher temperature effect could not be included. At zero temperature, each intermediate state is frozen at its minimum energy state. As mentioned earlier, for some bond angle sets, there is no solution under the assumption of regular octahedral structure. These bond angle sets are schematically confined in the flat area in Fig. 2.2 where the energy is artificially set to be 50 meV just for the visualization purpose. Inspecting the Fig. 2.2, we can identify the lowest energy state to be the γ state at zero temperature. The energy of this state is set to be zero as a reference. The α state corresponds to the angle set of (180^o, 180^o), and has the highest relative energy. Starting from the α state, the system could be smoothly transferred to the β state, which is the minimum energy state with $\theta_z = 180^o$. The angle set for β state is (163^o, 180^o). From the β state, the unit cell could be gradually deformed to the γ state, which corresponds to the angle set of (163^o, 168^o). This theoretical result is consistent with the experimental observation that the yellow CSI once heated to 450 ^{o}K could be transferred to α, then to β, and finally to γ state with decreasing temperature. The energy difference between the α and β state is ~ 35 meV, while the energy of the β state is 7 meV higher than that of the γ state. The energy differences suggest that it is much easier for the phase transition to occur from the γ to β state than from the β to α state.

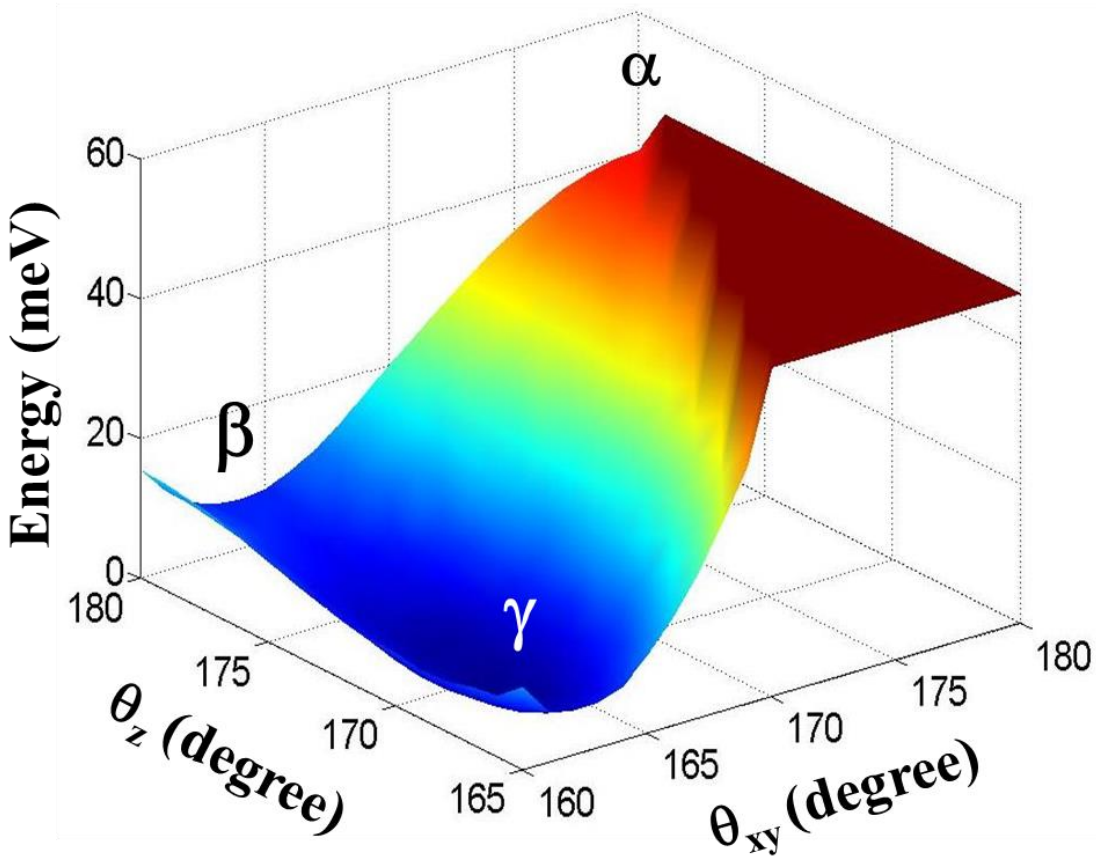

Fig. 2.2: The minimum total energy per unit cell of the 20-atom structure is displayed as a function of (θ_{xy}, θ_z) at zero temperature. The zero energy reference is set at the γ state and a hard limit of 50 meV is used for the bond angles in which there are not stable states.

With the results of minimum total energy for all the bond angle sets, we are able to determine the detailed coordinates of the 20-atom unit cell for all the three states and to compare with experimental values from the work of Yamada *et al.*[13] In the Table 2, the experimental data are arranged in the 20-atom basis. The calculated α and β structures are very consistent with the experimental data, which were extracted from high temperature XRD. It suggests that the coordinates and the value θ_{xy} for the β structure remain almost unchanged from zero to high temperatures. The difference in the lattice constants might be due to the thermal expansion effect. Since the experimental data were obtained at 370 ^{o}K, the linear thermal expansion coefficient can be estimated to be 2.97×10^{-5}, which is reasonable for a perovskite material.[5]

The ratio of *c/a* for the experimental lattice constant is equal to 1.427 (multiplied by two to be consistent with 20-atom basis). This value deviated by 0.35% from the theoretical predication of *c/a* = 1.432 for $\theta_{xy}=162^o$ and $\theta_z=180^o$ based on the mathematical derivation earlier. The agreement in lattice constants validates our assumption that the SnI_6 octahedral structure remains regular during phase transition. For the γ structure, there are some discrepancies between the calculated and experimental results. As shown in Fig. 2.2, the γ state is relatively "flat", i.e. the energy difference between the γ and its surrounding states is within a few meV. As a result, when the temperature increases, it is much easier for the γ state to deviate from the original zero-temperature γ state. Our calculation also shows that the Cs atom moves away from its original position (0, 0, 0.25) during the transition from the β to γ state.

		α phase	β phase	γ phase
Space Group		Pm3m	P4/mbm	Pnam
Crystal Structure		Cubic	Tetragonal	Orthorhombic
Angle Set (θ_{xy}, θ_z)	Calculation	$\theta_{xy} = \theta_z = 180^o$	$\theta_{xy} = 163^o$	$\theta_{xy} = 163^o$ $\theta_z = 168^o$
	Experiment	$\theta_{xy} = \theta_z = 180^o$	$\theta_{xy} = 161.9^o$	$\theta_{xy} = 158^o$ $\theta_z = 172^o$
Lattice Constant (Å)	Calculation	a = 6.154	a = 8.661 c = 6.192	a = 8.703 b = 8.655 c = 12.342
	Experiment	a = 6.219	a = 8.772 c = 6.261	a = 8.688 b = 8.643 c = 12.378
Cs	Calculation	(0, 0, 0.25)	(0, 0, 0.25)	(-0.03, 0.008, 0.25)
	Experiment	(0, 0, 0.25)	(0, 0, 0.25)	(-0.04, 0.006, 0.25)
I_1	Calculation	(0.75,0.25, 0)	(0.713,0.287, 0)	(0.719, 0.281, 0.019)
	Experiment	(0.75,0.25,0)	(0.710,0.290, 0)	(0.705, 0.295, 0.019)
I_2	Calculation	(0.5, 0, 0.25)	(0.5, 0, 0.25)	(0.505, -0.037, 0.25)
	Experiment	(0.5, 0, 0.25)	(0.5, 0, 0.25)	(0.476, 0, 0.25)

Table 2 The structure parameters for α, β, and γ phases determined by our calculations are compared with experimental data [3].

2.4 Confirmation of structure information by XRD

The X-ray diffraction (XRD) spectra are used to verify the crystal structure of CSI. We compare the XRD experimental data with the theoretical prediction to confirm the crystal structure and product of reaction, as shown in Fig. 2.3. The theoretical calculation of XRD profile shown as Fig. 2.3 c) was obtained using the "CRYSTALMAKER" simulation package. The inputted detailed structure information of γ structure was determined by the total energy per unit cell calculation as presented in Table 2. The peak number "1", "2" and "3" represents for the XRD features of the Sn-I-Sn bond tilting in the horizontal direction (x and y direction) and vertical direction (z direction). The measured X-ray diffraction data from a sample synthesized by vacuum method using CsI/SnI_2 raw material on ceramics substrate is shown as in Fig. 3.6 a). The XRD peaks from the ceramics substrate are removed for clarity. The measured data matches the main features (peak "1", "2" and "3") well with that of the theoretical calculation. This further confirms that the calculated detailed information of γ structure CSI that is input in the calculation software is in good agreement with experiments. We also take the X-ray measurement for the solution-based CSI film drop coated on a ceramic substrate, as shown in Fig. 3.6 b). Besides the black CSI identified (peak "1", "2" and "3"), other residue reactant and side products are identified, such as residue CsI (peak "4"and "5"), side product CsCl (peak "6"and "7") and SnO_2 (peak "8"and "9"). The side product confirms the reaction described as $3CsI + SnCl_2 \rightarrow CsSnI_3 + 2CsCl$. The present of SnO_2 indicates that some $SnCl_2$ is oxidized in the present of water.

The XRD study further validates the theoretical structure of γ structure CSI obtained in Table 2. It also verified the reaction product to be γ structure CSI for the vacuum based and solution based method.

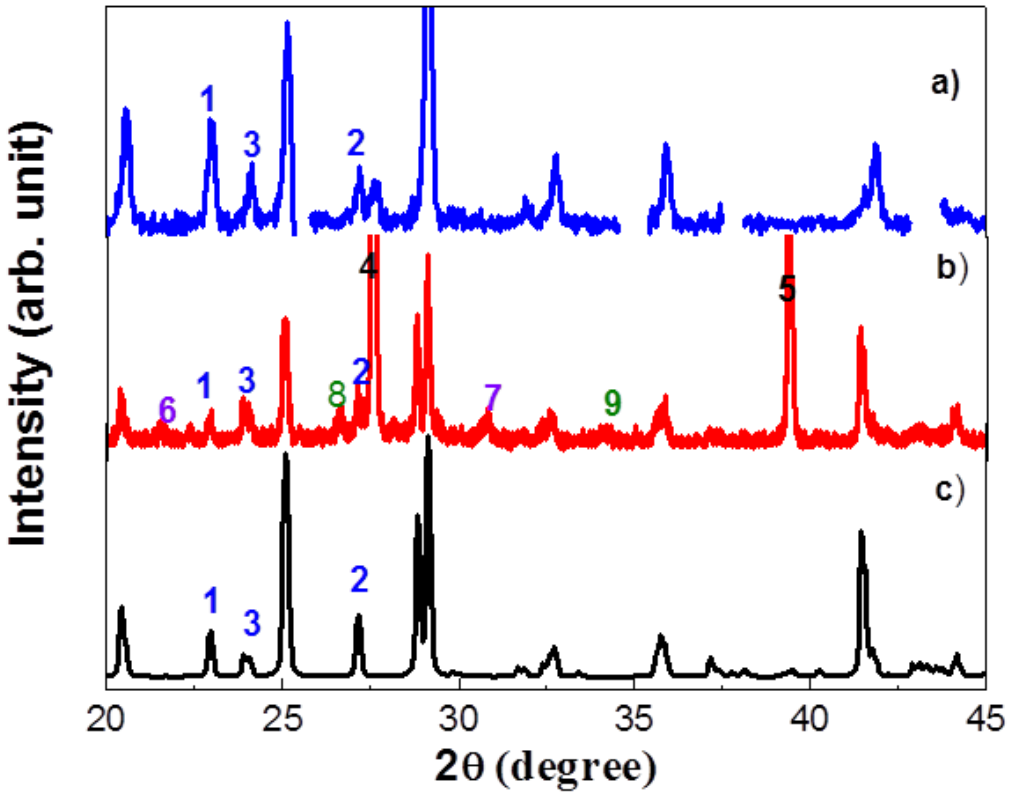

Fig. 2.3: The X-ray diffraction profile for a) vacuum-based CSI using CsI/SnI2 on ceramics substrate. The XRD peaks from the ceramics substrate are removed for clarity; b) solution-based CSI product. Residue reactant and side products are also identified. c) Calculated XRD structure of γ structure CSI, which is identified through the total energy per unit cell analysis. The peak number "1", "2" and "3" represents for the XRD features of the Sn-I-Sn bond tilting in the x, y, and z direction respectively.

2.5 The role of lattice constant

Since we cannot directly take temperature effects into account using the first-principles calculations, in order to reveal the mechanisms of phase transition processes, we consider the changes of lattice constant and Cs position offsets in these two sections to investigate the role of each of them in the phase transition processes. Besides the observed phase transitions with decreasing temperature, we also investigate the reverse phase transition with increasing temperature starting from the γ state.

The variation of lattice constant is closely related to temperature, usually known as thermal expansion as temperature increases and contraction as it decreases. Thus, the change of lattice constant at the vicinity of minimum total energy per unit cell could be used as a useful indicator for the structure phase change as temperature changes. The optimum lattice constant at which the crystal structure is at the minimum energy is displayed in Fig. 2.4 for each transitional state from the β to γ state. It decreases from the β to γ state as the vertical bond angle of Sn-I_2-Sn decreases from 180^o to 168^o. It is this lattice decrease that strongly indicates the β → γ phase transition should involve a temperature cooling process. It is also apparent that the slope of the lattice constant vs. θ_z is much smaller near the β state than that at γ state, suggesting that the stability for the γ state is higher than that for the β state.

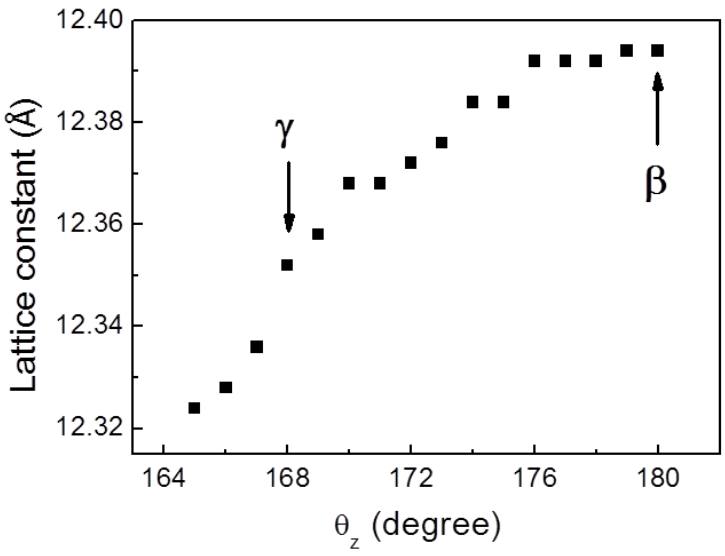

Fig. 2.4: Optimum lattice constant is displayed from the β to γ state.

To further understand the phase transition pathways, the functional variations of the minimum total energy for the α, β and γ states as a function of lattice constant are displayed in Fig. 2.5 a). These variations are considered as the α-, β-, and γ-branch for our description purpose. The energy separations of $E_\alpha - E_\beta$ and $E_\beta - E_\gamma$ are also shown in Fig. 2.5 b) as the

black and red curves, respectively. These branches can be best fitted as quadratic variation around the equilibrium position in the range of our interest: $E_\eta = A_\eta (x - x_\eta)^2 + B_\eta$, where $\eta = \alpha$, β or γ. As shown in Fig. 2.5 b), the energy separations are linear with lattice constant. This implies that the quadratic coefficients containing bulk moduli are the same for the α, β, and γ states. With the assumption that the Cs offset for the γ state does not change with temperature and remains unchanged at the optimum Cs offset, the normal phase transition pathway can now be explained in view of Fig. 2.5 a). When a CSI sample is at a high temperature associated with a large lattice constant, the transition from the α branch at point A to the β branch at point B could occur since the energy of the α state is higher than that of the β state, as indicated in Fig. 2.5 a). This suggests that α state is not stable even when the system maintains at the high temperature. The β state is a stable state at point B on the β-branch because the energy is lower than the γ state. As the sample temperature decreases, the β state energy decreases. After passing through the transition point C, the β state is being transferred to a γ state on the γ-branch. Finally, the γ state is established at point D and is stable as temperature further decreases.

For the reverse transition process, starting from the energy minimum of the γ state at point D, a stable β structure can be obtained following the direction of D to C, and subsequently from C to B by elevating the crystal temperature as shown in Fig. 2.5 b). The energy difference of $E_\alpha - E_\beta$ is positively dependent on temperature and always greater than zero at high temperature. This indicates that the transition from the $\beta \rightarrow \alpha$ phase with increasing temperature will not occur. Therefore, the phase transition from the $\alpha \rightarrow \beta$ state is not reversible and the α state is not a stable state since it can be deformed to the β state with no energy barrier. This seems to be inconsistent with the experiment observation[13] of the

XRD pattern from the α structure at 446 ^{o}K. However, the experimental α state was obtained from a yellow CSI sample. It might be possible that a dynamic equilibrium condition could be reached between the yellow CSI and the black α structure while the XRD data were taken.

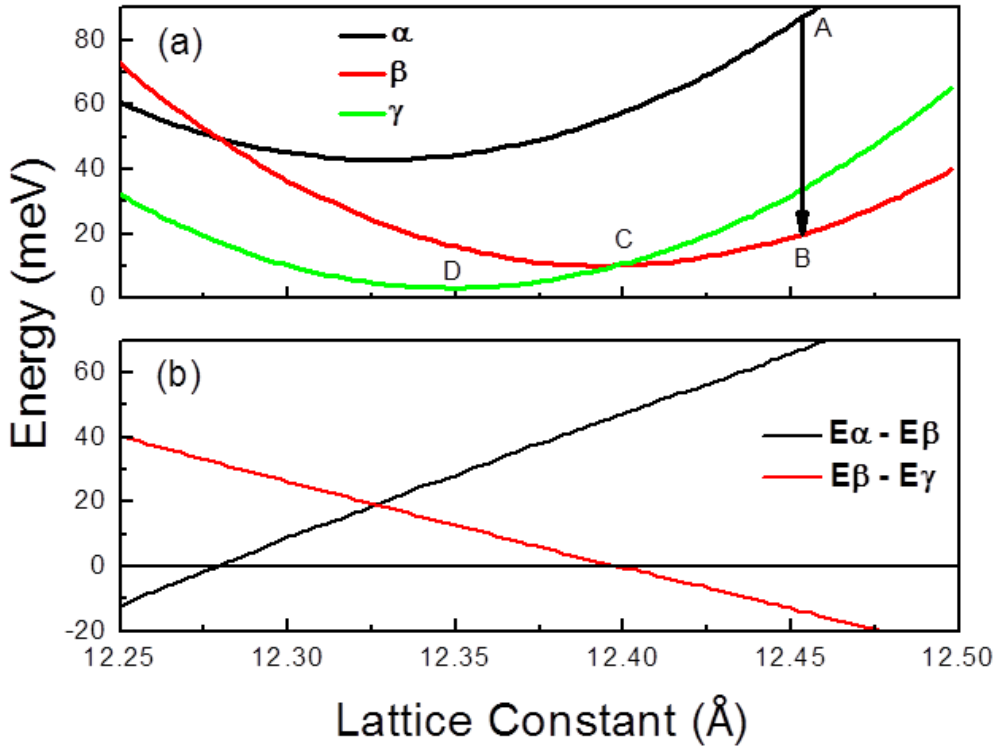

Fig. 2.5: a) The total energies for α (black), β (red), and γ (blue) state are plotted as a function of lattice constant. **b)** The energy differences of $E_\alpha - E_\beta$ and $E_\beta - E_\gamma$ are shown at various lattice constants. Phase transitions are expected to occur when the energy difference between two states are zero.

2.6 The role of Cs atoms

In the analysis of lattice constant effect in the last section, we have assumed the Cs atoms to be at the optimum position for each state at various temperatures. The role of Cs atom is to provide additional electronic charges to balance the charge distribution in the crystal. Each Cs is surrounded by eight nearest SnI_6 octahedra, and vice versa. The equilibrium positions for

the Cs atoms are determined by the position and tilting of SnI_6 octahedra for a given set of the bond angles. Therefore, the Cs offset is not a direct indicator of temperature and should have an independent effect on the total energy analysis. This independence between the effect of Cs offset and lattice constant on the total energy per unit cell is supported by the calculation of the γ state energy as shown in Fig. 2.6. At different lattice constant, the shape of the energy variation as a function of Cs offset is the same. Meanwhile, the extracted optimum Cs offset position is the same for different lattice constants. Reversely, the optimum lattice constant is the same for different Cs offsets. The non-entangled parameters of the Cs position offset and lattice constant also justifies our calculation method introduced earlier. It should be mentioned that the calculation that leads to the results in Fig. 2.6 is simplified by assuming a fixed ratio between CsX and CsY, and thus we can use only CsX to represent the Cs offsets.

The Cs offset from the original coordinates (0, 0, 0.25) in the pathway from the β → γ state is displayed in Fig. 2.7 for $\theta_{xy} = 163^o$. When the value of θ_{xy} is kept constant, the absolute values of CsX and CsY increase almost linearly as θ_z decreases from 180^o. The effect of changing θ_{xy} is similar while θ_z is kept constant. The further away from the cubic structure, the larger the Cs position offset should be. It should be emphasize that the calculated optimum Cs offset is zero when $\theta_z=180^o$, which is consistent with the symmetry requirements for the α and β states.

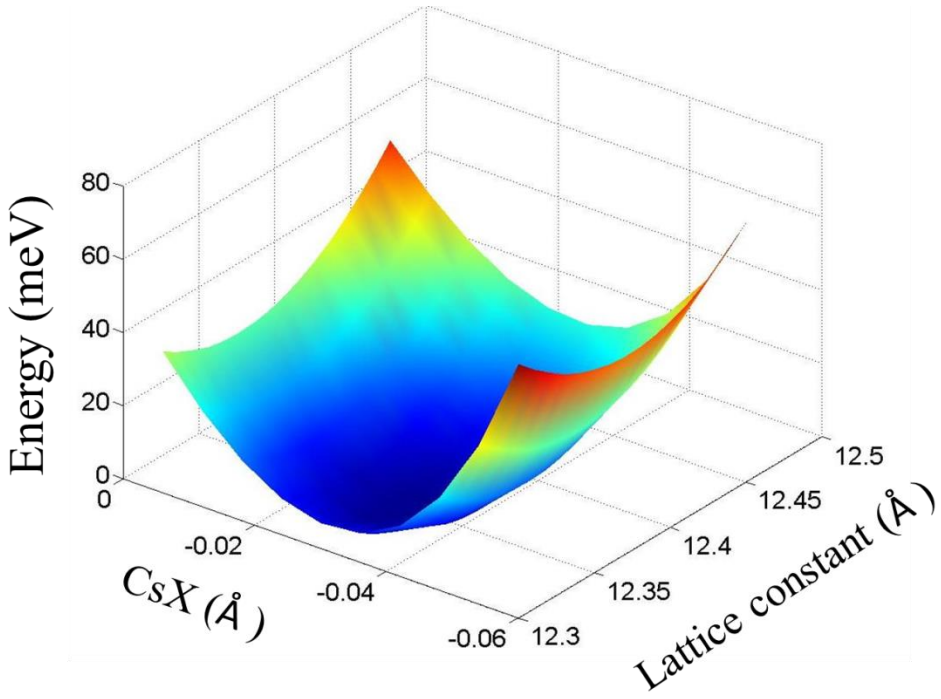

Fig. 2.6: The unit cell energy of γ state is plotted at various Cs offset and lattice constant.

Although the deviations of Cs coordinates are relatively small, they are crucial in the total energy calculation. This is demonstrated by the total energy as a function of θ_{xy} and θ_z as plotted in Fig. 2.8 at zero temperature without Cs offsets. It shows that the β state is the global minimum energy state. The γ state (163^o, 168^o) is now about 60 meV higher than the β state (163^o, 180^o). Therefore, without the Cs atom movement, the phase transition from the β → γ structure is not allowed. Meanwhile, the energy of each state in the pathway from the α → β state with $\theta_z = 180^o$ is lower than that of all other states with $\theta_z \neq 180^o$. This energy difference provides the energy barrier along the α → β pathway preventing the crystal from deforming to the other states with $\theta_z \neq 180^o$. It is also the reason why the α state will not be transferred to the γ state directly without going through the β state.

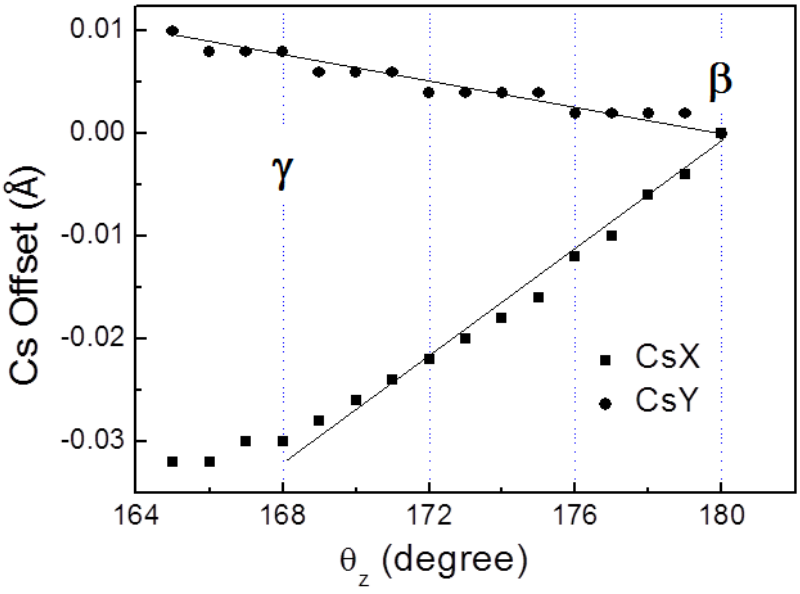

Fig. 2.7: Optimum values of CsX and CsY from the β to γ state are plotted as a function of θ_z.

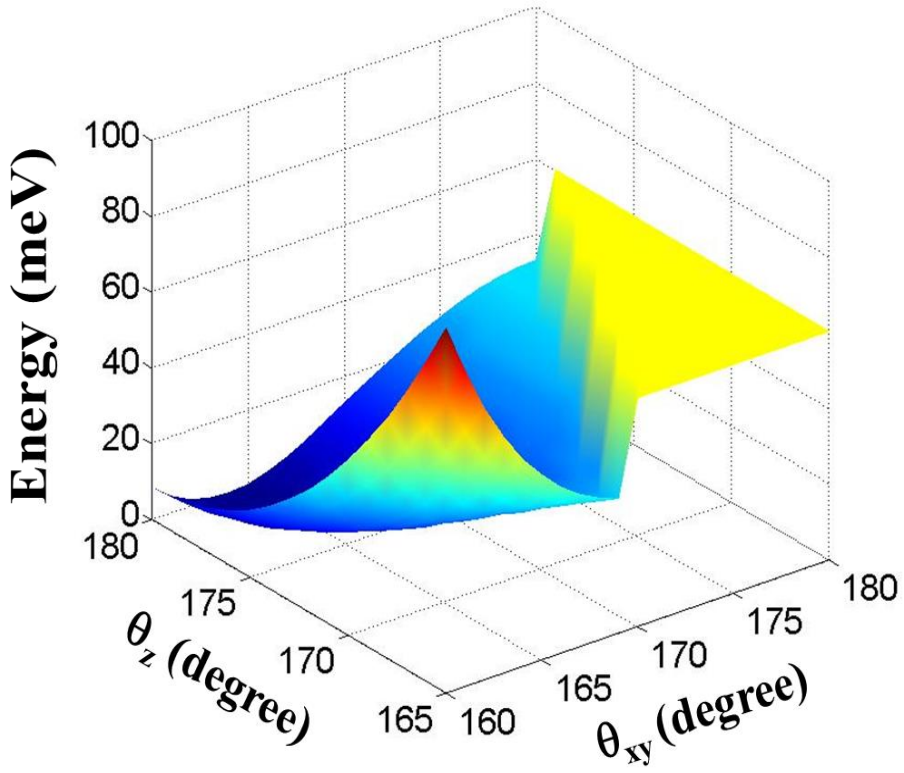

Fig. 2.8: The minimum total energy per unit cell is plotted as functions of θ_z and θ_{xy} at zero temperature without the Cs-offset optimization.

2.7 Summary

In conclusion, the phase transition processes of the black CSI are modeled using two bond angles of Sn-I-Sn in the vertical and horizontal directions to represent a set of the intermediate states. The detailed structure parameters for the γ phase at zero temperature are obtained by first principles calculations and discussed with the available experimental data. The underlying physics is revealed through exploring how the lattice constant and Cs position offset affect the energy minimization of unit cells in a given set of transition states. By analyzing the effect of lattice expansion, it is concluded that the transitional process between the β and γ state is reversible by changing the crystal temperature. The α state is not stable as it can be deformed to the β state without any energy barriers. The Cs position offsets are determined by the bond angle set at a given temperature. They are crucial in forming the γ state. It is also noted that the role of Cs offsets prevents the direct phase transition from the α → γ state.

Chapter 3: Electronic band structure characteristics of $CsSnI_3$

In the last chapter, we have determined the detailed atomic structure information through the first-principles calculations. Based on this structure information, we can obtain the electronic band structure and density of states using the same calculation software. The calculation method is the same as described in Chapter 2.

The band diagram of γ structure CSI and the density of states (DOS) are shown as in Fig.3.1 and Fig.3.2, respectively. The detailed structure input into the calculation program is determined through the total energy calculation described in Chapter 2. The theoretical calculated band-gap value is known to be undervalued. Therefore, we have used the experimental measured value of 1.3 eV at 300 K to proportionally adjust the calculated band diagram to match the experimental value of band gap. This band diagram further confirms that CSI is a direct band gap material. There are several interesting features: 1) the effective mass of electron and hole could be then estimated by a quadratic fitting of the lowest conduction band (CB1) and highest valence band (VB1), to be $0.734m_0$ and $0.151\ m_0$ respectively. The effective mass of electron is much larger than that of the hole; 2) It is also noticeable that there is another conduction band (CB2) closely adjacent to CB1 with separation about 60 meV. They are parallel to each other in momentum space from Γ to S point. From the DOS graph, the electronic states of the CB1 is the p-orbital of the central tin atom of the SnI_6 octahedron; while the p- and s-orbital of the 6 outer iodine atoms of the octahedron equally contribute to the CB2 states. The electronic states of VB1 originate mainly from the p-orbital of iodine atoms.

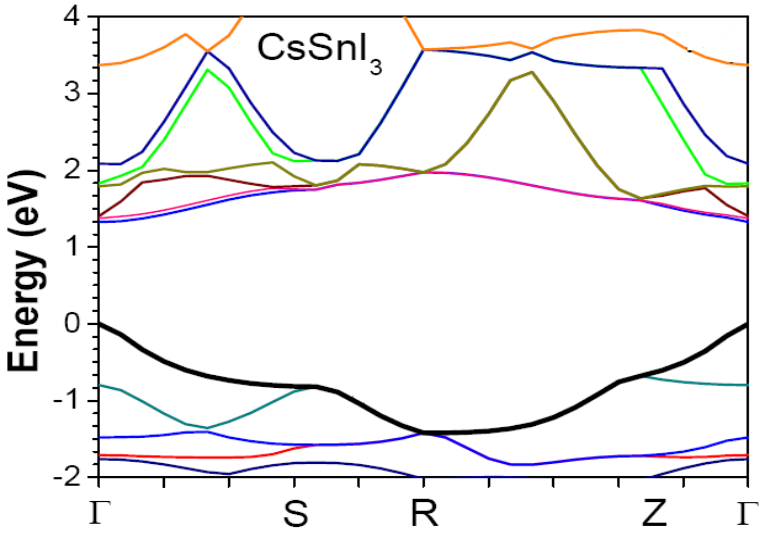

Fig. 3.1: Calculated electronic band diagram of γ structure CSI. The theoretically calculated band-gap value from the first principle is known to be underestimated; the experimentally measured band-gap value of 1.3 eV at 300 K is used to scale up band diagram.

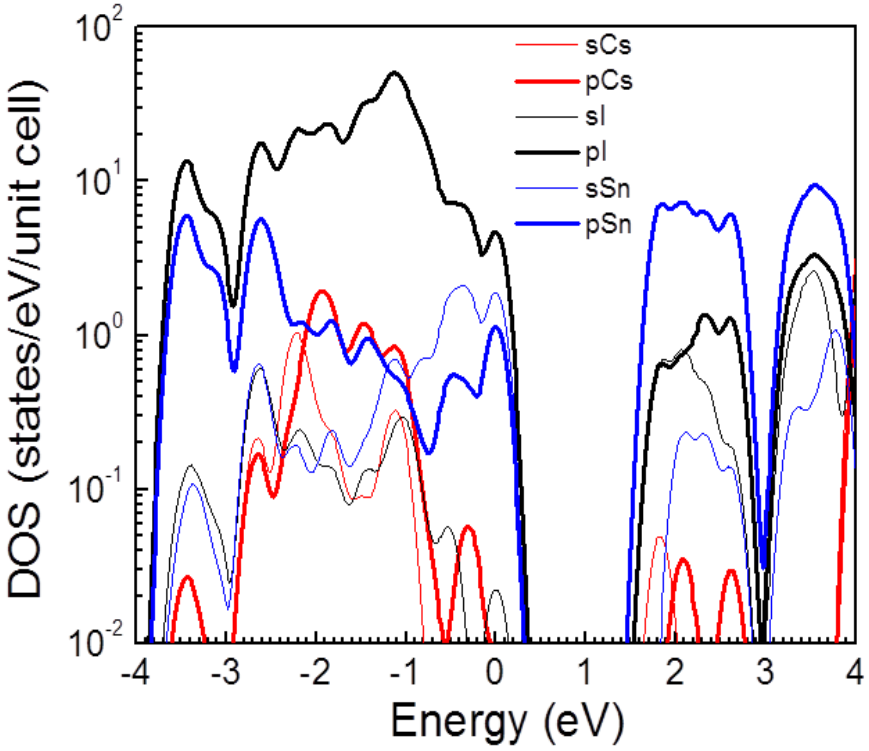

Fig. 3.2: Orbital-resolved density of states (DOS) is displayed. A broadening factor of 0.1 eV was used.

This unique band diagram is naturally determined by the atomic structure of CSI (refer to black γ structure CSI unless otherwise stated). And several interesting properties of CSI can

be interpreted by the band structure. In the next chapter, we will discuss how the relative larger electron effective mass (than hole) could result in abnormal temperature dependence of the band gap. The separation of the two parallel conduction bands is about 60 meV, which is close to the energy of two LO phonons (LO phonon energy determined to be 32 meV by Raman spectrum in chapter 5). This unique parallel band structure is very favorable of exciton-2 LO phonon interaction process. We can expect to see the two LO phonon features in optical spectrums, as would be demonstrated in Chapter 5 for Raman spectrum and Chapter 6 for PLE spectrum.

Chapter 4: Abnormal Temperature Dependence of the Band Gap of $CsSnI_3$

4.1 Background of band gap problem and introduction of our treatment

One of the interesting properties of $CsSnI_3$ is the strong and linear increase of the band (or energy) gap (E_g) with increasing temperature, which is opposite to what have been observed for most of common semiconductors. The electronic band gap is an important fundamental parameter of a semiconductor in terms of its electric and optical properties. The first experimental work on E_g dated back to the dawn of the semiconductor era. The successes of semiconductor based transistors, lasers, light-emitting diodes, and recently solar cells, have stimulated extensive works on the band gap variation with temperature, E_g (T), both theoretically and experimentally over many decades. These studies have successfully explained the normal behavior of the temperature dependence of band gap: measured E_g (T) curves show a monotonic decrease with temperature non-linearly at low T and linearly at high T. However, there are some exceptions which exhibit anomalous temperature behaviors. An early example is PbTe [16]. A blue energy gap shift was reported for this material in the temperature range from 100 to 300 K. In addition, the measured band gaps of CuBr and CuCl increase monotonically from near zero to room temperature [17]. More recently, a similar anomalous behavior has been observed for PbS [18]. The reason for this anomalous band gap behavior is not quite clear yet and needs to be further investigated. Exploring new materials with an anomalous temperature dependence of band gap remains interesting and helpful for fully understanding this fundamental problem.

In this chapter, the measured band gap as a function of temperature in $CsSnI_3$ by PL method is studied. The band gap is determined through a PL line shape analysis. It shows a

linearly positive relationship with temperature from 20 to 300 K. We explain our experimental data from three aspects. We first revisit the theoretical background for the temperature dependence of a semiconductor band gap. We then study the direct contribution of electron-phonon (e-p) interaction, based on the electron and hole effective mass estimated from the band diagram. Finally, we determine the thermal contribution to the band gap variation for $CsSnI_3$ by means of the first-principles calculations of band gap.

4.2 Determine the band gap of CSI from PL spectrum

The PL system is used to measure the PL spectra of the vacuum-based CSI thin film at low temperature. A $CsSnI_3$ thin film sample (silicon substrate in this case) was mounted on the cupper finger of a closed-cycle optical cryostat, which is capable of having temperature variation from 9 to 350 K. Excitation wavelength was 500 nm with a pass band of 5 nm for steady state PL. Excitation power density was about 0.5 mW/cm^2. Spectra were corrected by using a standard light source purchased from Ocean Optics Inc.

Normalized PL spectra from 9 to 300 K are displayed in Fig.4.1. The full width at half maximum (FWHM) of each spectrum is shown in the inset of this Fig.ure. Two important features are readily identified: (1) PL peak shifts to shorter wavelength, and (2) PL spectrum broadens as the sample temperature increases from 9 to 300 K. We now turn to discuss how to deduce accurate band gaps from PL spectra at various sample temperatures. There are two contributions to the PL line width broadening. One is the temperature dependent asymmetric thermal broadening on the high energy tail of a spectrum arising from more energetic excitons. A constant two-dimensional density of states and a Boltzmann thermal distribution with an exciton temperature (T_x) are used for this part of line shape. The other one is due to the symmetric broadening resulting from both the inhomogeneous broadening because of the nature polycrystalline compound and the homogeneous broadening originated from e-p

interactions. Main reasons for inhomogeneous broadening may include composition fluctuations and granular boundaries. We assume this symmetric broadening to be a Gaussian with a variance of σ. Combining the above two contributions, a PL spectrum at a given sample temperature can be fitted by the following convolution expression:

$$PL(E) = G(E,\sigma) * \exp(-(E - E_g + E_{bx}) / (K_B T_x)). \quad (4.1)$$

All measured PL spectra from 9 to 300 K were fitted by Eq. 4.1. The calculated spectra are shown in Fig.4.1 (b). To demonstrate the quality of fitting, two measured PL spectra at 80 and 220 K (discrete symbols) are plotted in a log scale in the inset along with the calculated spectra (solid-line curves). The spectrum fit over three orders of magnitude is highly satisfied for all spectra except a small deviation at low energy side for a few spectra with temperature greater than 200 K. However, this deviation will not affect the accuracy of the band gap determination. The focus point in this chapter is the deduced band gap at different temperature, which is summarized in Fig. 4.2 as solid spheres. This plot presents a salient feature: the band gap follows a positive linear-dependence in the temperature range we studied although it tends to be flat at temperature below 20 K. This feature is referred as the anomalous behavior of band gap in literature [17-18], and the reason still needs to be further investigated. In this chapter, we will discuss this interesting behavior.

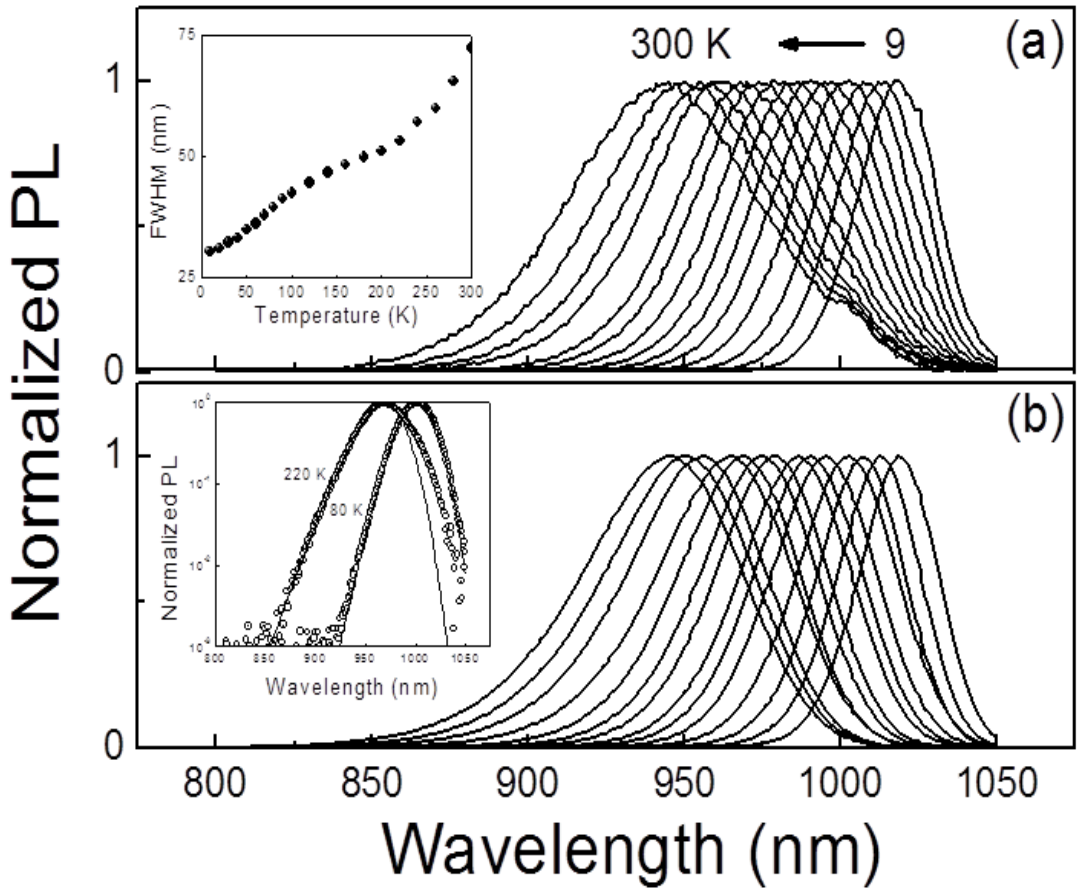

Fig. 4.1 (a) Normalized photoluminescence spectra measured at various temperatures from 9 to 300 K. The inset shows the temperature dependence of full width at half maximum (FWHM) of the PL spectra. (b) Calculated PL spectra using Eq. 4.1 which were matched to each measured PL spectrum to obtain band gap at different temperatures. The inset displays the two examples of spectrum fitting at 80 and 200 K. Discrete symbols represent the measured PL while solid curves are calculated PL spectra.

4.3 Theoretical Background of temperature dependence of band gap

The temperature dependence of band gap is generally described by the following expression under a quasi-harmonic approximation [19]:

$$\frac{\partial E_g}{\partial T} = \frac{\partial Eg}{\partial V} \cdot \frac{\partial V}{\partial T} + \sum_{j,\vec{q}} \left(\frac{\partial Eg}{\partial n_{j,\vec{q}}}\right)\left(n_{j,\vec{q}} + \frac{1}{2}\right), \tag{4.2}$$

where $n_{j,\vec{q}}$ is the number of phonons at j branch with wave vector $\vec{q}$, and it follows the Boltzmann distribution for bosons, $n_{j,q} = \frac{1}{\exp(\hbar\omega_{j,\vec{q}} / K_B T) - 1}$, where $\omega_{j,\vec{q}}$ is the angular frequency of the phonon mode. It is important to note that the summation in Eq. 4.2 is over all possible phonon modes in the entire Brillouin zone, i.e., q from 0 to q_{max}. The first part in Eq. 4.2 corresponds to the thermal expansion contribution, which arises from the anharmonicity of the inter-atomic potentials. The coefficient can be approximately considered to be temperature independent for a given semiconductor, and it can be either positive or negative. For instance, we have determined the sign of $\partial E_g / \partial V$ is positive for Si, while it is negative for GaAs. The origin of band gap in most semiconductors is the energy difference between bonding and anti-bonding of hybrid orbits. Thus, the value of $\partial E_g / \partial V$ depends on the specifics of the bonding parameters as well as the detailed orbits that form the band. In typical semiconductors, the thermal expansion contribution is considered to be a weak contribution to the temperature dependence of band gap. However, in $CsSnI_3$, it is shown that this contribution dominates over the contribution of direct e-p interaction.

The second part in Eq. 4.2 is the direct contribution of e-p interaction, which consists of Fan [20] and Debye-Waller [16, 21] terms. Fan term describes the virtual phonon emission and absorption processes as if e-p interaction is taken twice in 2nd-order perturbation theory. The Debye-Waller term represents the simultaneous interactions of an electron with two phonons in the branch j having the opposite wave vectors ($\vec{q}$ and -$\vec{q}$). This two-phonon interaction process is calculated using the 1st-order perturbation theory. Both processes are the 2nd-order approximation in the phonon amplitude, which will introduce an inverse dependence of atomic mass M and allows isotopic atom substitution studies. At relative high

temperature ($K_B T >> \hbar\omega_{j,\vec{q}}$), $n_{j,q} = \frac{1}{\exp(\hbar\omega_{j,\vec{q}} / K_B T) - 1} \sim \frac{K_B}{\hbar\omega_{j,\vec{q}}} T >> 1$ hence a linear temperature dependence of band gap is expected. At low temperature, however, the situation becomes more complicated. M. Cardona [22] investigated the Si band gap below 5 K and showed that the band gap followed the T^4 law. In principle, the coefficients $\frac{\partial Eg}{\partial n_{j,\vec{q}}}$ can be calculated with the full pseudo-potential description and phonon modes. In reality, however, it remains to be a challenging task to calculate the direct e-p contribution. As a result, many models have been developed to interpret experimental data, such as the Varshni empirical formula [23] $E_g(T) = E_g(0) - \alpha T^2/(T + \beta)$, where α and β are fitting parameters for a given semiconductor. Recently, the two-oscillator model [17, 18, 24, 25] has been developed. Using this model, the band gap variation with temperature can be expressed as

$$\Delta E_g(T) = -\frac{S_1}{\Omega_1 M_1}\left(\frac{1}{e^{\Omega_1/K_b T} - 1} + \frac{1}{2}\right) - \frac{S_2}{\Omega_2 M_2}\left(\frac{1}{e^{\Omega_2/K_b T} - 1} + \frac{1}{2}\right) \quad , \tag{4.3}$$

where Ω_i (i = 1, 2) is the phonon energy, M_i is the atomic mass, and S_i is the relative weight for oscillator 1 and 2, respectively. Instead of summing over all possible phonon modes in entire Brillouin zone, the two-oscillator model only considers two dominant phonon modes with two constant energy levels. By fitting experimental data, combined with isotropic atom replacement studies, one can get the information about the constants of S_1 and S_2, which reflects the contribution of direct e-p interaction. In the previous studies of the anomalous behavior of band gaps in CuCl and PbS system, the values of S_1 and S_2 were determined to have different sign, and the term with negative sign dominated, thus resulting in a positive temperature dependence of band gap. Although the two-oscillator model has been used to successfully explain the anomalous behavior of the band gap variation with temperature, it also provides a feasible case that the constants of S_1 and S_2 might have amplitude but opposite

sign. If this case holds true in some semiconductors, then the contribution of direct e-p interaction to the band gap change with temperature vanishes, leading to the dominant contribution by the thermal expansion as temperature increases. As examples, we describe in next section how it might be possible in case of $CsSnI_3$ that the Fan term may actually disappear after summing all the contributions in entire q wave vector space.

4.4 Analysis of the Electron-phonon Interaction effect on the band gap

The Fan term is given by:

$$\Delta E_g = -\sum_{\vec{q}} \frac{\left|\left\langle \vec{k} \mid H_{el-ph} \mid \vec{k}-\vec{q} \right\rangle\right|^2}{E(\vec{k}-\vec{q}) - E(k) + \hbar\omega_{\vec{q}}} - \sum_{\vec{q}} \frac{\left|\left\langle \vec{k} \mid H_{el-ph} \mid \vec{k}+\vec{q} \right\rangle\right|^2}{E(\vec{k}+\vec{q}) - E(\vec{k}) - \hbar\omega_{\vec{q}}} \quad . \tag{4.4}$$

The first and second terms correspond to the emission and absorption of phonon at wave vector q, respectively. We first examine acoustic phonons and limit our attention near the electronic band edge, $k \approx 0$, Eq. 4.4 becomes

$$\Delta E_g = -A\sum_{\vec{q}} \frac{4m^* |q|}{q^2 - Q^2} \cdot \frac{1}{e^{\hbar v_q / K_B T} - 1} \quad , \tag{4.5}$$

where A is a positive constant, m^* is the effective mass of carriers, and $Q = \left|\frac{2m^* v_q}{\hbar}\right|$ with $v_{\vec{q}}$ as the velocity of acoustic wave near the zone edge. If a condition so that $K_B T >> \hbar v_{\vec{q}}$,

$$\Delta E_g = -A\frac{K_B}{\hbar v_{\vec{q}}} \sum_{\vec{q}} \frac{4m^*}{q^2 - Q^2} T \quad . \tag{4.6}$$

From the above equation, the positive contribution of ΔE_g arises from all the phonon modes with $|q| < Q$, while its negative contribution comes from the phonon modes with $|q| > Q$. If Q is smaller than $|q|_{\max}$ by two or three orders of magnitude, most of phonon modes will satisfy

$|q| > Q$ and lead to a negative value of ΔE_g in Eq. 4.6. That is the case for most of tetrahedral semiconductors. For Si and GaAs, Q_e is about $10^7 \mathrm{m}^{-1}$, which is two orders of magnitude smaller than $|q|_{\max}$ ($5.6\times10^9 m^{-1}$). For $CsSnI_3$, $Q_e = 1.6\times10^8 m^{-1}$, $Q_h = 3.3\times10^7 m^{-1}$ are calculated using the electron effective mass of 0.734 m_0 and the hole effective mass of 0.151 m_0 near Γ point,[1] respectively. The value of effective mass is estimated by the calculation of band structure shown in the Chapter 3. The maximum phonon wave vector is estimated to be $3.9\times10^9 m^{-1}$ using the lattice constants obtained by experimental X-ray diffraction data[13] at room temperature. The large Q value due to the large electron effective mass in $CsSnI_3$ makes it possible that the value of ΔE_g in Eq. 4.6 becomes negligible.

For optical phonons, the situation is quite similar. For simplicity, we consider longitudinal optical (LO) phonon mode and assume very flat dispersion for LO phonons, then, the Eq. 4.4 becomes

$$\Delta E_g = -B\sum_{\vec{q}} \frac{m^* q^2}{q^4 - P^4} \frac{1}{e^{\Omega/kT} - 1}, \tag{4.7}$$

where $P = \frac{\sqrt{2m^*\Omega}}{\hbar}$. Use the same parameters as the case of acoustic phonons and the measured[15] LO phonon energy (Ω) of 32 meV. We obtained for electrons and holes, respectively, $P_e = 0.78\times10^9 m^{-1}$ and $P_h = 0.35\times10^9 m^{-1}$, which is comparable with $|q|_{\max}$. Similar to the acoustic phonon case, the value of ΔE_g in Eq. 4.7 may be also insignificant.

To fully determine the value of Fan term with the large Q (P) in $CsSnI_3$, we need to know all possible phonon modes, which is extremely difficult. However, if we only count for two major phonon modes, Eq. 4.5 and 4.7 will apparently lead to the two-oscillator model.

The sign of $\frac{1}{q^2 - Q^2}$ ($\frac{1}{q^4 - P^4}$ in case of LO phonon modes) determines the sign of S_1 and S_2 in Eq. 3.3. With the large $Q(P)$, it is possible that one mode satisfy $|q| < Q(P)$, while the other have $|q| > Q(P)$. In this case, S_1 and S_2 in Eq. 3.3 will have opposite sign. When S_1 and S_2 are very close in magnitude, the contribution of direct e-p interaction to $\Delta E_g(T)$ would vanish. We conjecture this is the case for $CsSnI_3$ and work out the thermal expansion contribution with the measured data.

4.5 Thermal Expansion Contribution to the band gap

We treat this problem by freezing the lattice (i.e., always at T = 0 K, neglecting the effect of phonon), and then calculate the band gap of $CsSnI_3$ as we rigidly reduce the lattice constant from to $a_0 - \Delta a$, where a_0 is the lattice constant at 300 K. We use a to represent three different lattice constants in an orthorhombic structure. Of course, the lattice can never be frozen in equilibrium even at 0 K because of none-zero ground state energy. However, it is possible to investigate solely the band gap change with increasing or decreasing volume. By assuming a linear relationship between lattice constant and temperature, the calculated band gap $E_g(\Delta a / a_0)$, can be used to fit the experimental data $E_g(T)$. From this fitting, the value of linear thermal expansion coefficient α_L can be obtained. In this approach, we use our assumption that the direct e-p interaction contribution is negligible and thermal expansion effect is dominant for the temperature behavior of the band gap in this material. The validation of this assumption will be checked by comparing the deduced value of linear thermal expansion coefficient with the experimentally measured one for $CsSnI_3$. However, the information of this coefficient of $CsSnI_3$ is not yet available. We will then compare the

reduced parameter with the coefficient of other perovskite materials with a similar crystal structure, to verify our assumption.

The solid line in Fig. 4.2 shows the calculated E_g vs. $\Delta a / a_0$ (top axis). The calculation of band gap is done using the same software with the same setup as described in Chapter 2. It can be seen that the band gap decreases linearly as lattice constant contracts from its room temperature values. It requires a linear lattice change of 0.42% from room temperature to 0 K to match the measured band gap variation with temperature. The top axis $\Delta a / a_0$ and bottom axis can be overlapped by assuming a constant linear thermal coefficient α_L with a value of $0.42/100/300 = 1.40 \times 10^{-5}\ K^{-1}$. Thus the solid line can be recognized as the calculated E_g vs. T due to thermal expansion or contraction. The calculated curve fits the experimental data very well except at low temperature less than 20 K. The reason is that we have assumed expansion coefficient to be constant, which may not be accurate at low temperature. If we adjust the expansion coefficient to be temperature dependent at low temperature, it is possible to obtain a better fit with the experimental data. However, since we are more interested in a large temperature range of great than 20 K, lack of this adjustment does not influence our conclusion.

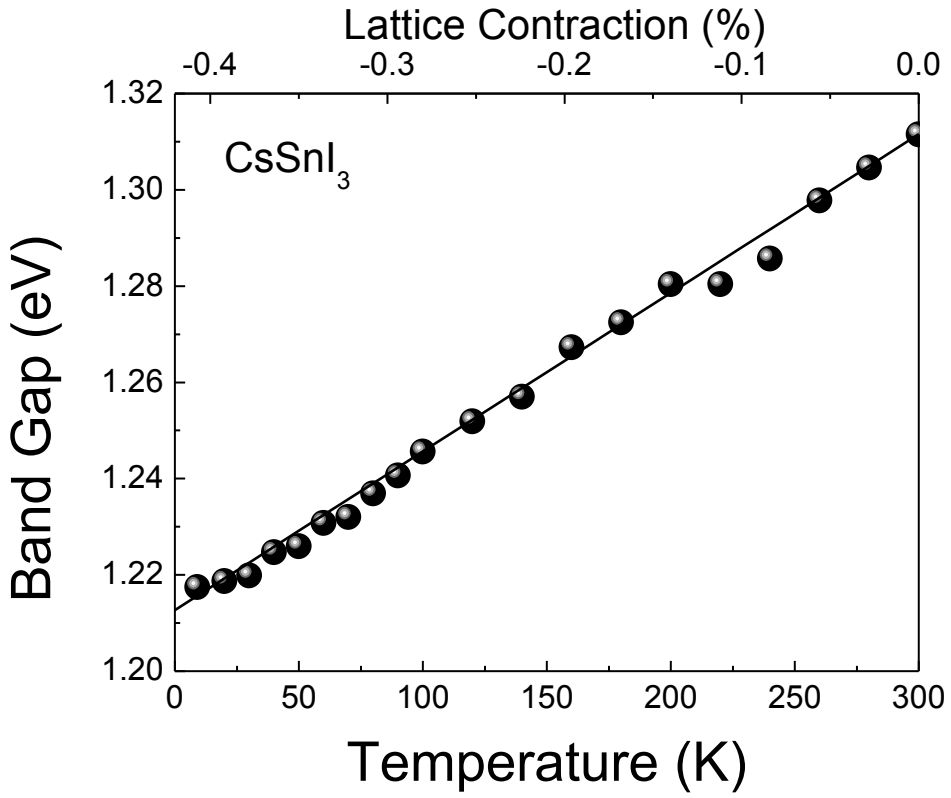

Fig. 4.2 Band gap of $CsSnI_3$ at various temperatures deduced from photoluminescence spectrum (solid spheres) and the band gap variation with lattice contraction obtained from first-principles calculations (solid line). The top axis is the relative lattice contraction, $\Delta a / a_0$, where a_0 is the lattice constant at room temperature.

As we mentioned, the validity of this matching relies on the justification of the deduced value of linear thermal coefficient α_L, which is usually measured by X-ray diffraction method. The value of α_L for several perovskites with orthorhombic structure such as $SrZrO_3$ [26],$ScAlO_3$ [27], and $MgSiO_3$ [28] have been experimentally measured to be 1.08×10^{-5} K^{-1}, 0.90×10^{-5} K^{-1},and 1.57×10^{-5} K^{-1}, respectively. The value of α_L can be also obtained theoretically using various models such as molecular dynamics, lattice dynamics, and Debye model [29]. For example, the value for $MgSiO_3$ has been calculated [30] to be 2.09×10^{-5} K^{-1}. Our deduced value of α_L for $CsSnI_3$ is 1.40×10^{-5} K^{-1}, which is very reasonable comparing with the measured or calculated α_L values for other perovskites materials available in

literature. Therefore, our assumption is justified that the contribution of direct e-p interaction is negligible and the variation of E_g (T) is dominated by the thermal expansion contribution.

4.6 Summary

In this chapter, we have determined the band gap of CSI as function of temperature from 9 to 300 K by photoluminescence method. The band gap variation with temperature shows uncommon positive linear temperature dependence. It is conjectured that the contribution of direct electron-phonon interaction to the band gap change is negligible likely due to the unusual large electron effective mass. We justified this conjecture by the first-principles calculations of band gap with various lattice constants, which changes linearly with temperature. By matching the experimentally measured band gap variation with temperature to the calculated, we deduced a linear thermal expansion coefficient of 1.40 x 10^{-5} K^{-1} for $CsSnI_3$, which is consistent with several other materials having a same crystal structure as $CsSnI_3$.

Chapter 5: Triply resonant Raman scattering: manifestation of two LO phonon process in $CsSnI_3$

5.1 Resonant Raman scattering background

Resonant Raman spectroscopy is a powerful tool to obtain useful information about the vibronic properties of a condensed matter. In the normal Raman process, the incoming photon is scattered by the vibration and lose the energy to one or more LO phonons. The intermediate states are all virtual for normal Raman process. Raman scattering efficiency is enhanced when the incoming or outgoing photon energy approaches to the combined high density of electronic states in a semiconductor. There were many experimental studies [31-33] using the single resonant Raman process to characterize electron-phonon coupling. The double resonant Raman scattering was reported in graphite [34] when both incoming and outgoing photons met with real electronic states. Such a double resonant Raman process was also investigated in carbon nanotubes [35]. Triply enhanced resonant Raman scattering process was not as often reported as the single and double resonant Raman process. Alexandrou *et al* [36] studied the triply enhanced Raman process in GaAs/AlAs superlattices when the energy difference between the heavy- and light-hole bands was tuned to be equal to the energy of two LO phonons by spatial confinement. In their study, all the intermediate states of the SORS were real. Hence, the Raman scattering efficiency was greatly enhanced. A similar work carried out by Schneider *et al.* [37] also revealed the nature of triply enhanced resonant SORS. In their work, the electronic states under electric field, known as Wannier-Stark ladders, were separated by the energy of two LO phonons.

In chapter 3, we have presented the first-principles study of $CsSnI_3$ including its band structure calculation. One of fine features we have identified for CSI is that it has two

adjacent parallel conduction bands separated by ~ 60 meV. The origin of electronic states for the lowest conduction band is mainly from the p-orbitals of the inner tin atom of octahedron while the s- and p-orbitals of six outer iodine atoms of octahedron are the main sources of electronic states for the next conduction band. If the LO phonon energy in this material is about the half of the parallel band separation, we should be able to see the second order Raman scatter (SORS) which emits two LO phonons, to be resonantly enhanced by this unique two-parallel-conduction band structure.

In this chapter, the observation of the first order and triple-resonance enhanced SORS processes by LO phonons in $CsSnI_3$ is studied. We verify our experimental observations with a theoretical calculation of the SORS spectrum using the band structure property of $CsSnI_3$. And finally an effective phonon dispersion curve for LO phonons by fitting the calculated SORS spectrum with the measured one is obtained.

5.2 Experiment of Raman Spectrum

We use the CSI thin film with CsI/SnI_2 synthesized by vacuum evaporation method for the Raman measurement. The schematic diagram of Raman measurement setup is shown as in Fig. 5.1 The system is similar to the PL measurement system, however, the requirement for the detection monochromator (the grating in Fig. 5.1) is very stringent because we are collecting extremely weak signal very close (a few nm away) to the strong laser excitation wavelength. The Raman measurements of our samples were performed using a Horiba J-Y Spectrometer equipped with an 1800 grooves/mm grating in case of the Ar^+ ion laser excitation at 514.5 nm, and with a 600 grooves/mm grating for the HeNe laser excitation at 632.8 nm. The measurements were performed at room temperature using a backscattering geometry (180^0) under an Olympus BX40 microscope with an objective.

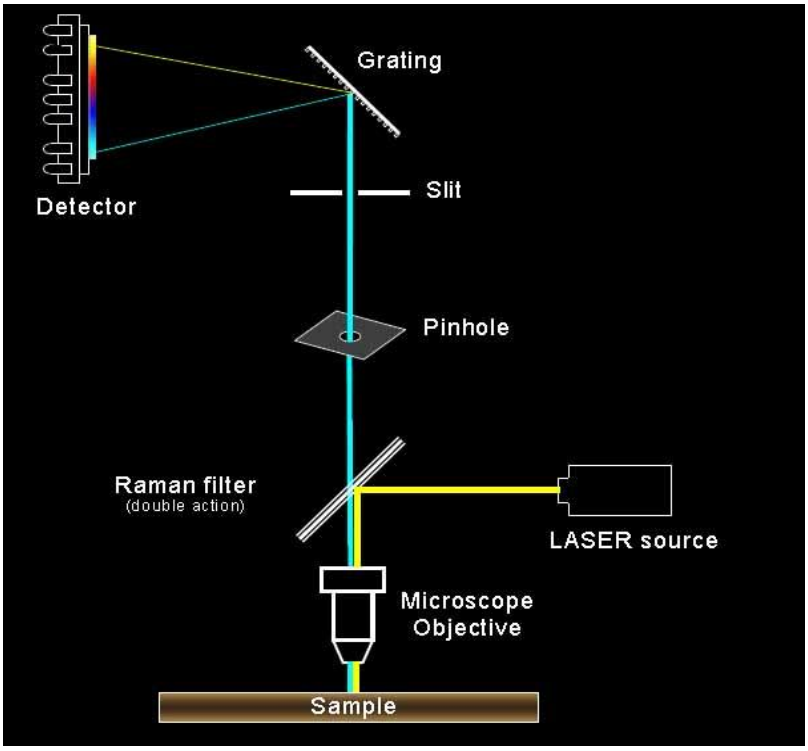

Fig. 5.1: Schematic diagram of the Raman measurement system

5.3 Identify the peaks for the Raman Spectra

The experimentally measured Raman spectrum of the CsSnI3 thin-film on ceramic substrate using the Ar+ laser at room temperature is displayed in Fig. 5.2 (a) as the solid curve. The calculated Raman spectra are also shown using the two different phonon dispersions; they will be discussed later. The measured spectrum shows two peaks with a few features: 1) the scattering intensity of the second peak at 58.5 meV is larger than that of the first peak at 32.0 meV; 2) there are no additional Raman peaks beyond the second one; 3) the Raman shift of the second peak is 5.5 meV less than the double (64 meV) of the Raman shift of the first peak; and 4) the shape of the second peak is asymmetric and much broader than that of the first peak. Since the first peak has a narrow full width of 1.5 meV at half maximum, the LO phonon modes near the center of the Brillouin zone should be responsible in the first order Raman scattering process due to the momentum conservation rule. Hence,

the LO phonon energy near Γ point is determined to be 32 meV. This assignment is further reinforced by the verification of the second peak as the SORS by two LO phonons involving a theoretical calculation to be discussed.

To experimentally verify that both first and second peak are associated with Raman process and originated from the CsSnI3 thin-film, another experiment was performed on the CsSnI3 thin-film deposited on glass substrate using the HeNe laser line at 632.8 nm. The measured Raman spectrum is displayed in Fig. 5.2 (b). It possesses all the features of the spectrum taken by the Ar+ laser line as shown in Fig. 5.2 (a). This experiment concludes that the two measured Raman peaks are from the CsSnI3 thin-film. It should be noted that the relative ratio for the first peak to second peak is different for the two spectra in Fig. 5.2. However, this difference will not affect our discussion.

If we followed the same theoretical treatment [38, 39] as the normal Raman scattering to determine the electron-phonon coupling strength using the intensity ratio of the second- over first-order Raman scattering, we would get an extraordinary large electron-phonon coupling constant, and would be different for the $CsSnI_3$ thin-films on different substrate. If that were the case, we would observe subsequent multiple phonon peaks after the second one. The absence of subsequent Raman peaks after the second one as shown in Fig. 5.2 discourages the normal explanation of extraordinary electron-phonon interaction strength in this material. The strong intensity of the second Raman peak has to be relevant with a resonant enhancement. This scenario is also consistent with the calculated energy separation between the two conduction bands which is close to the energy of two LO phonons. Therefore, the attribution of triply resonant SORS to the second Raman peak is considered as a reasonable explanation. We further verify this assignment by theoretically calculating the SORS spectrum and by comparing it with the measured one.

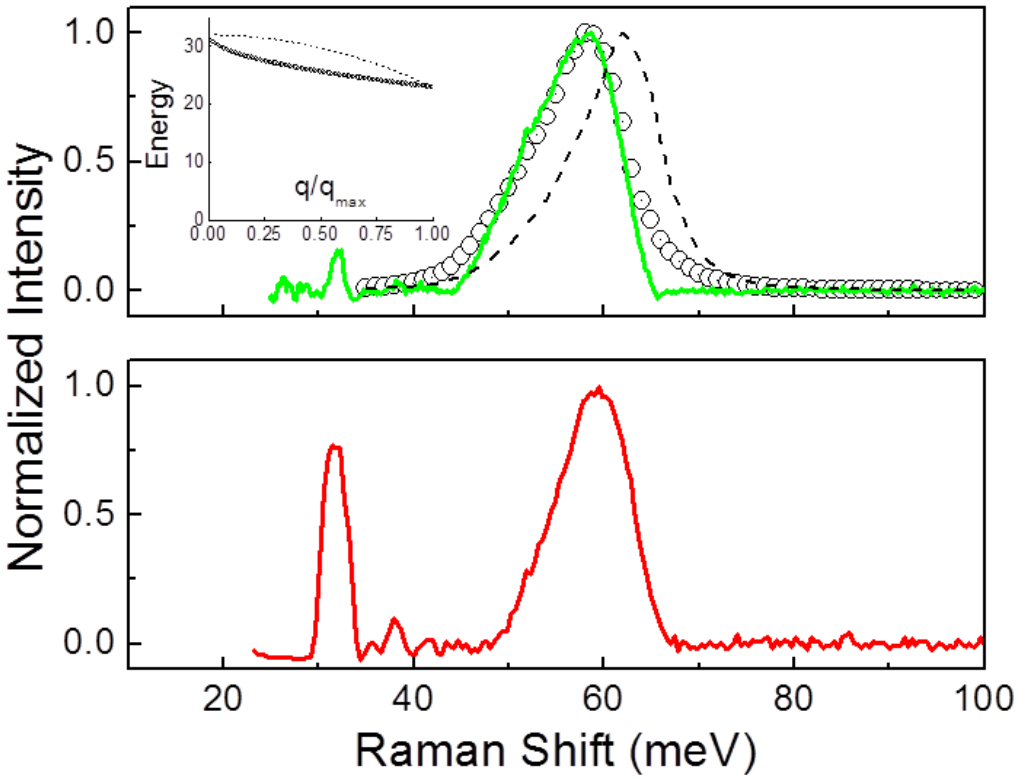

Fig. 5.2: Measured Raman scattering intensity as a function of Stokes energy shift, (a) solid curve spectrum taken from $CsSnI_3$ thin-film on ceramic substrate with Ar^+ laser at 514.5 nm, and (b) taken from $CsSnI_3$ thin-film on glass substrate with HeNe laser at 632.8 nm. The first peak located at 32 meV is due to the first order LO phonon scattering. The subsequent broad and asymmetric peak is from the triply enhanced second order Raman scatting. The curve with discrete symbols and the dashed curve are the calculated SORS spectra using the two different LO phonon dispersion curves shown in the inset of (a) as described in the text.

5.4 Possible triply Raman scattering process based on band structure

We need the information of band structure as presented in the Fig. 3.1 to analysis the scattering of the incoming photon. The calculated two low conduction bands and two top valence bands from Γ to S point are shown in Fig. 5.3. The curvature of the lowest conduction band (CB1) is smaller than the top valence band, which implies a relatively larger effective mass of electrons than that of holes. The uniqueness in this band diagram is the existence of another conduction band (CB2), which is closely adjacent and parallel to CB1 in the momentum space. The separation between CB1 and CB2 is 58 meV. Possible Raman processes leading to the resonance behavior of SORS are illustrated in the Fig.5.3. For

example, an electron is excited from the top valence band to the point C2 in CB2 by an incoming photon; a pair of phonons with wave vectors ± q is created by scattering the electron to the point C1 in CB1 through a real intermediate electronic state in CB1 at the point A. This process can be also accomplished by a different intermediate state at the point B. It is worthy to note that the HeNe laser has an access of the top valence band only while the Ar^+ laser line can access the two valence bands as schematically shown in Fig. 5.3. This difference in the initial joint density of electronic states might be a reason why the peak ratio in Fig. 5.2 (a) is different from that in Fig. 5.2 (b).

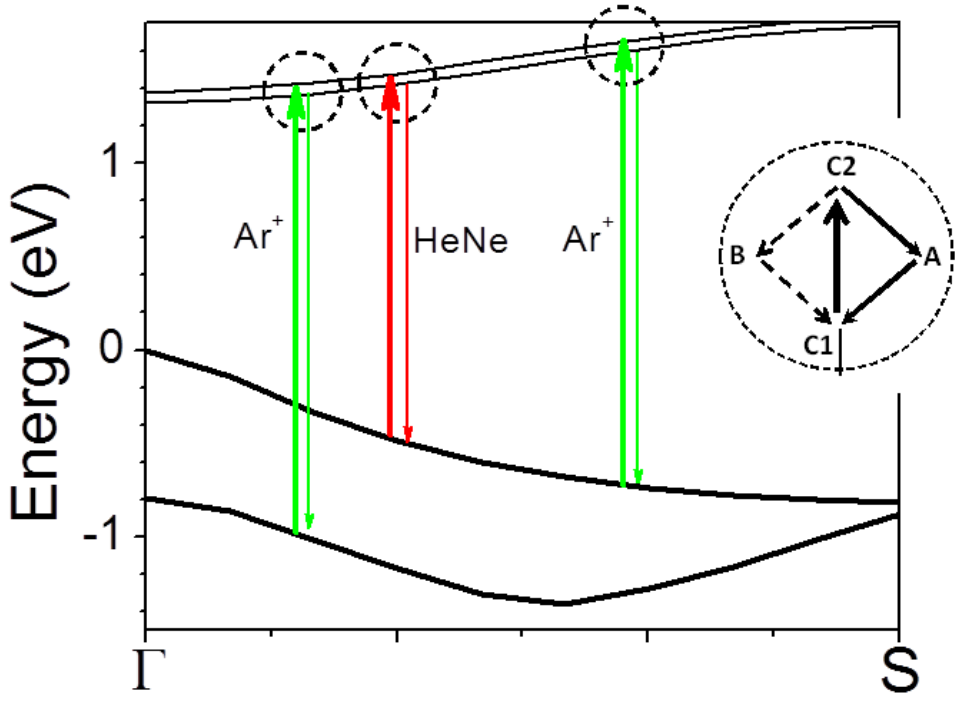

Fig. 5.3 Two top valence bands and two bottom conduction bands are shown from Γ to S point in wave vector space for $CsSnI_3$. Triply resonant Raman scattering processes are illustrated involving the electronic states in these four bands.

5.5 Theoretical validation of our assumption of triply resonant Raman process

Based on the strong polar nature of other perovskite materials [40, 41] with similar crystal structure as that of $CsSnI_3$, it is reasonable to assume that the dominant electron-phonon coupling possesses the usual form of Frohlich interaction. Hence, the main contribution of the second Raman peak is from the simultaneously scattering of two LO phonons with opposite wave-vector directions as illustrated in Fig. 5.3. The theoretical spectrum of SORS is given in the following equation based the usual understanding of electron-photon and electron-phonon interactions [42]:

$$I(\omega) \sim \sum_{\vec{q},\vec{k}} \sum_{l,m,n} \left| \frac{\left\langle f, V_{\vec{k}} \left| H_{e-R} \right| n, C_{\vec{k}} \right\rangle \left\langle n, C_{\vec{k}} \left| H_{el-ph} \right| m, C_{\vec{k}-\vec{q}} \right\rangle \left\langle m, C_{\vec{k}-\vec{q}} \left| H_{el-ph} \right| l, C_{\vec{k}} \right\rangle \left\langle l, C_{\vec{k}} \left| H_{e-R} \right| i, V_{\vec{k}} \right\rangle}{(E_f - E_n + \Omega_I - \omega + i\Gamma)(E_m - E_l + \hbar\omega_{LO}(q) + i\Gamma)(E_l - E_i - \Omega_I + i\Gamma)} \right|^2 \times \frac{\eta}{[\omega - 2\hbar\omega_{LO}(q)]^2 + 4\eta^2}. \quad (5.1)$$

In the Eq. 5.1, ω is the Raman energy shift, the indexes of *i, l, m, n,* and *f* represent possible real electronic bands associated a particular SORS process, and Ω_I is the excitation photon energy. The electron-radiation and electron-phonon interaction Hamiltonians are expressed as H_{e-R} and H_{el-ph}, respectively. The symbols of $C_{\vec{k}}$ and $V_{\vec{k}}$ represent the electronic states with wave vector *k* in conduction and valence band, respectively. It should be mentioned here that there are two broadening parameters in Eq. 5.1, Γ and η. The value of Γ is related to the dephasing time of electronic state involved in SORS processes. The value of η in the Lorentzian function is inversely proportional to the phonon dephasing time. The excitonic effect as explored by many researchers such as Garcia-Cristabal *et al* [43] were not considered in this calculation because the electronic states involved in Raman processes are far away from the band edge. There are two tasks for the theoretical calculation of SORS

spectrum: 1) to adequately predict the peak position (58 meV) of SORS by LO phonon scatterings with the LO phonon energy of 32 meV, and 2) to produce a broad and asymmetric line shape. For simplicity, only one of the processes depicted in Fig. 5.3 is considered which consists of one inter-band and one intra-band transition due to the electron-phonon interaction. The electron-phonon interaction Hamiltonian is known [44] to have the q^{-1} dependence and q-independence for inter- and intra-band transitions, respectively.

To numerically calculate the SORS spectrum, a LO-phonon dispersion relationship has to be specified, and the values of Γ and η have to be given and justified. Different types of LO phonon dispersion relationships were considered. Two of them are given here: (Dispersion #1) $\hbar\omega_{LO}(y) = 0.032 - 0.009*y^2$, and (Dispersion #2) $\hbar\omega_{LO}(y) = 0.032 - 0.009*\sqrt{y}$ in unit of eV, where $y = q/q_{max}$. The value of 32 meV is used as the LO phonon energy at Γ point (y = 0). These two dispersion relationships are displayed in the inset of Fig. 5.2 (a). The calculated SORS spectra are also shown in Fig. 5.2 (a) as discrete symbols using the dispersion #2 and as the dashed curve using the dispersion #1, respectively. Both dispersion #1 and #2 generates a broad and asymmetric SORS spectrum because a relatively wide range of phonon *q*-vector is allowed to participate in the SORS process. However, only the spectrum calculated using the dispersion #2 matches the experimentally measured peak position at 58.5 meV. It should be pointed out that the actually LO phonon dispersion should be measured by other experimental methods such as the method of inelastic neutron scattering [45]. The dispersion #2 should be considered as an *effective* LO dispersion since we have only considered one of many possible SORS processes for which their relative contributions to experimentally measured spectrum are not easy to be determined. In our calculation, the value of η = 1.5 meV was used since it matches with the measured full width at half maximum for the first order Raman peak. Various values of Γ were examined and 5

meV was found to fit the experimental data well, which indicates the fast electron scattering time of 0.8 ps out of initial electronic states. This scattering time is consistent with the fast electron thermalization process in other semiconductors such as GaAs [46]. It should be pointed here that the values of η and Γ were determined by fitting experimentally measured spectra. These values should reflect the contributions of homogeneous and inhomogeneous broadenings.

It is difficult to estimate exactly how much Raman scattering efficiency is enhanced due to the triple resonance since the exact material parameters for $CsSnI_3$ are needed for this to be computed. We instead calculated the SORS efficiency as a function of the energy separation between the two parallel conduction bands as displayed in Fig. 5.4 (a). It shows that the SORS efficiency is maximized when the energy separation is near the energy of 2 LO phonons. In order to gain the insight as which fraction of phonons in momentum space are particularly important for the SORS process, we also calculated the SORS intensity as a function of the normalized phonon wave vector. The result is displayed in Fig. 5.4 (b). It is sharply peaked when $q/q_{max} = 0.04$ with an asymmetric distribution extending to large wave vector values. This behavior explains why the measured SORS peak has broad and asymmetric line shape.

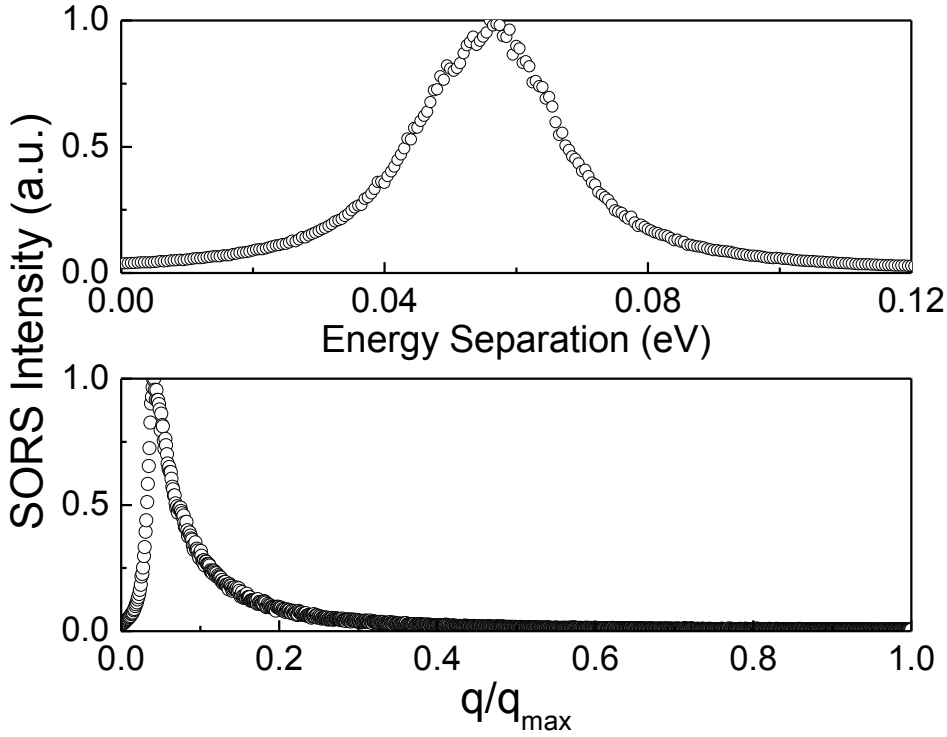

Fig. 5.4: Calculated SORS intensity as a function of the energy separation between two parallel conduction bands (a) and as a function the normalized magnitude of LO phonon wave vector (b).

5.6 Summary

In summary, the Raman scattering data of CSI are presented. The LO phonon energy is 32 meV, determined by the first order Raman peak position. As predicted by the unique band structure, it shows enormously enhanced intensity of the second-order Raman scattering. Such an enhancement is attributed to the triply resonant Raman scattering process by LO phonons, which is realized naturally through the unique two parallel conduction bands with a separation close to the energy of two LO phonons in this semiconductor compound. The observation of the larger SORS further validates the calculated band structure as presented in Chapter 3.

The strong two-LO phonon process predicted by the band structure has been demonstrated in the Raman scattering process. It encourages us to explore the two-LO

phonon process in the emission or absorption spectrum. However, the LO features is not observable in PL spectrum even at low temperature as shown in Fig. 4.1, due to the large inhomogeneous broadening introduced by the polycrystalline nature of the sample. The absorption spectrum of CSI at room temperature does not exhibit any LO phonon feature, and we do not have the equipment to measure the absorption spectrum at low temperature. Therefore, photoluminescence excitation (PLE) spectrum of CSI is investigated instead, as shown in the Chapter 6.

Chapter 6: Photoluminescence excitation spectrum of $CsSnI_3$: two-phonon processes

6.1 Introduction of the LO phonon features in PLE spectrum

Photoluminescence Excitation (PLE) spectroscopy is a useful and widely-used technique in characterizing electronic states in semiconductors. PLE experiment measures the variation of photoluminescence intensity at a particular wavelength, which is generally referred as detection position, over different excitation energies. Therefore, the intensity of the PLE spectrum at a particular wavelength is determined by two factors: 1) the absorption coefficient at this wavelength, and 2) the fraction of carriers or excitons which could relax to detection positions and then recombine radiatively. In most of bulk semiconductors, the electronic band is continuous, which is in favor of the intra-band transition of carriers through carrier-carrier and carrier-lattice relaxation process. The relaxation process of photo-generated carriers could be so fast that the carriers go through the so-called "thermalization" and cooling processes and reach the Boltzmann equilibrium before recombine radiatively. Therefore, the second factor is almost the same at different excitation wavelength, and the shape of PLE spectrum is mainly determined by the energy dependent absorption coefficient. However, things are different in low-dimensionally structured semiconductors, such as quantum dots [47], quantum wells [48], where the electronic states are quantized. Carrier-lattice scattering could be slow due to the lack of electronic states that satisfied both energy and momentum conservation conditions. This effect, named as "phonon bottleneck", could make the relaxation of hot carrier less efficient than radiative recombination, resulting different relaxation processes at various excitation wavelength. In this case, the second factor is important in determining the shape of PLE spectrum. Clear longitudinal optical (LO) phonon features were observed experimentally in the PLE spectrum

of a few quantum dots, [49, 50] single-walled carbon nanotubes, [51] and quantum wells under the condition that electronic states were separated by integer number of LO phonon energy.

As discussed in Chapter 5, the second order Raman scattering was resonantly enhanced by the two adjacent parallel lowest conduction bands separated by the energy of two LO phonons. As a result, it is nature to think, can we observe the LO phonon features in the PL and PLE spectrum? The intuition suggests that the two LO phonon assisted transitions should also be resonantly enhanced by the unique electronic band structure. However, the LO phonon feature is not observable in the PL spectra of CSI shown at Fig. 6.1, due to the large inhomogeneous broadening originated from the polycrystalline nature of the sample. In this chapter, we want to retrieve the information of the LO phonon feature from the study of the PLE spectrum of CSI.

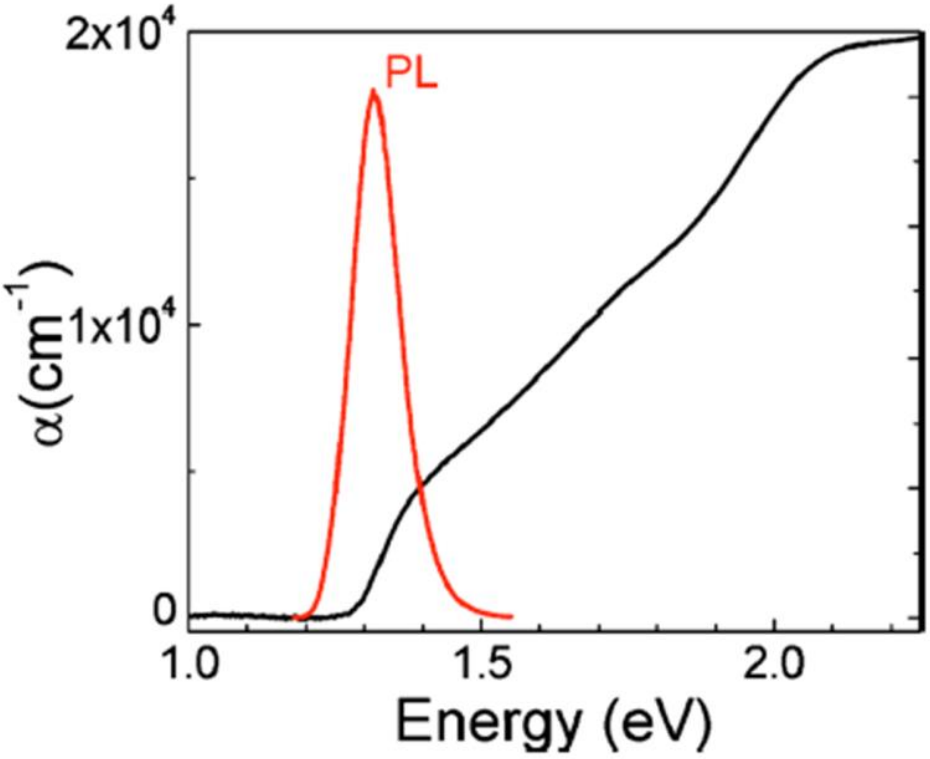

Fig. 6.1: Measured absorption and PL spectra of CSI at room temperature. The black line is the absorption spectra.

6.2 Comparison of Raman and PLE spectrum

It might be easy to get confused between PLE and Raman spectrum, as in both cases, the excitation and detection positions are very close. For Raman process, the incoming photon is "scattered" by the lattice, and thus the outgoing light is coherent with the incoming light. As shown in Fig. 6.2, virtual states have to be considered to explain Raman scattering. This is related to the fact that the interaction of the photon with the lattice and the re-emission of the scattered photon occur almost simultaneously. Therefore, the time scale for Raman scattering is very short, usually within a picosecond or less. However, the time scale for photoluminescence is much larger, usually within nanosecond region. For PL, the incoming photons are actually absorbed by electrons, and then thermalized to the lowest conduction band by interaction with phonons. Meanwhile, the photoluminescence intensity is usually much larger than Raman intensity. As a result, the Raman process and photoluminescence are two different processes.

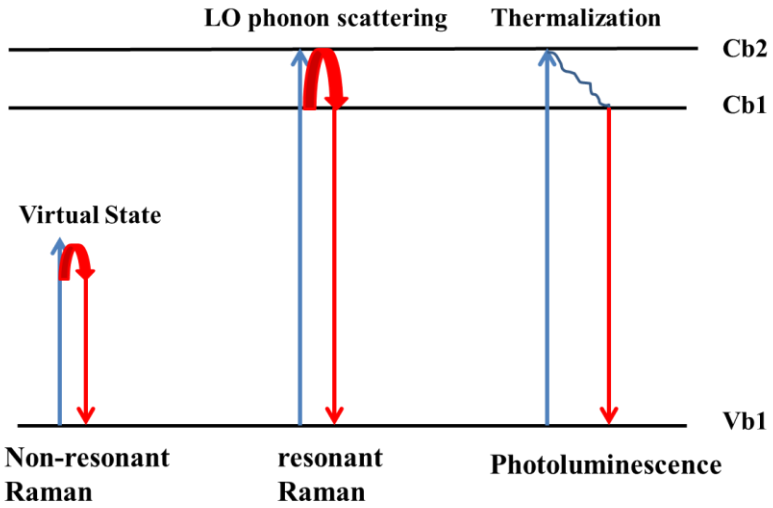

Fig. 6.2: Illustration of Raman, resonant Raman and photoluminescence processes.

6.3 The PLE spectra: two-LO-phonon assisted emission

The normalized PLE spectrum of $CsSnI_3$ at 12 K with the detection position 1009 nm, which is the peak position of PL spectrum at that temperature, is shown as in Fig. 6.3. The PLE spectrum has a very broad (about 80 meV FWHM) and asymmetry peak at about 70 meV away from the emission position, while at the high energy side, the spectrum is flat. This PLE spectrum is very different from the absorption spectrum shown as in Fig. 6.1, which is a typical absorption spectrum for bulk semiconductor material with three-dimensional density of states (3D DOS). The difference of the PLE and absorption spectrum indicates undoubtedly that the fraction of photon-generated carriers that could recombine radiatively at the detection position is different under different excitation light.

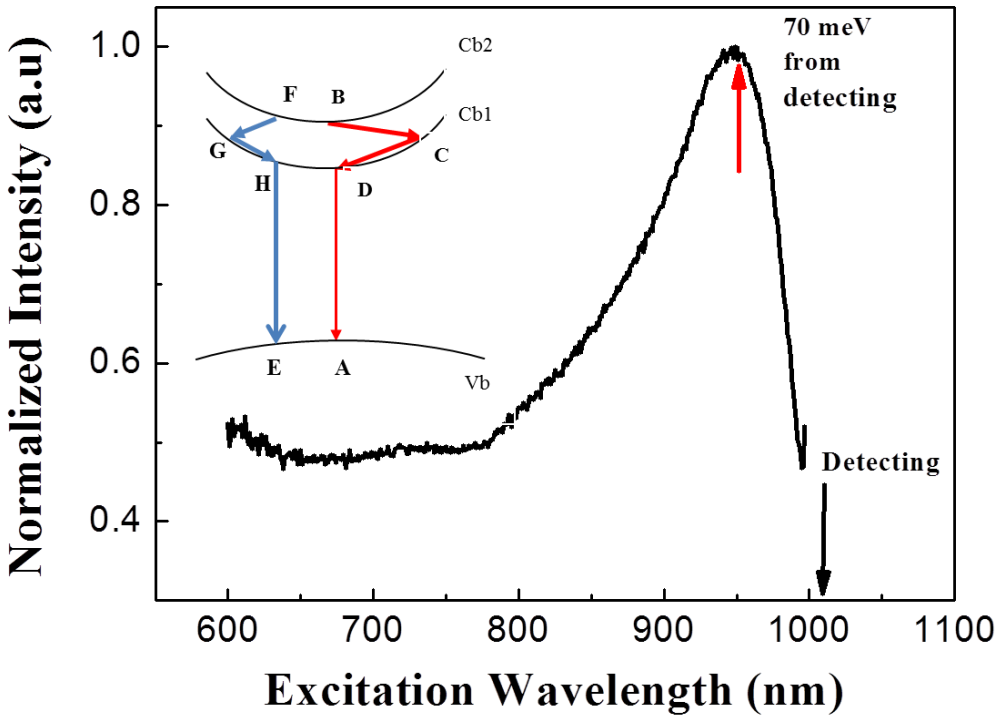

Fig. 6.3: The PLE spectrum of $CsSnI_3$ at 12 K with detection position to be 1009 nm, which is the peak position of PL spectra of CSI at 12 K. The schematic diagram for this PLE process is shown as in red arrow in the insert. The blue arrow represents for the case when the detection position is not peak of PL spectra.

We argue the peak of PLE spectra is due to the two LO phonon assisted emission which is resonantly enhanced by the unique two parallel conduction bands separated by the energy of two LO phonons. This process is shown as the transition path "B→C→D→A" in the insert of Fig.6.3. Just similar as the second order Raman scattering, all the transition intermediate states are real, and thus the transition probability are greatly enhanced. To theoretically show this scenario, the PLE spectra attributed to this process at detection position Ω_d is given as:

$$I(\Omega_I) \sim \sum_{\vec{q}} \left| \frac{\langle A|H_{e-R}|D\rangle\langle D|H_{el-ph}|C\rangle\langle C|H_{el-ph}|B\rangle}{(E_D - E_C + \hbar\omega_{LO}(q) + i\Gamma)(E_C - E_B + \hbar\omega_{LO}(q) + i\Gamma)} \right|^2 \times \delta(\Omega_I - \Omega_d - 2\hbar\omega_{LO}(q)) \qquad (6.1)$$

Where A, B, C, and D are possible real electronic states in conduction bands as shown in the Fig. 6.3. Symbols of $H_{e\text{-}R}$ and $H_{el\text{-}ph}$ represent the electron-radiation coupling and electron-phonon coupling Hamiltonian, respectively. Γ is a broadening factor that is related to the dephasing time of electronic states involved in this process. The Eq. 6.1 above is different from the Eq. 5.1 for the Raman process as the absorption transition from A to B is not a component of the process. When the energy of the intermediate states C, $E_C = E_B - 32$ meV = $E_D + 32$ meV, all three denominators (real part) in the expression is zero, and thus resonantly enhancement occurs.

Based on the Eq. 6.1, there are two indications about the PLE spectra if dominated by the two-LO-phonon assisted emission. First, the peak position of PLE spectrum should change simultaneously with the detection position, to satisfy the delta function in the Eq. 6.1. Second, the intensity should be proportional to the oscillator strength at the detection position, given the term of $\langle A|H_{e-R}|D\rangle$ in the Eq. 6.1. The relative oscillator strength manifests itself as the PL intensity at particular position. Therefore, the peak intensity of PLE spectra at different detection positions should be proportional to the PL intensity at the wavelength of the

detection position. We would verify our assumption through the detection position and temperature dependences of PLE spectrum study in the next two sections.

6.4 Temperature dependence of the PLE spectrum

The temperature dependence of the PLE spectrum is shown as in Fig.6.4. At different temperatures, we took the photoluminescence spectrum first to determine the peak position, which would then be set as the detection position. The measured signal was then normalized by the intensity of excitation light. As shown in Fig.6.4, the peak position of PLE shifts to shorter wavelength at increasing temperature, along with the blue shift of the detection position. The blue shift is caused by the positive temperature dependence of the electronic band gap of CSI as discussed in details in Chapter 4. The shift of peak position is consistent with the prediction of the two-LO-phonon emission model as we predicted in the section 6.4.

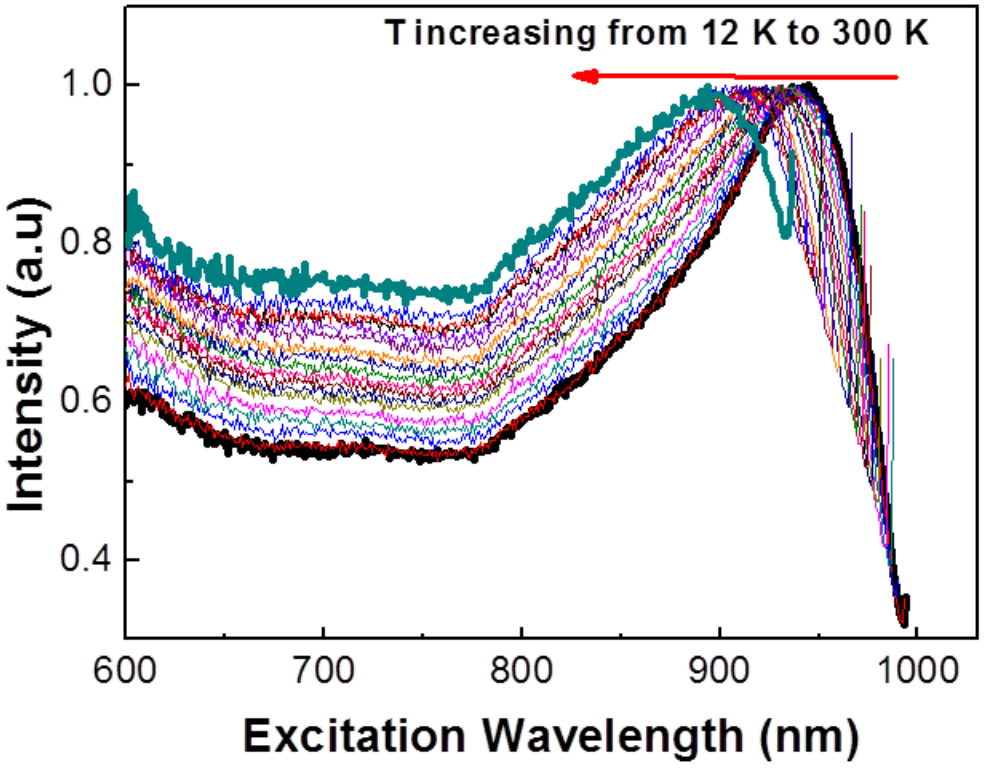

Fig. 6.4 PLE spectrum at various temperatures from 12 K up to 300 K. The spectrum from left to right corresponds to increasing temperature.

In order to analysis the peak intensity of the PLE spectrum, the PL spectrum taken at various temperatures from 10 K to 300 K is shown as in Fig. 6.5. The peak intensity of PLE spectrum and PL spectrum at various temperatures are shown as in Fig. 6.6. The peak intensity of PLE spectrum is proportional to the PL spectrum at low temperature (T < 100 K). However, as temperature gets higher (above 100 K), the PLE peak intensity drops faster than the PL intensity. This phenomenon is also consistent with our assumption of the two LO phonon process. As discussed in the introduction of this chapter, one necessary condition for the presence of LO phonon features in PLE spectrum is that the thermalization process should be slow enough. Otherwise, most of the photo-generated carriers would be cooled down to the quasi-equilibrium Boltzmann distribution before the radiative recombination, thus the fraction of excitons that could be recombined radiatively is the same for different excitation wavelengths. If that is the case, the radiative intensity at the detection position is just proportional to the number of photon-generated carriers and no LO phonon feature should be observed. The reason of the LO phonon features can be observed in CSI is because of the two parallel conduction bands, not only because of the resonantly enhancement of the two-LO-phonon emission, but also because the two parallel bands slows the thermalization process to the lowest of CB1. At low temperature, the electrons could be thermalized to the bottom of CB2 instead of CB1. In this case, if the excitation energy is close to CB2, the photon-generated electron is less likely to be thermalized, allowing the two-LO-phonon emission to occur. As the temperature increase, the thermalization would be enhanced by the increase of electron-LO phonon coupling. Therefore, the two phonons assisted emission become less dominant in the PLE process and the peak intensity of PLE drops faster than the PL intensity.

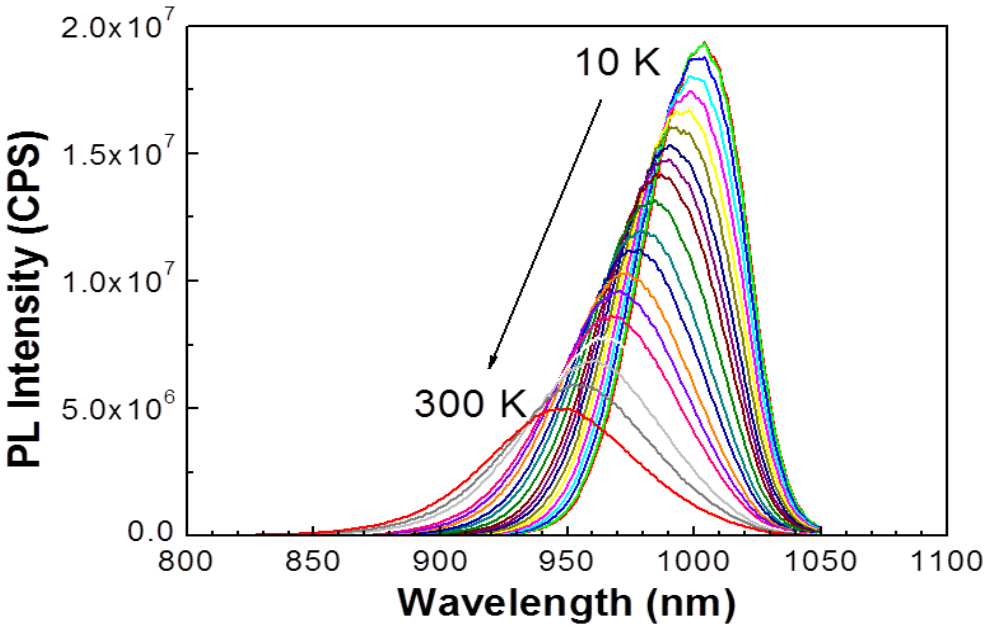

Fig. 6.5: The PL spectra of $CsSnI_3$ at various temperatures from 10 K to 300 K.

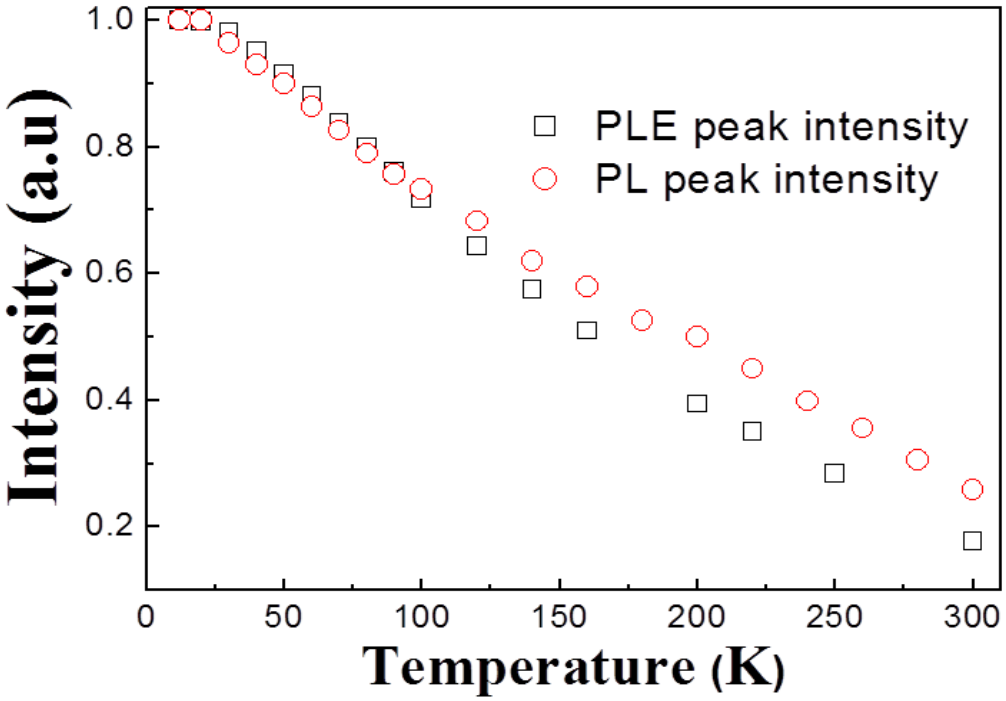

Fig. 6.6: The normalized peak intensity of PLE (black square dot) and PL (red round dot) spectra at various temperatures.

6.5 The PLE spectrum at different detection position

The detection position dependence of PLE spectrum is shown as in Fig. 6.7. One process of PLE with detection at off-resonant wavelength is shown as in the insert of Fig. 6.3 as the blue arrow F→G→H→E. The shape of the PLE spectrum at different detection position is identical. The peak position of the spectrum shifts along with the detection position. This observation is consistent with the first indication of the two-LO-phonon assisted transition in PLE process. The peak intensity of PLE spectrum at different detection position is shown as the black dot in the right side of the Fig. 6.7. Compared with the PL spectrum at 12 K with excitation wavelength 500 nm shown as the red line in Fig. 6.7, the peak intensity of PLE spectrum is proportional to the PL intensity at the detection position. This is consistent with the second indication of the dominant effect of the two-LO-phonon assisted emission in PLE spectra.

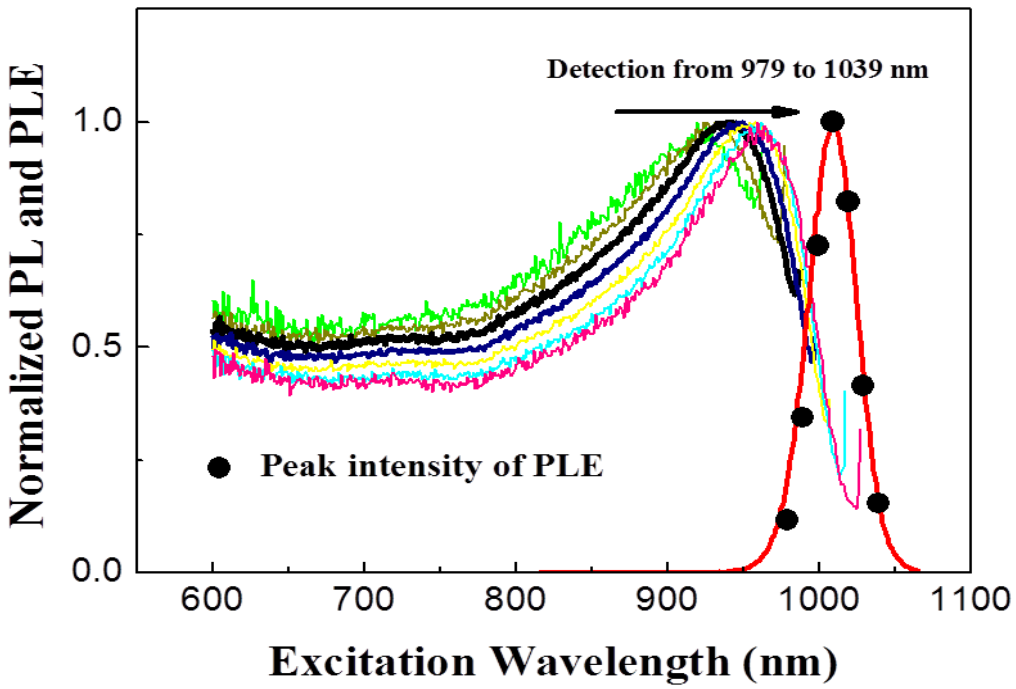

Fig. 6.7: PLE spectra at 12 K with various detection energy, 979, 989, 999, 1009, 1019, 1029 nm, from left to right respectively. The red line on the right side is the PL spectrum of $CsSnI_3$ thin film with excitation 500 nm at 12 K. The black dot represents the peak intensity of PLE spectra at various detection positions.

6.6 Summary

In summary, there are two necessary conditions for the existence of LO phonon features in PLE spectra: 1) band structures with separations of n times of Ω_{LO} which could resonantly enhance the n LO phonon assisted emission, and 2) slow "thermalization" process. In this chapter, the main peak of PLE spectrum of $CsSnI_3$ has been identified to be the two LO phonon assisted emission, through the detection position and temperature dependences study of PLE spectra. We have shown that the unique band structure of $CsSnI_3$ can resonantly enhance the two LO phonon process.

Chapter 7: Superfluorescence and superradiance theory revisited

7.1 Introduction of superradiance theory

Spontaneous emission of light is a fundamental process that plays an essential role in many phenomena in nature and forms the basis of many applications. The excited state in gas, atoms, molecule, nano-crystals and etc. couples with vacuum, and can transit to ground state, thus emit a photon. If all the excited state decays independently, the emitted light is incoherent light with random phases. This is the normal spontaneous emission. The decay rate is described by Einstein A coefficient and the radiation intensity is just proportional to the number of excited states, N.

However, if the excited states decay coherently, that is, the emitted light is in phase-related, as first predicted by R. H. Dicke [52] in 1954 in a two-level atomic system, some of the excited states can emit "super-radiantly". At the superradiant state, all the N atoms are correlated and the decay rate is enhanced by N times. The emission intensity of radiation is not proportionally to N, as one would expect from independent radiators, but to N^2. From the quantum mechanics point of view, when the dimension of the atomic system is small compared to the emission wavelength, the radiation field can be seen as constant in the range of atomic system. That is, all the atoms can sense the same radiation field and exchange photon with this common radiation field. In this case, the individual quantum number (excited state or ground state) of each atom is no longer good quantum number due to the exchange of photon between atoms. Instead, the whole atomic system should be treated as a huge radiation dipole and described in the coupling representation, just like the spin coupling system. If there is only two identical atoms separated by a distance smaller than the wavelength of emitted light, the situation is just in analogous to the coupling of two spin angular momenta. This coupled system would have two possible eigenstates: a superradiant

state that radiates twice as fast as single atom, and a subradiant state that does not radiate. The superradiant and subradiant states are analogous to the spin triplet state and singlet state, respectively.

Following the Dicke's notation, under the common radiation field, the total Hamiltonian of the system is:

$$H = H_0 + ER_3 + H_1 = H_0 + ER_3 - A(0)\cdot(\vec{e_1}R_1 + \vec{e_2}R_2) \tag{7.1}$$

where R_1, R_2 and R_3 are collective operators for the giant dipole,

$$R_k = \sum_{j=1}^{n} R_{jk}\ ,\quad k = 1,2,3 \tag{7.2}$$

The transition matrix for the state with coupled quantum number r and m is:

$$\langle r, m-1 | \vec{e_1}R_1 + \vec{e_2}R_2 | r, m\rangle = \frac{1}{2}(\vec{e_1} \pm i\vec{e_2})[(r-m+1)(r+m)]^{\frac{1}{2}} \tag{7.3}$$

Therefore, the decay intensity at the state described by r and m is:

$$I = I_0(r+m)(r-m+1) \tag{7.4}$$

The "superradiant state" is the state where r is large but absolute value of m is small. If we only consider the "superradiant state" with r = N/2, where N is total number of atoms. Let y be the total number of atoms at excited state, then m = y – n/2. Define the spontaneous life time for single atom as $\tau_0 = 1 / I_0$, then the Eq. 7.4 can be written as:

$$-\frac{dy}{dt} = \frac{y}{\tau_0}(n-y+1) \tag{7.5}$$

Therefore, the enhancement of the decay rate changes with the number of atoms at excited states. The Eq. 7.5 describes the scenario when all the atoms are perfectly correlated as r =

N/2. For an uncorrelated system, the rate of motion is just the equation for spontaneous decay $-\frac{dy}{dt}=\frac{y}{\tau_0}$. It is therefore natural to use a factor μ varying from 0 to 1 to describe the "degree of coherence" as shown in the Eq. 7.6. The essential physics of μ is the same as the "shape factor" to be discussed in a classical perspective of SR.

$$-\frac{dy}{dt}=\frac{y}{\tau_0}[\mu(n-y)+1] \tag{7.6}$$

From a classical point of view of SR, the emitted light of each atom is coherence light when the atoms are close to and initially in phase with each other. The net electromagnetic field is proportional to N and therefore the emitted intensity goes as N^2. In 1971, Rehler and Eberly [53] calculated the superradiant decay rate in atomic system through both quantum and classical treatment. The time evolution of the total energy of two-level atoms was derived and a shape factor μ that described the strength of the cooperative emission was introduced. In their work, all the atoms emit coherent light with fixed phase difference, controlled by the initial laser excitation. In this case, all the atoms are excited in the same way except only the time delays due to the finite separations between atoms. The fixed phase for each atom is $\vec{k}_1\cdot\vec{r}_j$, where $\vec{k}_1$ is the wave vector of excitation, and $\vec{r}_j$ is the position of the jth atom. The shape factor μ is dependent on the laser wave vector $\vec{k}_1$, indicating the correlation is introduced by the resonant (as implied by two-level atoms) laser excitation. The shape factor could be calculated given the positions of emitters and proper excitation-induced initial correlations. The classical picture of SR is shown as in Fig. 7.2. Therefore, the shape factor is closely related to the average phase difference $e^{i(\vec{k}-\vec{k}_1)\cdot\vec{r}}$ of different atoms.

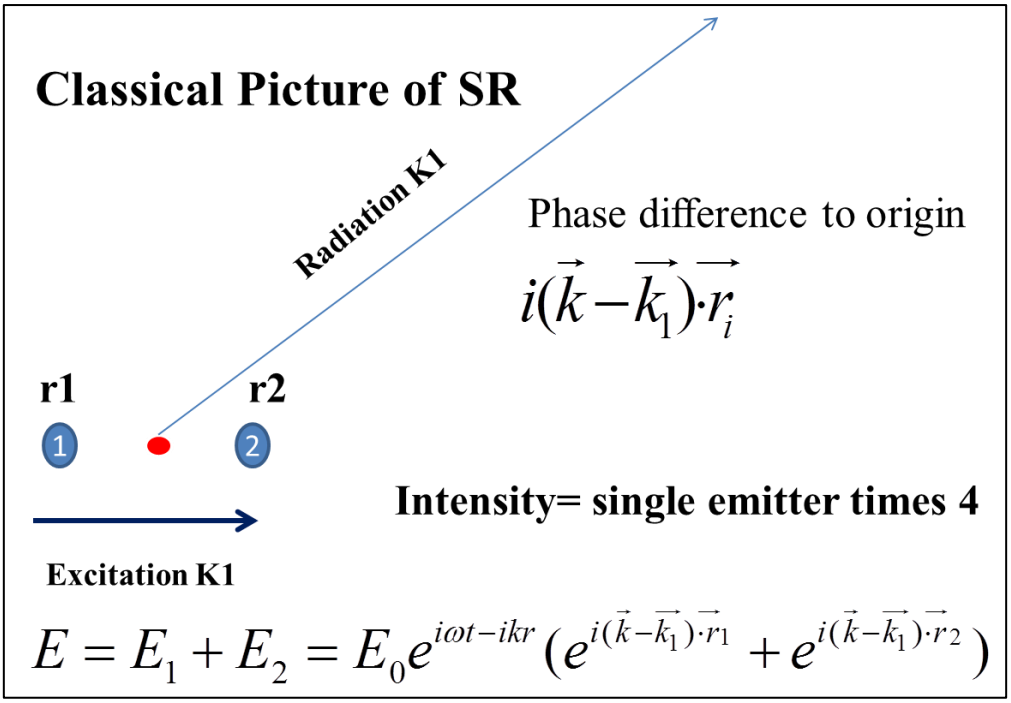

Fig. 7.1 Graphical description of SR from classical point of view is given.

Although Dicke restricted the superradiant state in a small region in atomic system and expected the decay rate to be significantly (three or more magnitude) larger than spontaneous emission, the concept of superradiance has been extended to all the systems [54-60] (quantum wells, bulk crystal, J-aggregates, etc.) with cooperative effects. Extensive theoretical works [61-67] have been made about the superradiant emission in all kinds of systems.

The decay rate of a superradiant system is proportional to the number of emitters N. However, the increase of decay rate with increasing N cannot last forever. Konester [64] firstly investigated the transition from superradiant excitons to stable polaritons in a cubic structure which consists of a stack of N identical monolayers. By considering only the crystal state that are modulated in the direction perpendicular to the slab (the z direction), he derived the dispersion relation of the coupled exciton-photon modes for a slab of arbitrary thickness. He demonstrated that the fundamental k = 0 mode showed superradiant behavior and that it had a maximum radiative decay rate when the crystal slab thickness was half a wavelength.

When crystal slab thickness is small, in the z direction, the wave vector is quantized due to the periodic boundary condition: $k = \frac{2\pi}{Na} m$, where m = 0,...N-1. The separation of the wave vector $\frac{2\pi}{Na}$ is much larger than the wave vector of photon $\frac{2\pi}{\lambda}$, when Na << λ . Therefore, the coupling with photon modes is the largest when the wave vector for exciton mode $k = 0$. The frame work of Konester was expanded and elaborated by Gunnar Bjork [63] and Chang-qi Cao [67], etc.

7.2 Superfluorescence and its relationship with superradiance

In all the theories described above, SR decay requires the initial coherence to be built up by the resonant excitation. The shape factor in Rehler and Eberly's work depends on the excitation wave vector k_1. In the thin slab system introduced by Konester, the superradiant mode has to be prepared initially. As the most exciting form of the cooperative effect, a special form of SR, superfluorescence (SF) decay was introduced to differentiate from the normal SR process [68]. SF is from an initially incoherent system, which later on spontaneously builds up a macroscopic dipole and then decay superradiantly. There is a transition from spontaneous to the cooperative emission in the SF process, named as delay time τ_d, which is inversely proportional to the number of excitons N [69]. The delay time, in which the coherence builds up spontaneously, is unique for SF. The difference between SR decay and ideal SF process (not consider dephasing) is illustrated as in Fig.7.2. Unlike SR that needs resonant excitation to build initial coherence, the SF process usually starts with off resonant excitation. The excited excitons go through very fast thermalization process from the initially excited position to the lowest point of conduction band, and then start to emit spontaneously. During the spontaneous emission process, excitons interact via the exchange of spontaneously emitted photons. This interaction process is similar to the stimulated

emission process in the sense that the remaining excitons are "stimulated" by the initial spontaneously emitted photons. At sufficiently high densities of excitons, this interaction process leads to an effective mutual phasing of excitons. As a result, a macroscopic polarization with amplitude proportional to density of excitons spontaneously formed. Of course, SF is different from stimulated emission since no gain is involved.

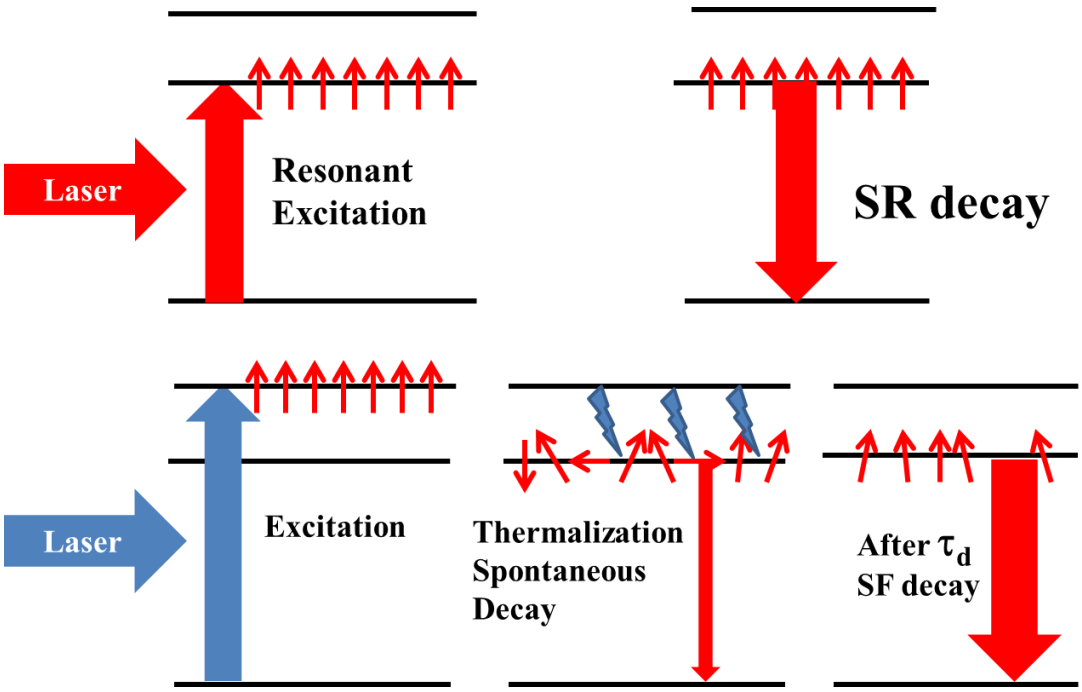

Fig. 7.2 Comparison of superradiant and superfluorescence processes is illustrated.

7.3 Our treatment of Superfluorescence

In literature, there are plenty of discussions about the SF behavior, such as the delay time, the peak intensity of the pulse, the SF decay rate. However, there has not been a complete framework that considers the time evolution of the SF process, including the coherence build-up and dephasing (both inhomogeneous and homogenous broadening) processes. In this chapter, we would like to study the time profile of SF decay, and discuss how the characteristics of SF (delay time, peak intensity, and decay rate) could change with the number of exciton N and inhomogeneous dephasing time T_2.

We use the derived equation of motion from Dicke's superradiance with the concept of the "degree of coherence", as shown in Eq. 7.6. The same equation can be derived under Rehler and Eberly's theoretical work [53]. The equation of motion in their work is given by:

$$-\frac{dW}{dt}=\frac{\mu}{\tau_0}(\frac{N}{2}+W)(\frac{N}{2}-W+\frac{1}{\mu}) \tag{7.7}$$

Where N is the total number of excitons, W is the total energy of the system and it changes with time, τ_0 is the spontaneous decay time and μ is the shape factor described before. In Rehler and Eberly's notation, if the exciton is at ground state, its energy is -1/2, if at excited state, the energy is 1/2. The total energy $W(t)=-\frac{N}{2}+y(t)$, where y(t) is the number of excited exciton at time t. Then we can get the same equation with Eq. 7.6.

$$-\frac{dy}{dt}=\frac{y}{\tau_0}(\mu(N-y)+1) \tag{7.8}$$

From equation (7.8), we can see that the decay rate of exciton is increased from the spontaneous emission by a factor of $\mu(N-y)+1$. If the cooperative effect is very strong and the shape factor μ gets close to 1, we can see the decay rate reaches maximum when only half of the excitons remain excited $y=\frac{N}{2}$. So the shape factor could be treat as a measurement of the "degree of coherence", and it varies from 0 up to 1. In the case of spontaneous emission, there is no cooperative effect $\mu = 0$, the equation goes back to the single exponential decay for spontaneous emission. Rehler and Eberly have analytically solved the equation (7.2) for a constant shape factor given proper initial condition, and have shown that the radiated intensity is mostly dominant by the exponential factor $e^{-t/\tau}$ with $\tau=\tau_0/(1+\mu N)$. The decay rate is enhanced by the factor (1+μN).

Although Rehler and Eberly's work is about two-level atoms which coherently excited by the external laser, we can apply the motion of equation into other systems. Their assumptions about the two-level atoms can give rise to the express of the shape factor μ as: $(1/N+\mu)I_0 = \int I_0(k)\left|\{\exp[i(k-k_1)\cdot r]\}_{av}\right|^2 d\Omega_k$. For different systems, the essential part of the equation is the shape factor μ that contains the information about how well the emitters cooperate in the emission. The shape factor μ is different given different excitation conditions, distribution of emitters (shapes such as line, thin slab, J-aggregates), and photon modes (cavity, vacuum).

Let us consider the coherence build up process for excitons in SF decay process. There are two key parameters determining the coherence between excitons in the SF decay: the cooperative frequency ω_c, and the dephasing rate introduced by both inhomogeneous and homogeneous broadening. The cooperative frequency ω_c is positively related to the exciton density N. Specifically, ω_c for a two dimensional excitons in quantum wells has been well studied to be [69-72]:

$$\omega_c = \sqrt{\frac{8\pi^2 d^2 N\Gamma_c}{\hbar n^2 \lambda L_{QW}}} \qquad (7.9)$$

Where d is the transition dipole moment, N is two dimensional exciton density, Γ is the overlap factor of radiation, $\hbar$ is the reduced Planck constant, n is the refractive index, λ is the wavelength, c is the speed of light, L_{QW} is the total width of the quantum wells. The other parameters other than density of excitons are constants, so we can simply use $\omega_c = A\sqrt{N}$, with A to be the constant coefficient. Notice that the build-up rate for coherence is a function of current density of excitons.

We now consider the influence of dephasing on coherence. At low temperature, the inhomogeneous broadening is dominant over the homogeneous broadening introduced by electron-phonon interaction. So we only consider inhomogeneous broadening for now. The inhomogeneous broadening factor is defined by [62, 73]:

$$H(t) = \frac{1}{N}\left|\sum_{l} \exp(i\Delta_l t)\right|^2 \tag{7.10}$$

Where Δ_l is the angular frequency detuning $\omega_l - \omega$ of the *l*th exciton. The time evolution of H(t) can be approximated by $\exp(-2t/T_2)$, where T_2 is the inhomogeneous dephasing time. As a result, the coherence of the system should be multiplied by $\exp(-2t/T_2)$.

To include both effect of coherence build-up process and dephasing process in the SF, the coherence of the system with initial exciton number N is given by:

$$\mu = \mu_0 \exp(\omega_c - 2/T_2)t \tag{7.11}$$

where μ_0 should be very close to 0 since the initial coherence of the system is 0; ω_c is given by $A\sqrt{N(t)}$, where N(t) is the current density of exciton. According to this equation, in order for the correlation to build up, we must have $\omega_c > 2/T_2$. Therefore, the density of initial excitons must exceed a critical density: $N > N_c = (\frac{2}{AT_2})^2$. As the emission continues, when t is very large and the density of excitons decrease below the critical density, the dephasing gradually destroys the coherence. Plug the equation (7.11) back into equation (7.8), we can calculate the time profile of the radiative intensity.

7.4 Ideal superfluorescence decay process

Let us first validate our model by neglecting inhomogeneous broadening (T_2 very large). In this case, the system should have SF decay, as shown in Fig. 7.3. In the calculations, we use the parameters, τ_0=1000 ps, $\mu_0 = 4\times 10^{-7}$, $A = 1\times 10^{-5}$. From the graph, the characteristics of SF decay gradually show up with increasing initial exciton number N. Even though there is no dephasing in this case, the coherence build up process still has to compete with the spontaneous emission that decreases the cooperative frequency ω_c. The delay time of SF peak decreases at larger N. The peak intensity and delay time as a function of N is shown as in Fig. 7.4. The peak intensity of the SF burst at sufficient large N is proportional to N^2, and the delay time of the SF peak is inverse proportional to N. The consistent of the result with the characteristics of SF phenomena further validates our model.

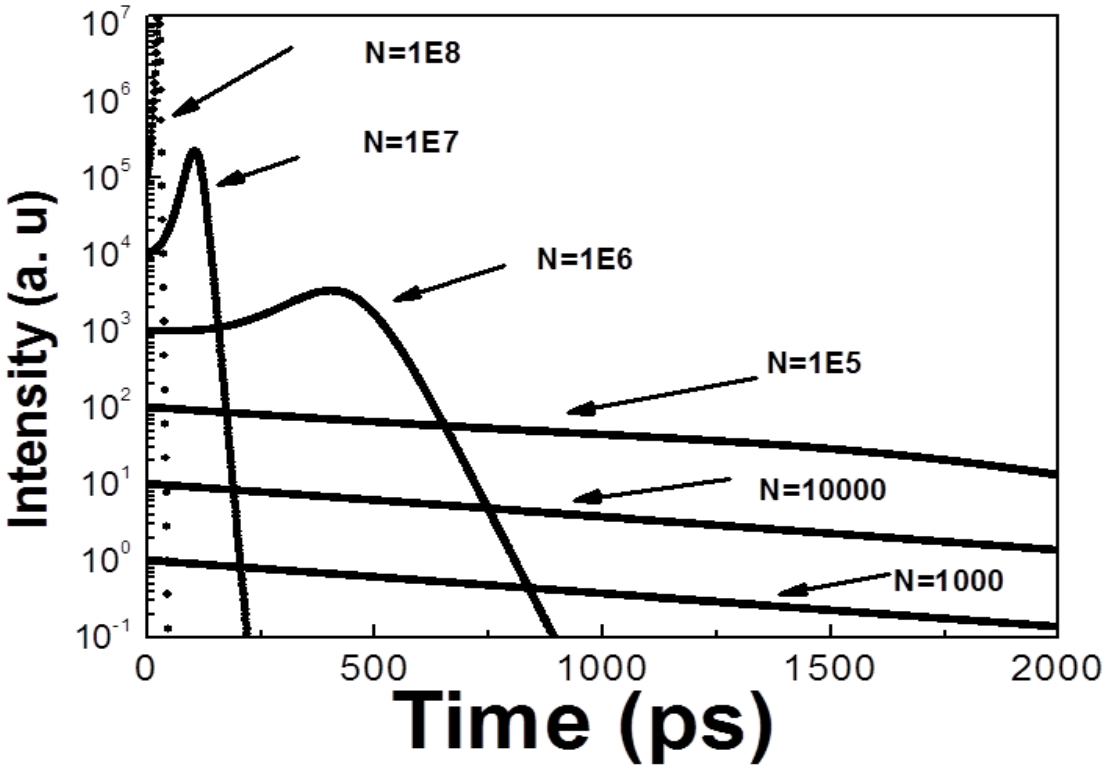

Fig. 7.3: Time evolution of radiative intensity with different initial number of excitons (N) for ideal SF decay.

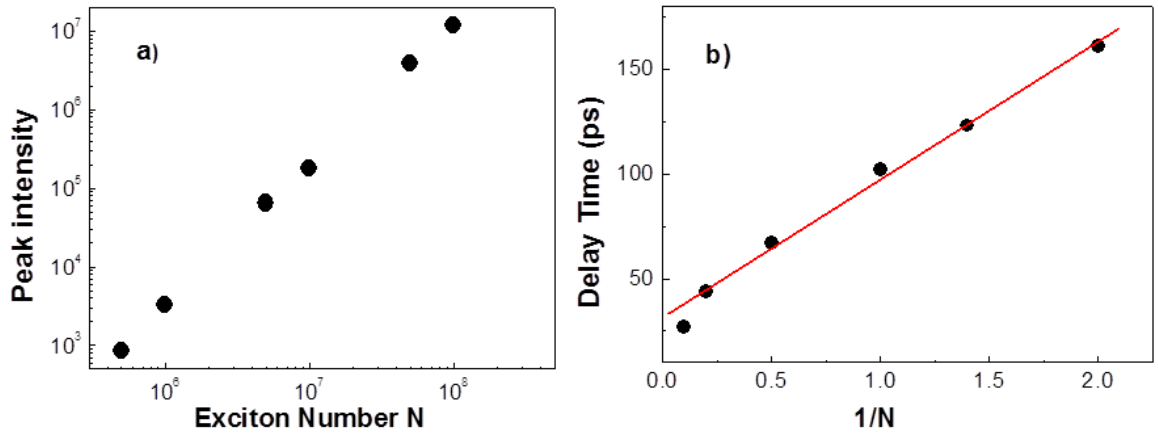

Fig. 7.4: a) The peak intensity of SF burst verse number of initial excitons N; b) the delay time of the peak of SF burst verse 1/N. The 1/N is multiplied by 10^7 for clarification purpose. The red line is not fitting and just for visualization purpose.

7.5 Superfluorescence decay with inhomogeneous dephasing

Now we need to include the inhomogeneous broadening effect for SF decay as shown in Fig. 7.5. In this calculation, we use the inhomogeneous dephasing time T_2 = 100 ps. Other parameters are the same as the calculation for Fig. 7.4. In order to satisfy the critical equation, $\omega_c > 2/T_2$, the initial N should be greater than $N_c = 4\times 10^6$, as shown in Fig. 7.5 that only for N larger than 4×10^6 could have SF burst. When N is sufficiently large, the coherence build up process is much faster than dephasing process, and then the decay is just the ideal SF as shown in Fig. 7.5 for large Ns. However, when the two processes are comparable, the decay starts with initial fast SF decay, and then change abruptly to normal spontaneous emission. This bi-exponential decay nature is special for SF emission with considerable inhomogeneous broadening effect. Notice that the slower decay in our model is the spontaneous decay process, not the subradiant decay that was claimed in Vasily V. Temnov's work [74]. According to Dicke's paper, exciton could emit superradiantly at the beginning and might get trapped in the "subradiant states" later. As some of the energy trapped in the subradiant states,

the decay rate is slower than the spontaneous emission rate. Both superradiant and subradiant are consequence of cooperative effect. In our analysis of SF, as the dephasing gradually destroys the coherence at low density of excitons, the slower decay should go back to spontaneous emission.

The delay time and peak intensity of the SF burst is plot as in Fig. 7.6 and 7.7, respectively. The delay time is still a linear function with 1/N even for the bi-exponential decay process. However, the peak intensity of SF burst is much more sensitive for the considerable dephasing effect. It is clear that the peak intensity for small N (bi-exponential decay in the Fig. 7.5 is reduced by the dephasing process. We also compared the decay rate for the initial fast decay for different N values as shown in Fig. 7.8. The SF decay rates at different N values are obtained through exponential fitting of the first fast decay process. From the graph, we can conclude that the decay rate is linearly related with the number of initial exciton density.

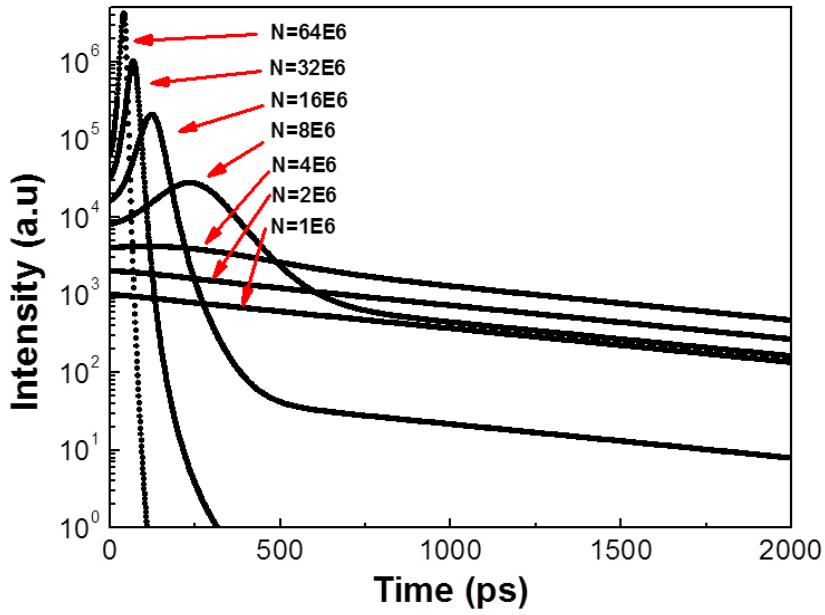

Fig. 7.5 Profiles of time evolution of radiative intensity are shown with different initial exciton numbers. Inhomogeneous dephasing time T2=100 ps was used in the calculation. The red arrows are for visualization purpose.

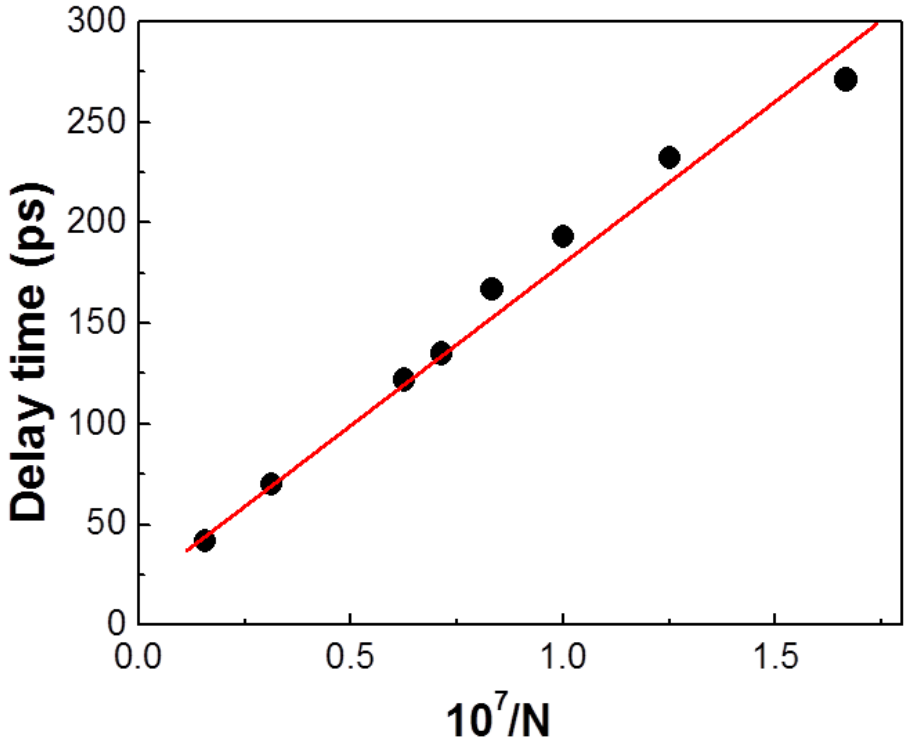

Fig. 7.6 Delay time is plotted as a function of 1/N. The red line is the linear fitting results.

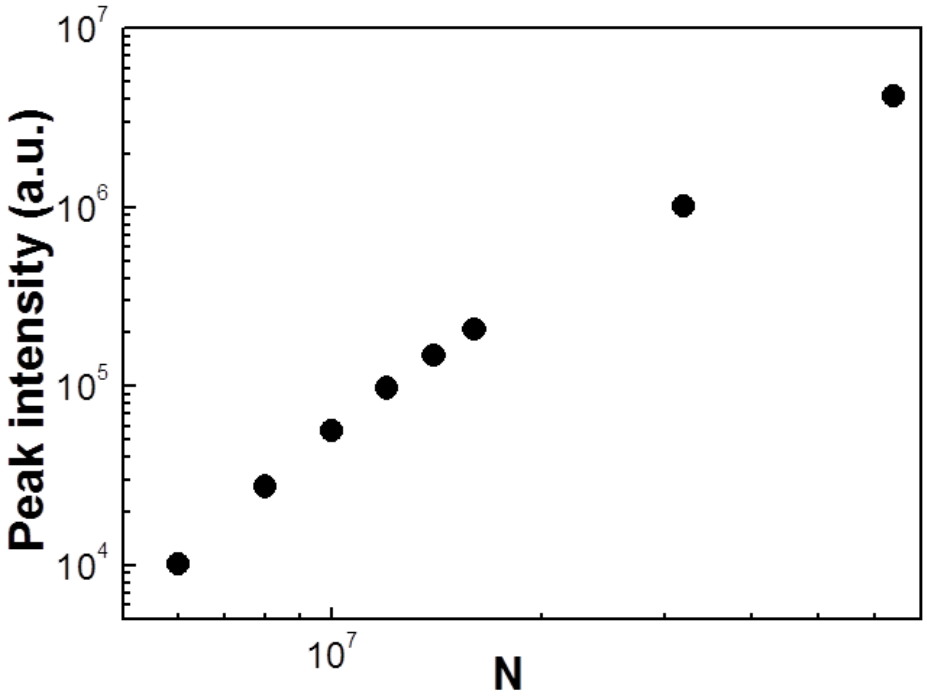

Fig. 7.7 The peak intensity vs. different initial number of excitons is plotted.

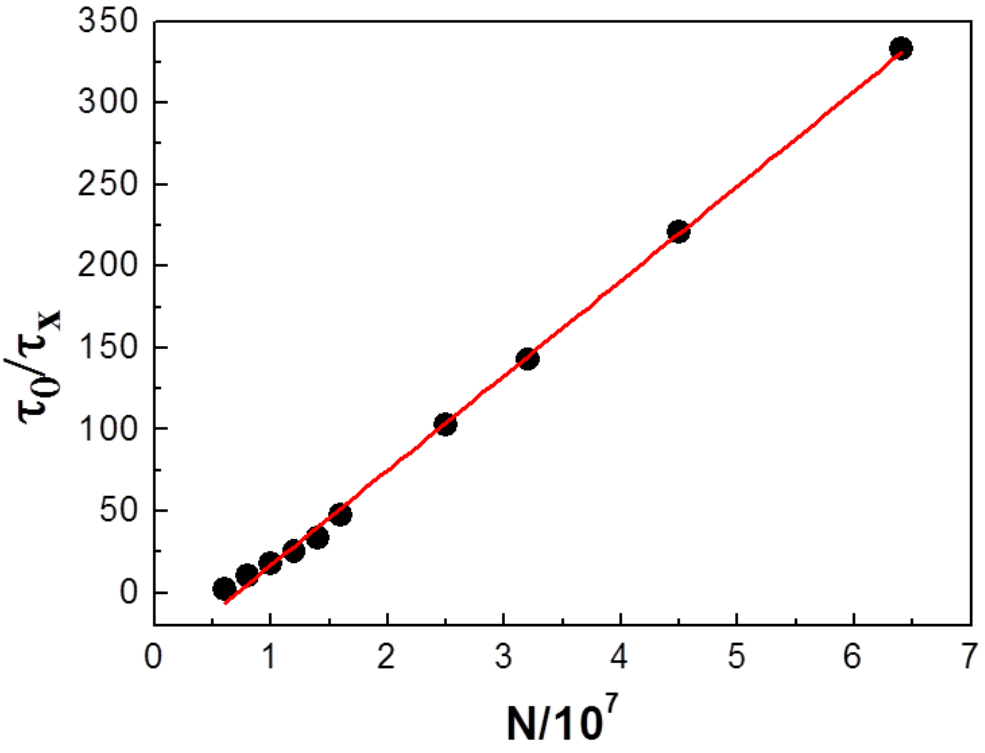

Fig 7.8 The enhancement of the SF decay rate over spontaneous emission at different N. The red line is the linear fitting.

7.6 Superfluorescence decay at different temperatures: the effect of homogenous dephasing

We can investigate the SF decay process at different temperatures in our framework by including the homogenous broadening effect in the dephasing term $1/T_2$. Since exciton-LO phonons interactions are the most effective way of relaxation, we only consider the dephasing caused by LO phonon, which should be proportional to the number of LO phonons $n_{LO} = \frac{1}{\exp(\hbar\omega_{LO}/K_BT)-1}$. The new term for $1/T_2$ should be:

$$\frac{1}{T_2} = \frac{1}{T_{20}} + \frac{1}{T_{LO}} \times \frac{1}{\exp(\hbar\omega_{LO}/K_BT)-1} \qquad (7.12)$$

where T_{20} is the inhomogeneous dephasing time, T_{LO} is the dephasing constant for LO phonon, and the last term is the number of LO phonons at temperature T.

The calculated temperature dependent profile is shown as in Fig. 7.9 a). In this calculation, the T_{20}= 200 ps, T_{LO}= 50 ps, N=1× 10^7, the energy of LO phonon used is 32 meV. The other parameters are the same as previous calculation. The Peak intensity and delay time of the SF pulse is plotted in Fig. 7.9 b). The peak intensity gradually decreases and delay time gradually increase at higher temperature. If we use the concept of "effective domain size" N_{eff} [75, 76], which is the number of perfectly coherent excitons in the system ($N_{eff}=\tau_0/\tau_x$), the peak intensity and delay time of SF burst should follow N_{eff}^2 and $1/N_{eff}^2$ rules. As a result, the coherence domain size is reduced by the exciton-LO phonon interaction at higher energy. The enhancement of the decay rate for the SF burst at each temperature is shown as in Fig. 7.10. We use the inverse of T to compare with the theoretical work by Francis C.Spano [76]. Our calculation result is very consistent with Spano's work. N_{eff} does not depend on the temperature until a certain threshold temperature is reached, at which point N_{eff} starts to decrease. The existing of threshold temperature is because of the discrete nature of the LO phonon band structure, i.e the number of optical phonon very small at low temperature. As the temperature increases, the Neff decreases linearly with the temperature till 1, which means spontaneous emission.

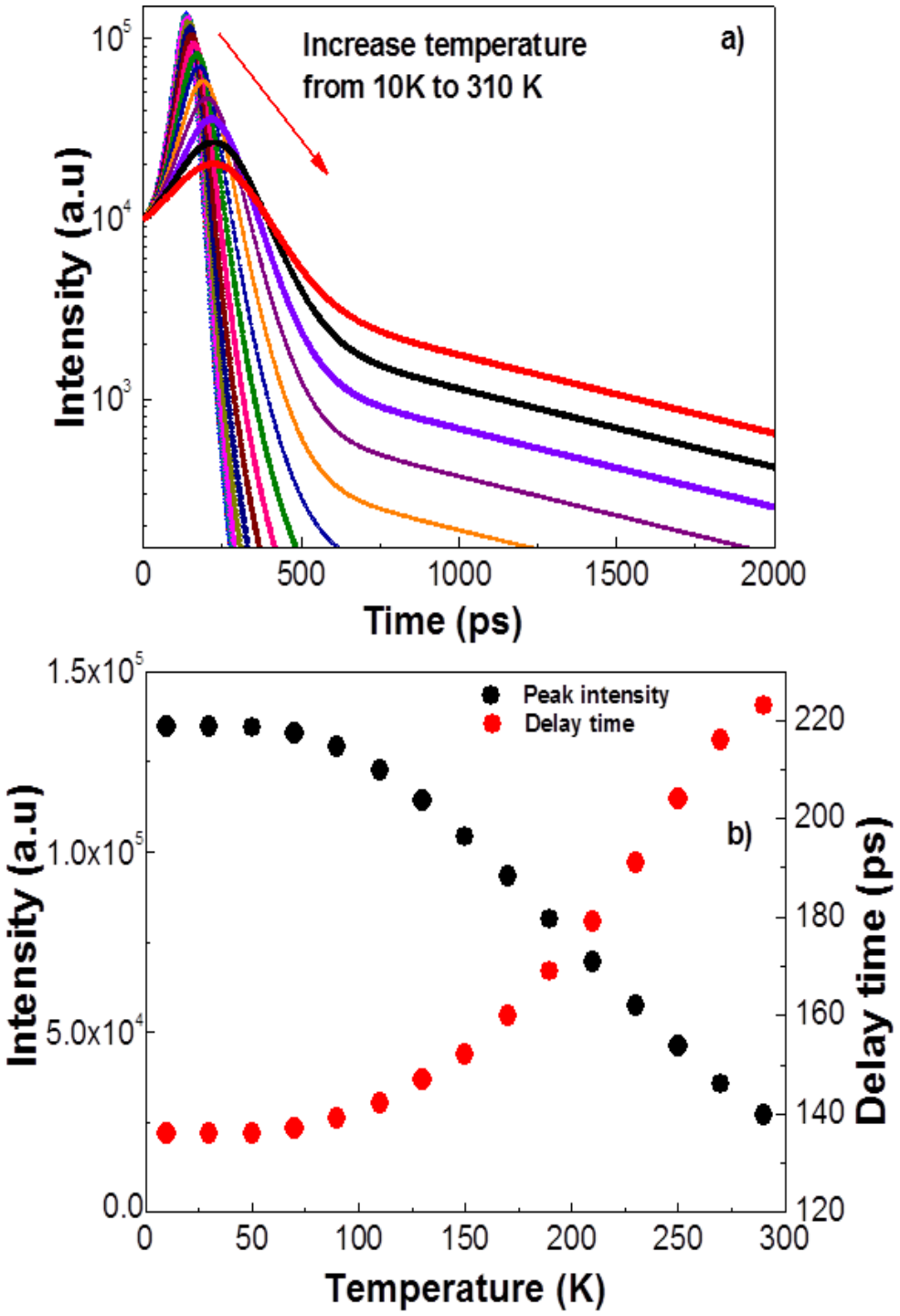

Fig. 7.9 a) The calculated SF decay process at various temperatures from 10 K to 310 K with separation of 20K. b) The peak intensity (black dot) and delay time of peak position (red dot) at various temperatures.

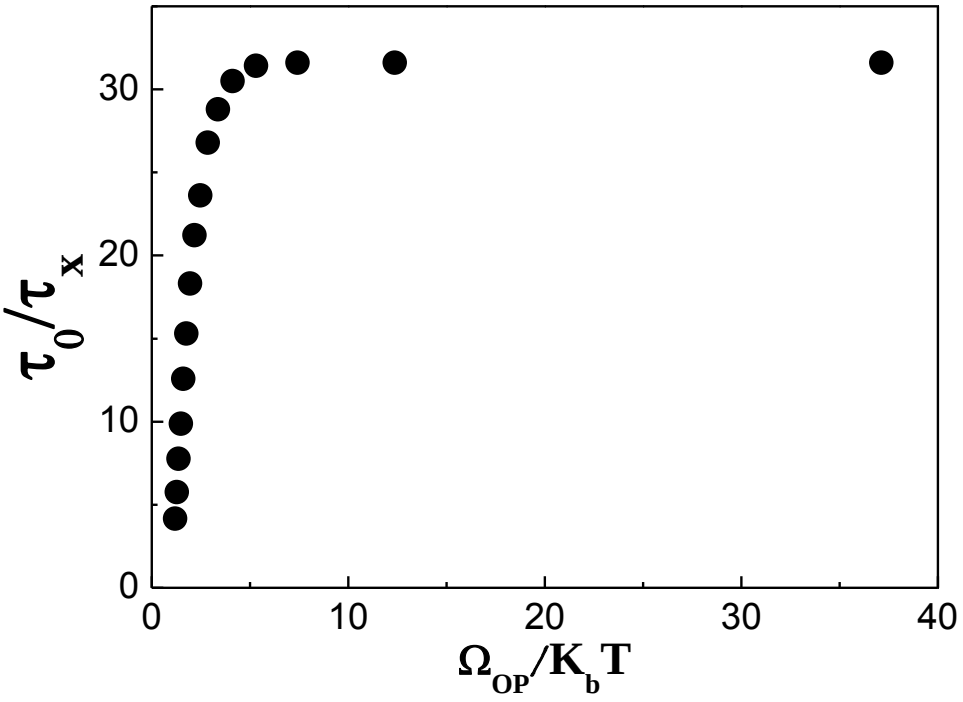

Fig. 7.10 Calculated enhanced decay rate over spontaneous emission as a function of 1/T.

7.7 Summary

In this chapter, we revisited the theory of SR and SF radiative emission. More importantly, we extended the motion of equation developed by Rehler and Eberly to describe the time evolvement of SF decay and developed the framework to include some effects that needs to be considered for experimental results, such as the inhomogeneous broadening and temperature effects. The peak intensity and delay time of SF burst have also been studied under our models.

We would apply the result of this chapter to explain the data of time resolved photoluminescence (TRPL) spectra with different excitation intensities and temperatures to be presented in the next chapter, and prove that the SF emission has been observed in the polycrystalline $CsSnI_3$ thin film.

Chapter 8: Superfluorescence in $CsSnI_3$: a manifestation of the correlation effect of natural 2D excitons

In Chapter 7, the theory and behavior of superfluorescence (SF) have been discussed. In this chapter, we would show the SF characteristics in the time resolved photoluminescence (TRPL) measurements of $CsSnI_3$ thin film. Possible reasons why CSI would have this coherent effect of excitons are discussed.

8.1 Experimental setup for time resolved photoluminescence

The TRPL is a contactless method to characterize recombination and transport in various materials and devices. Photoluminescence is measured by exciting a sample with a pulsed light source, and then measuring the subsequent decay in photoluminescence intensity as a function of time. Various techniques have been used to measure time-resolved photoluminescence such as up-conversion [77, 78] and streak camera [79] methods. We use the Time-Correlated Single-Photon Counting (TCSPC) technique. The laser pulse is split into two beams. The first beam triggers a time-amplitude converter (TAC) to start ramping up a voltage. The second beam excites PL from the sample. Some of the PL is passed through a long pass filter and monochromator onto a PMT. The first emitted photon to be detected by the PMT sends a stop signal to the TAC, and the TAC voltage is read and stored by a pulse height analyzer.The overall time resolution is about 200 ps for this system, mainly limited by the PMT used. The schematic set up for TRPL is shown as Fig. 8.1. The cryostat system in Fig. 8.1 is for low temperature measurements.

For all the TRPL measurements, the excitation light was from the picosecond laser with wavelength 532 nm. As a result, the excited excitons by absorbing photons goes through

the thermalization process and then reach the radiative states. So we need to use SF theory instead of normal SR theory to analysis our data.

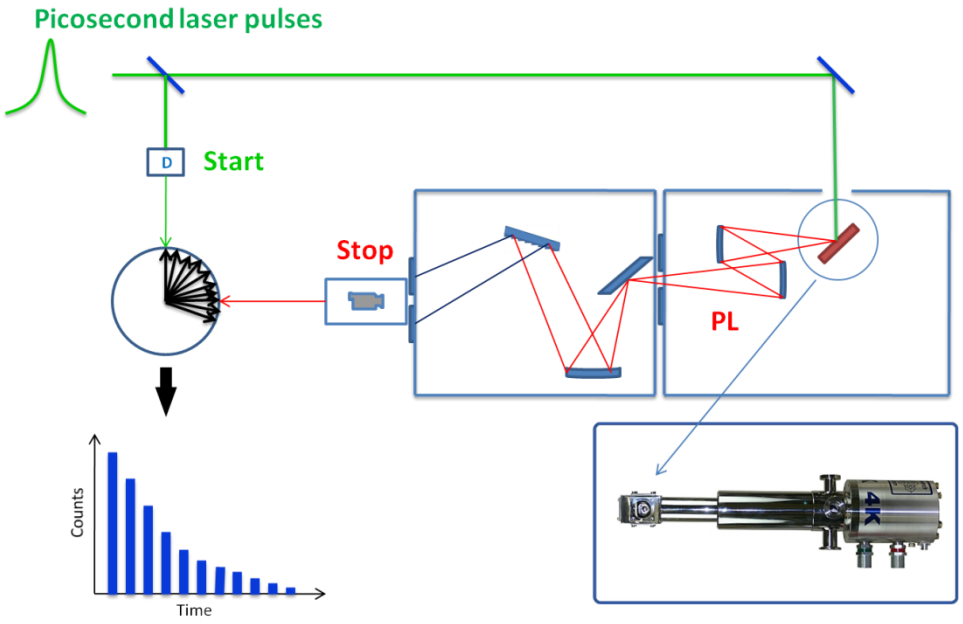

Fig.8.1: The schematic diagram for the set up of the TRPL measurement.

8.2 Power dependence of time resolved photoluminescence

The power dependence of TRPL measurements of CSI thin film deposit on a ceramic substrate is shown as in Fig. 8.2. The PL(t) was taken at 80 K for Pexc from 5 to 50 meW (10 meW corresponds to power density 0.3 W/cm^2). From the Fig.8.2, we can observe clear bi-exponential decay process: a intial fast decay followed by a slow decay process. We think the slow decay is the spontanous emission process with life time about 1 ns. This is consistent with one of the charteristics of SF decay with comparable inhomogenous broadening process.

We use the prediction of using our model Eq. 7.8 and Eq. 7.11, and convolute with system response give as G(t) to fit our experimental result shown as the red curve in Fig. 8.2:

$$G(t) = \exp(-t^2 / (2\sigma^2)) \tag{8.1}$$

G(t) is the impulse system response function with a variance of $\sigma = 200$ ps. The fitting results are shown as the red curve with $\sigma = 200$ ps used. All the other parameters for the fittings at various excitation is the same except the initial number of excitons N: spontanous decay life time $\tau_0 =$ 1000 ps, $\mu_0 = 1 \times 10^{-8}$, the coefficiant A for coherence build up rate is $A = 9 \times 10^{-6}$, the dephasing life time T_2 = 150 ps. As shown in Fig 8.2, the fitting quality is good for one order of magnitude, and fine tuning of the parameters is needed to future improve the fitting quality. For the calculated spectum, the ratio of the SF burst over the initial large intensity due to the spontanous emission is only within one order of magnitude, indicating the coherence is not strong. The blue curve for Fig 8.2 d) is the calculated result without the convolution with system response.

The decay rate for the initial fast decay process at various excitation power is shown as in Fig. 8.3 a). The decay rate of exictons is linearly related to the excitation power density. which should be proportional to exciton density if not saturated. However, the power depdenent steady PL study of CSI thin film to be shown later indicates the saturation effect when $P_{exc} > 10$ mW. As a result, the exciton density is not proportional, but linearly related to the excitation power density. The decay rate for the SF burst is ploted vs N, as shown in Fig. 8.3 b). This linear dependence of the decay rate on the exciton density is one of the indication of SF decay. From the data displayed in Fig. 8.3, the maximum enhancement factor, R_x/R_{x0}, for the exciton spontaneous emission rate at 80 K is about 5. This number is 4 times larger than the reported value of 1.3 at 2 K by Scheibner *et al.* [56] in a single layer of CdSe quantum dots. At larger excitation power density, the saturation effect would play a more important role as additional dephasing and non-radiative channel caused by the

exciton-exciton interaction. The saturation effect is studied through the power dependent steady PL study as shown in Fig. 8.4.

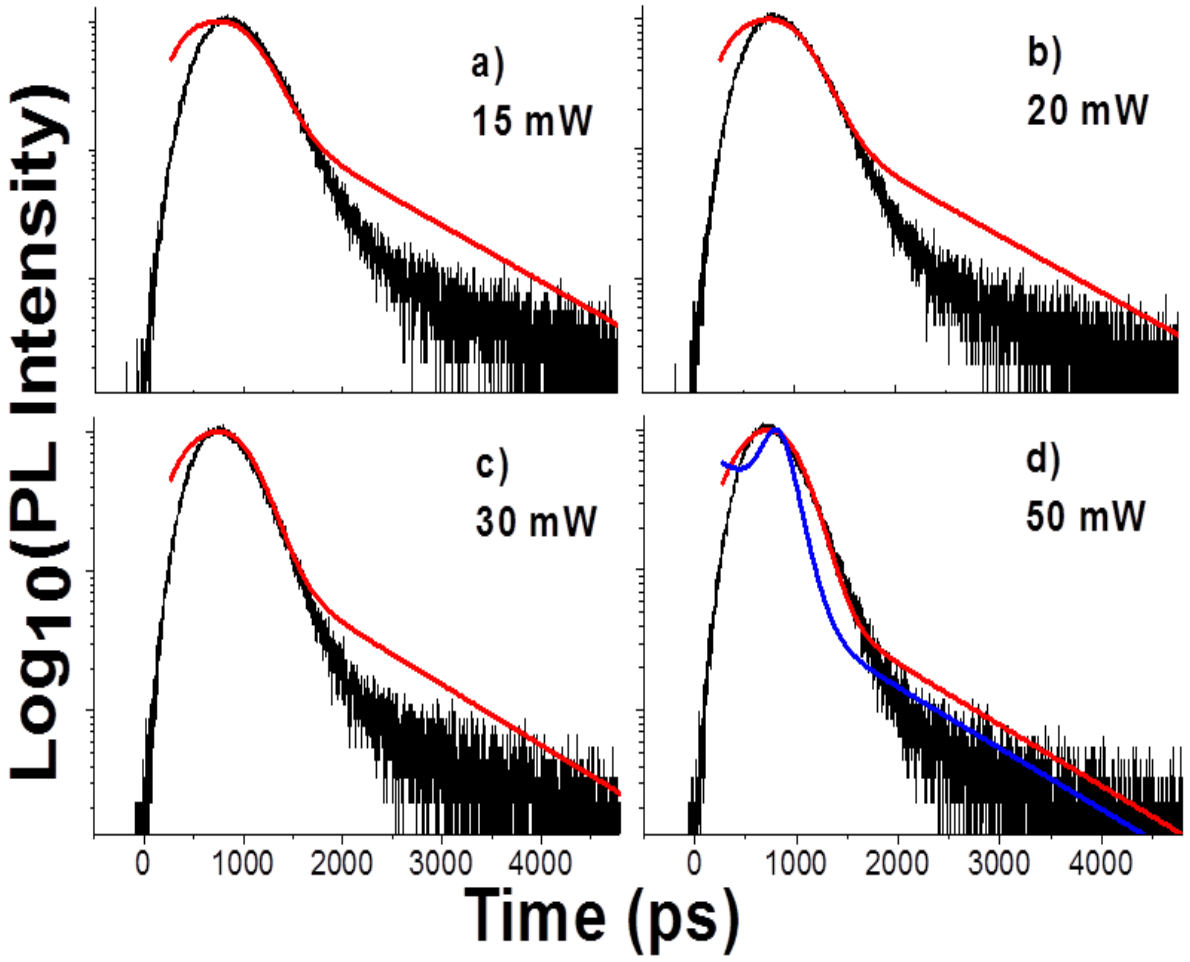

Fig. 8.2:PL(t) at 80 K taken at P_{exc} of 15 mW a), 20 mW b), 30 mW c), and 50 mW d). The thin red curve in each panel is calculated using our model after convolution with system response. The blue line in panel d) is the calculated result without convolution.

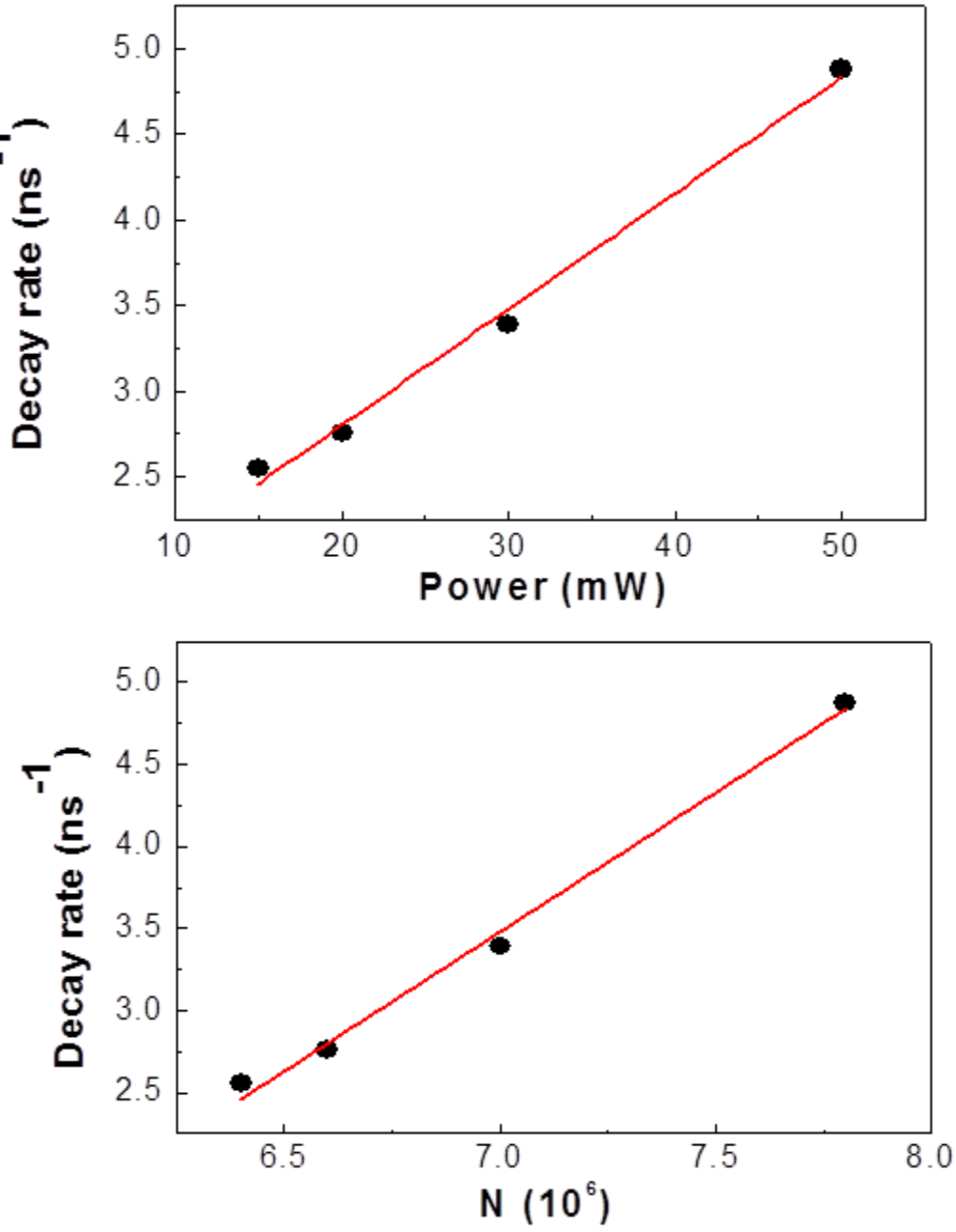

Fig. 8.3: a) Emission rates at 80 K under different Pexc levels. b) Emission rates with different initial number of excitons N. N is obtained by fitting the calculated spectrums with the experimental results under different Pexc. The red lines are linearly fitting of the decay rate.

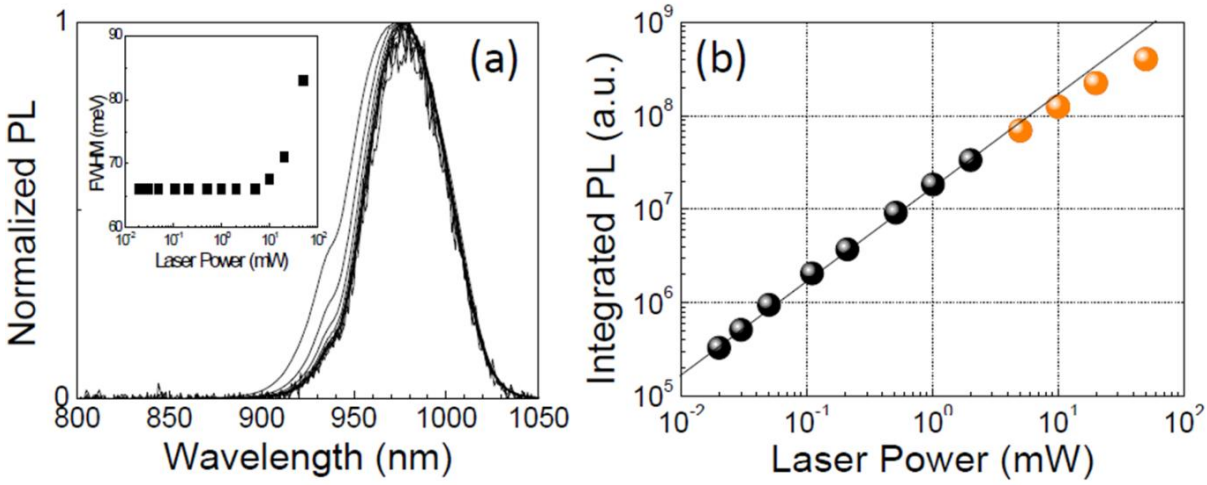

Fig. 8.4: (a) Normalized PL spectra at 80 K are shown as Pexc increases from 0.02 to 50 mW. The inset shows the PL FWHM as a function of Pexc. (b) Integrated PL intensity from the spectra in (a) vs. Pexc. The orange-colored data points indicate that at these excitation power levels PL(t) are shown in Fig. 8.3. The gradient of one is shown by the thin line indicating constant PL efficiency.

The evolution of the PL spectra at 80 K from another thin-film sample is shown in Fig. 8.4 (a) as P_{exc} increases from 0.02 to 50 mW. The PL spectra were collected by a fiber cable and were not spectrally corrected since we were only interested in relative PL intensity in this case. The apparent small spectral shoulder near ~ 940 nm is due to the fiber cable. The PL FWHM is displayed in the inset which remains roughly unchanged up to 20 mW and starts to increase rapidly as P_{exc} further increases. The PL FWHM is dominated by inhomogeneous broadening because of the polycrystalline nature of thin-films and the rapid increase of FWHM at high P_{exc} may arise from the laser-induced sample heating and exciton-exciton interaction. Integrated PL intensity vs. P_{exc} is shown in Fig. 8.4 (b) as solid spheres. The orange-colored data points indicate that at the P_{exc} levels of 5, 10, 20, and 50 mW, the time-resolved PL data are shown in Fig. 8.3. The gradient of one is also shown by the thin line indicating constant PL efficiency. From Fig. 8.4 (b), the saturation effect starts at P_{exc} larger than 10 mW.

As discussed in Chapter 7, the peak intensity of the SF burst is very sensitive to the fast dephasing process and deviate from the N^2 rule when the SF is not ideal. As a result, when P_{exc} > 10 meW and the saturation effect can not be neglected, the peak intensity of our data does not follow the N^2 rule. However, the delay time (the delay of the SF burst) is inversely related to the exciton density as shown as in Fig. 8.5. The red line is the linear fitted results with the inverse of exciton number 1/N. The inverse correlation between delay time and the exciton density is a unique characteristics for SF decay process.

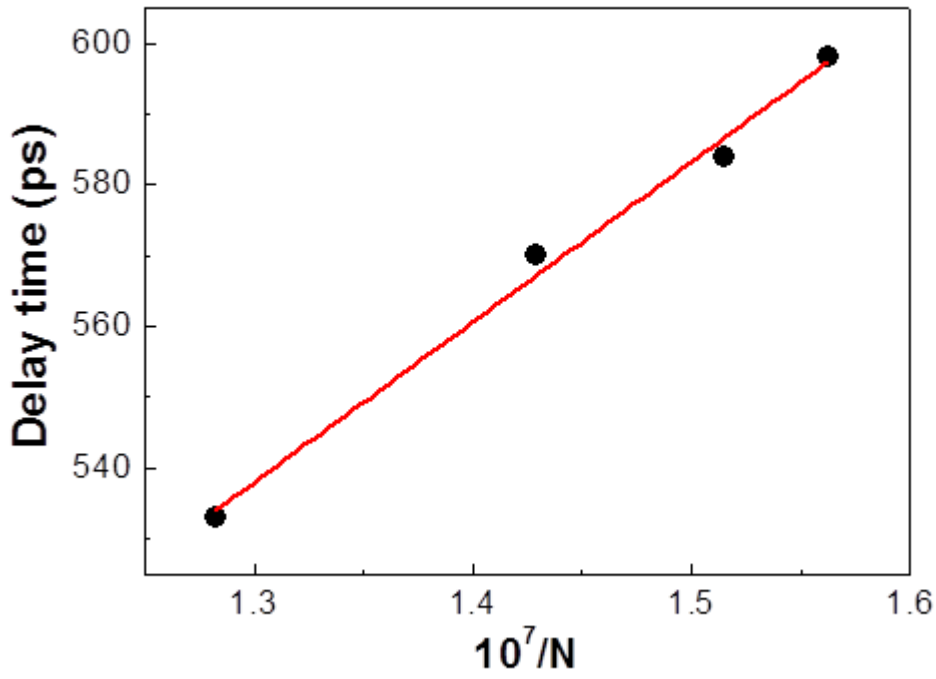

Fig. 8.5: The delay time of the SF burst over the inverse of different exciton numbers N. The red line is the linear fitting result.

8.3 Temperature dependence of TRPL

The temperature dependence of TRPL measurements taken from a different sample is shown as in Fig. 8.6. It seems that the bi-exponential decay process is not as aparent as in last section. This is because the sample-related inhomogenous dephasing rate is larger than the sample in the power dependence study. We use the standard fitting procedure to get the rise time and first fast decay rate by the convolution of the following F(t) and G(t) (defined as in Eq. 8.1), which are given below:

$$F(t) = \exp(-t/\tau_r)[1-\exp(-t/\tau_d)] \tag{8.2}$$

We are not using the same fitting method for this data because it is very difficult to obtain accurate fitting when the coherence effect is very weak. The fitting results for T = 100 K is shown as the red line in Fig. 8.6. The most interesting information is the temperature dependence of the decay rate shown as in Fig. 8.7. To be consistent with the presentation in the last section, we use the Ω_{op}/K_BT as the variable, where Ω_{op} is the LO phonon energy 32 meV for CSI, K_B is the Boltzmann constant. The red line in the graph is just for visualization purpose so that we can see very clear of the feature: the decay rate remains constant at low temperature up to 70 K and then decreases linearly with increasing temperature. This feature is exactly the same as the prediction of our model for SF decay at various temperatures when both inhomogeneous and homogenous broadening dephasing effects are included. This further indicates that in CSI, the main homogeneous broadening effect is from the exciton-LO phonon interaction.

To summary, in the section 8.2, the excitons emission of $CsSnI_3$ is proven to be the SF process from the following three facts: the bi-exponential decay nature, the linear relation between initial fast decay rate and exciton density, and the inverse relation between the delay time and the exciton density. In this section, we have shown that the temperature dependence of decay rate is exactly the same as predicted by our model of SF decay process. As a result,

we believe that we have identified the cooperative effect of excitons of CSI, and that the cooperative effects manifest itself as superflouresence. Eventhough the coherence is not very strong due to the large inhomogenous broadening oringated from the polycrystalline nature of our sample, we believe we could observe very strong SF decay process for the material of single crystal quality.

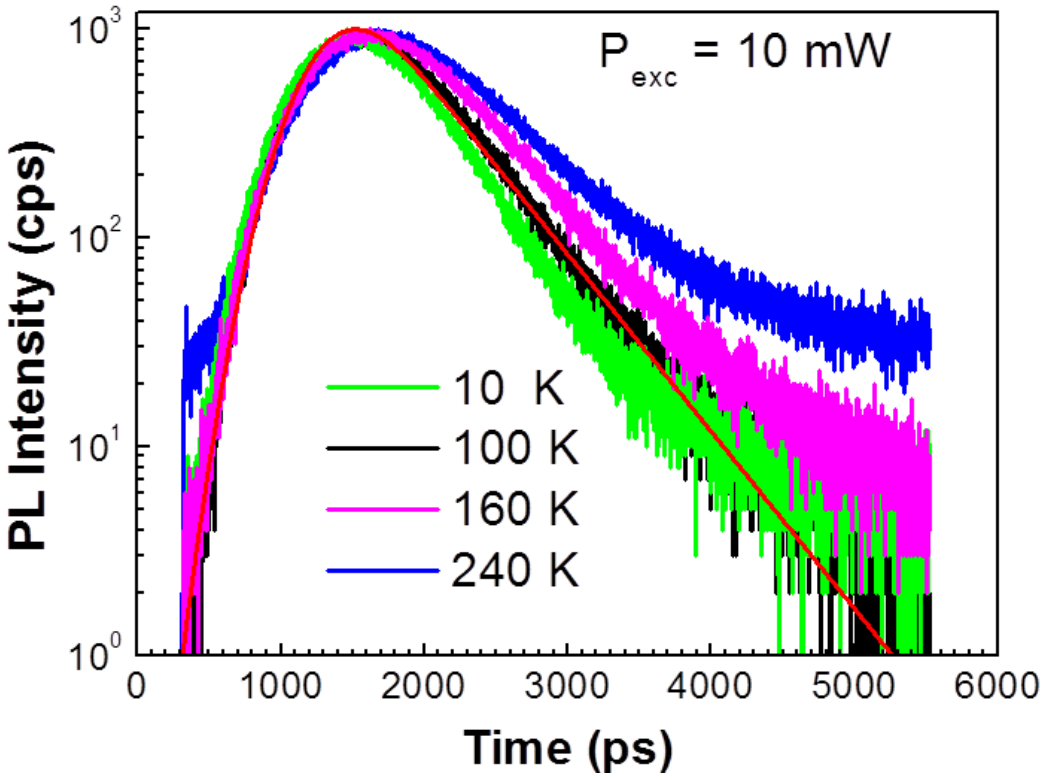

Fig. 8.6 PL(t) at various temperatures as indicated at Pexc = 10 mW which corresponds to the photoexcitation power density of 0.3 W/cm2. The thin red curve is calculated to fit the PL decay profile at 100 K.

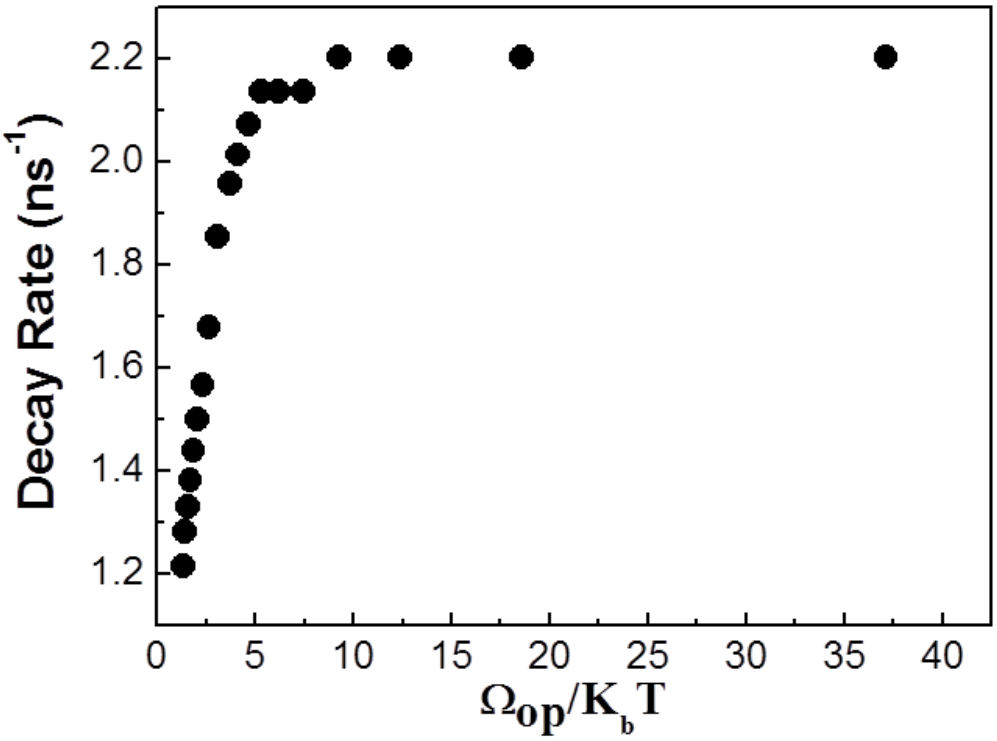

Fig. 8.7 The decay rate is plotted at various temperatures (1/T) of CSI thin film. Ω_{op} is the energy of LO phonon, 32 meV is used. K_b is the Boltzmann constant. The decay rate remains constant for temperature below 70K and decrease linearly with temperature.

8.4 Why can SF exist in $CsSnI_3$?

As mentioned before, the inhomogenous broadening is large for our sample because of the polycrystalline nature. So why can we observe SF process in CSI intead of other typical semiconductors? There has not been much experimental observation of SF process as SR because of the difficulty to achieve coherence for a initial uncorrelated system. As discussed before, the critical condition to achieve SF is that $\omega_c > 2/T_2$. For bulk material, even when the sample quality is great and the inhomogenous broadening could be neglected, the build up rate for coherence is limited by three dimensional density of states of excitons, which is proportioan to $\sqrt{E - E_{ex}}$. One way of increasing the exciton densitys at the lowest energy is to use quantum wells placed in a strong magnetic fields as the work of Y. D. Jho group

[70-72]. The density of states could be enhanced by the strong magetic field (energy level quantizing) and the reduced dimensionality (constant two dimensional DOS).

For CSI, even though the large inhomogenous broadening, the SF process can still be observed because of the extraordinary large exciton density, shown as the extraordinary large PL intensity. The comparison of the PL intensity of polycrystalline CSI thin film and the single crystal InP wafer was shown as in Fig. 1.3. In fact, we have not find any other common semicondutor that could have compariable PL efficiency with CSI. We believe that the large exciton density is because of the formation of the natural two dimensional (2D) excitons in the planes of SnI_4 tetragons. Similar effects of natural 2D excitons have been reported for PbI4 [80, 81] and $PbCl_4$-based [82] inorganic-organic hybrid materials. However, the reason of the formation of 2D excitons still awaits further investigations.

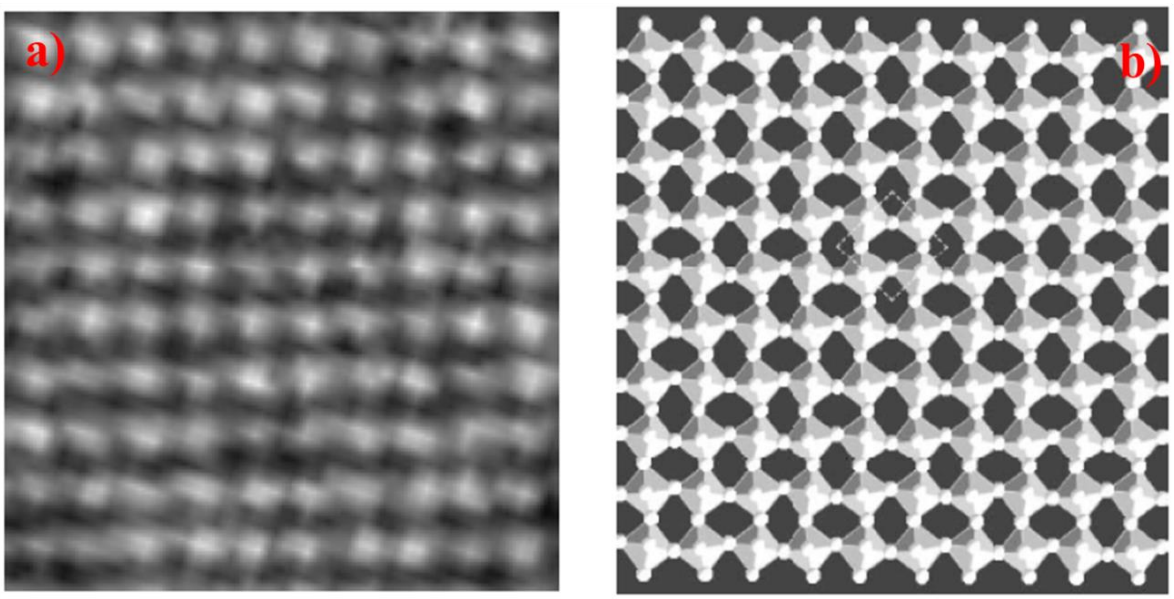

Fig. 8.8 (a) High resolutions TEM in a selected area for a CSI film on ceramics substrate. (b) Theoretically generated 10 × 10 octahedra with tin atoms at the centers and iodine atoms at vertices, projected in to a xy plane with x = [-1 1 0] and y = [1 1 0].

If our assumptions about the 2D excitons confinement is true, the SF emission in CSI occurs in the following steps. 1) The excitation photons (non resonant excitation 532 nm) are obsorbed by CSI and produces free carriers or non-equilibrium excitons. The obsorption

spectrum for CSI is typical for direct band gap semiconductor with 3D density of states. 2) The non-equilibrium excitons are thermalized to the lowest conduction band and then constrained in the 2D SnI_4 tetragons. 3) The formation of 2D excitons increases the density of states for the emission states near K = 0, capable to be filled with more excitons. More importantly, the confinement of absorbed 3D exciton in to 2D planes would greatly enhanced the exciton density. 4) The exciton density exceed the critical density for SF process N_c and the coherence of excitons are gradually build up during the initial spontanous emission process. 5) After a time delay of τ_d, the SF burst occurs with enhanced radiative decay rate. 6) After the most of excitons have recombined, the inhomogenous broadening gradually destroys the coherence and the decay goes back to spontanous emission for residual excitons.

Chapter 9: Conclusions

In conclusion, we have explored the peroskite compound $CsSnI_3$, a new semiconductor material which was identified by our group. We believe that it has a great potential in photonic device applications. Many interesting optical properties fundamentally rooted from the unique landscape of electronic states in CSI have been discussed in details. In my thesis, the exploration of CSI can be grouped into the following three parts.

The first part of the exploration started with the basic atomic structures of CSI. We adopted the first principles calculations to investigate the change of atomic symmetry of CSI at different temperatures. The fine structure information of γ state of CSI was obtained by the total energy calculations, and then compared with the available experimental data. With the detailed structure information, the electronic states of γ structure have been calculated. Several charcteristics of the electronic energy band diagram were identified, such as the large effective electron mass and the unique two parallel conduction bands with the energy seperation of ~ 64 meV.

The second part of my thesis deals with the abnormal temperature dependence of the band gap of CSI, which was determined by the photoluminensence study. This behavior was explained by the combination of the following two considerations: 1) the neglegible contribution of direct electron-phonon interaction to the band gap change due to the unusual large electron effective mass, and 2) the positive thermal expansion effect to the band gap change demonstrated by the theoretical calculations. We have also observed large two-LO phonon features in both Raman and photoluminescence excitation spectroscopy. The two-LO-phonon features are originated by the unique band structure: two parallel conduction band with separation close to the energy of two LO phonons. The two-LO-phonon features

have been identified as the triply resonant second order Raman scattering and two-LO-phonon assisted emission for PLE spectra, respectively.

The final part of my work involves the most exciting phenomenon in emission: superfluorescence in CSI. After revisiting Dicke's superradiance theory and combining the characteristics of SF, we have developed a model to describe the time evolution of SF radiation. This model predicts the bi-exponential decay feature if considerable dephasing rate is present. Meanwhile, the SF burst intensity, delay time, and decay rate have been studied by using the model. The SF emission in CSI was revealed through the power dependence and temperature dependence of time resolve photoluminescence measurements. The emission was proven to match all the characteristics of SF predicted by our model, such as the bi-exponential decay, the inverse relation of delay time over N, the linear relationship of decay rate with N, and the temperature profile of decay rate. We believe that the confinement of excitons in the two dimensional SnI_4 tetragons is the reason for SF in CSI.

References

[1] D. Scaife, P. Weller, and W. Fisher, "Crystal preparation and properties of cesium tin (II) trihalides," *J. Solid State Chem.*, vol. 9, pp. 308 – 314, 1974.

[2] P. Mauersberger and F. Huber, "Structure of caesium triiodostannate (II)," *Acta Cryst.* ***B***, vol. 36, pp. 683 – 684, 1980.

[3] K. Yamada, S. Funabiki, H. Horimoto, T. Matsui, T. Okuda, and S. Ichiba, "Structural Phase Transitions of the Polymorphs of CsSnI 3 by Means of Rietveld Analysis of the X-Ray Diffraction," *Chem. Lett. (The Chemical Society of Japan)* vol. 20, p. 801, 1991.

[4] K. Shum, Z. Chen, J. Qureshi, C. Yu, J. J. Wang, W. Pfenninger, N. Vockic, J. Midgley, and J. T. Kenney, "Synthesis and characterization of $CsSnI_3$ thin films," *Appl. Phys. Lett.*, vol. 96, p. 221903, 2010.

[5] I. Chung, B. Lee, J. He, R. P. H. Chang and M. G. Kanatzidis, "All-solid-state dye-sensitized solar cells with high efficiency," *Nature*, vol. **485**, pp. 486-489, 2012.

[6] J. Burschka, N. Pellet, S.J Moon, R. Humphry-Baker, P. Gao, M. K. Nazeeruddin and M. Grätzel "Sequential deposition as a route to high-performance perovskite-sensitized solar cells," *Nature*, vol. 499, p. 316, 2013.

[7] K.Yang, W. Setyawan, S. Wang, M. B. Nardelli, and S. Curtarolo "A search model for topological insulators with high-throughput robustness descriptors," *Nature materials*, vol. 11, p. 614, 2012.

[8] M. D. Peel, S. P. Thompson, A. Daoud-Aladine, S. E. Ashbrook and P. Lightfoot, "New Twists on the Perovskite Theme: Crystal Structures of the Elusive Phases R and S of $NaNbO_3$," *Inorg. Chem.*, vol. 51, p. 6876, 2012.

[9] P. Li, S. Ouyang, G. Xi, T. Kako, and J. Ye, "The Effects of Crystal Structure and Electronic Structure on Photocatalytic H2 Evolution and CO2 Reduction over Two Phases of Perovskite-Structured $NaNbO_3$," *J. Phys. Chem. C.*, vol. 116, p. 7621, 2012.

[10] F. Blanc, D. S. Middlemiss, L. Buannic, J. L. Palumbo, I. Farnan and C. P. Grey, "Thermal phase transformations in LaGaO3 and LaAlO3 perovskites: An experimental and computational solid-state NMR study," *Solid State Nucl. Magn. Reson.*, vol. 42, p. 87, 2012.

[11] M. N. Iliev, M. V. Abrashev, H. G. Lee, V. N. Popov, Y. Y. Sun, C. Thomsen, R. L. Meng, and C. W. Chu, "Raman spectroscopy of orthorhombic perovskitelike $YMnO_3$ and $LaMnO_3$," *Phys. Rev.* ***B.***, vol. 57, p. 2872, 1998.

[12] I. Borriello, G. Cantele, and D. Ninno, "Ab initio investigation of hybrid organic-inorganic perovskites based on tin halides," *Phys. Rev.* ***B.***, vol. 77, p. 235214, 2008.

[13] S. J. Clark, M. D. Segall, C. J. Pickard, P. J. Hasnip, M. J. Probert, K. Refson, M. C. Payne, "First principles methods using CASTEP," *Z. Kristall.*, vol. 220, p. 567, 2005.

[14] N. Troullier and J. L. Martins, "Efficient pseudopotentials for plane-wave calculations," *Phys. Rev.* ***B.***, vol. 43, p. 1993, 1991.

[15] H. J. Monkhorst and J. D. Pack, "Special points for Brillouin-zone integrations," *Phys. Rev.* ***B.***, vol. 13, p. 5188, 1976

[16] C. Keffer, T. M. Hayes, and A. Bienenstock, "PbTe Debye-Waller Factors and Band-Gap Temperature Dependence," *Phys. Rev. Lett.*, vol. 21, p.1676, 1968.

[17] A. Gobel, T. Ruf, M. Cardona, C.T. Lin, J. Wrzesinski, M. Steube, K. Reimann, J.C. Merle, and M. Joucla, "Effects of the isotopic composition on the fundamental gap of CuCl," *Phys. Rev.* ***B***, vol. 57, p. 15183, 1998.

[18] H. J. Lian, A. Yang, M. L. W. Thewalt, R. Lauck, and M. Cardona, "Effects of sulfur isotopic composition on the band gap of PbS," *Phys. Rev.* ***B***, vol. 73, p. 233202, 2006.

[19] M. Cardona, "Electron–phonon interaction in tetrahedral semiconductors," *Solid State Communications,* vol. 133, p. 3, 2005.

[20] H. Y. Fan, "Temperature dependence of the energy gap in semiconductors," *Phys. Rev.*, vol. 82, p. 900, 1951.

[21] E. Antoncik, "On the theory of temperature shift of the absorption curve in non-polar crystals," *Czechosl Journ. Phys*., vol. 5, p. 499, 1955.

[22] M. Cardona, T. A. Meyer, and M. L. W. Thewalt, "Temperature dependence of the energy gap of semiconductors in the low-temperature limit," *Phys. Rev. Lett.*, vol. 92, p.196403, 2004.

[23] Y. P. Varshni, "Temperature dependence of the energy gap in semiconductors," *Physica*, vol. 34, p. 149, 1967.

[24] H. Alawadhi, S. Tsoi, X. Lu, A. K. Ramdas, M. Grimsditch, M. Cardona, and R. Lauck, "Effect of temperature on isotopic mass dependence of excitonic band gaps in semiconductors: ZnO," *Phys. Rev.* ***B***, vol. 75, p. 205207, 2007.

[25] J. M. Zhang, T. Ruf, R. Lauck, and M. Cardona, "Isotope effects on exciton energies in CdS," *Phys. Rev.* ***B***, vol. 57, p. 9716, 1998.

[26] H. J. Monkhorst and J. D. Pack, "Special points for Brillouin-zone integrations," *Phys. Rev.* ***B***, vol. 13, p. 5188, 1976.

[27] Y. Zhao and D. J. Weidner, "Thermal expansion of $SrZrO_3$ and $BaZrO_3$ perovskites," *Phys. Chem. Miner.*, vol. 18, p. 294, 1991.

[28] R.J.Hill and I. Jackson, "The thermal expansion of ScAlO3—A silicate perovskite analogue," *Phys. Chem. Miner.*, vol. 17, p. 89, 1990.

[29] G. Fiquet, D. Andrault, A. Dewaele, T. Charpin, M. Kunz, and D. Haüsermann, "P-V-T equation of state of MgSiO3 perovskite," *Phys. Earth Planet. Inter.*, vol. 105, p. 21, 1998.

[30] A. R. Oganov, J. P. Brodholt, and G. David Price, "Comparative study of quasiharmonic lattice dynamics, molecular dynamics and Debye model applied to MgSiO3 perovskite," *Phys. Earth Planet. Inter.*, vol. 122, p. 277, 2000.

[31] W. Limmer, H. Leiderer, K. Jakob, W. Gebhardt, W. Kauschke, A. Cantarero, and C. Trallero-Giner, "Resonant Raman scattering by longitudinal-optical phonons in $Zn_{1-x}Mn_xSe$ (x=0, 0.03,0.1) near the E_0 gap," *Phys. Rev.* ***B***, vol. 42, p. 11325, 1990.

[32] S. Nomura and T. Kobayashi, "Exciton–LO-phonon couplings in spherical semiconductor microcrystallites," *Phys. Rev.* ***B***, vol. 45, p. 1305, 1992.

[33] A. G. Rolo and M. I. Vasilevskiy, "Raman spectroscopy of optical phonons confined in semiconductor quantum dots and nanocrystals," *J. Raman Spectrosc.*, vol. 38, p. 618, 2007.

[34] C. Thomsen and S. Reich, "Double resonant Raman scattering in graphite," *Phys. Rev. Lett.*, vol. 85, p. 5214, 2000.

[35] M. Souza, A. Jorio, C. Fantini, B. R. A. Neves, M. A. Pimenta, R. Saito, A. Ismach, E. Joselevich, V. W. Brar, Ge G. Samsonidze, G. Dresselhaus, and M. S. Dresselhaus, "Single-and double-resonance Raman G-band processes in carbon nanotubes," *Phys. Rev.* ***B***, vol. 69, p. 241403, 2004.

[36] A. Alexandrou, M. Cardona, and K. Ploog, "Doubly and triply resonant Raman scattering by LO phonons in GaAs/AlAs superlattices," *Phys. Rev.* ***B***, vol. 38, p. 2196, 1988.

[37] H. Schneider, J. Wagner, K. Fujiwara, and K. Ploog, "Triply resonant Raman scattering by LO phonons in a Wannier-Stark ladder," *Phys. Rev.* ***B,*** vol. 42, p. 11430, 1990.

[38] H. Lange, M. Artemyev, U. Woggon, T. Niermann, and C. Thomsen, "Experimental investigation of exciton-LO-phonon couplings in CdSe/ZnS core/shell nanorods," *Phys. Rev B,* vol. 77, p. 193303, 2008

[39] T. D. Krauss and F. W. Wise, "Coherent acoustic phonons in a semiconductor quantum dot," *Phys. Rev.* ***B***, vol. 55, p. 9860, 1997.

[40] J. L. M. van Mechelen, D. van der Marel, C. Grimaldi, A. B. Kuzmenko, N. P. Armitage, N. Reyren, H. Hagemann, and I. I. Mazin, "Electron-Phonon Interaction and Charge Carrier Mass Enhancement in $SrTiO_3$," *Phys. Rev. Lett.,* , vol. 100, p. 226403, 2008

[41] Y. Girshberg, and Y. Yacoby, "Ferroelectric phase transitions and off-centre displacements in systems with strong electron-phonon interaction," *J. Phys.: Condens. Matter,* vol. 11, p. 9807, 1999

[42] R. M. Martin and L. M. Falicov, "Resonant raman scattering," *Light Scattering in Solids I, Appl. Phys.,* vol. 8, p. 79, 1983

[43] A. Garcia-Cristabal, A. Cantarero, C. Trallero-Giner, and M. Cardona, "Excitonic model for second-order resonant Raman scattering," *Phys. Rev.* ***B***, vol**.** 49, p. 13430, 1994.

[44] R. Zeyher, "Calculation of resonant second-order Raman efficiencies for allowed and forbidden scattering," *Phys. Rev.* ***B***, vol. 9, p. 4439**,** 1974.

[45] D. Strauch and B. Borner, "Phonon dispersion in GaAs," *J. Phys.:Condens. Matter*, vol. 2, p. 1457, 1990

[46] A. Leitenstorfer, C. Fürst, A. Laubereau, W. Kaiser, G. Tränkle, and G. Weimann, "Femtosecond carrier dynamics in GaAs far from equilibrium," *Phys. Rev. Lett***.**, **,** vol**.** 76, p. 1545, 1996

[47] V. I. Klimov, D. W. McBranch, C. A. Leatherdale, and M. G. Bawendi, "Electron and hole relaxation pathways in semiconductor quantum dots," *Phys. Rev.* ***B***, vol. 60, p. 13740, 1999.

[48] T. C. Damen, Jagdeep Shah, D. Y. Oberli, D. S. Chemla, J. E. Cunningham, and J. M. Kuo, "Dynamics of exciton formation and relaxation in GaAs quantum wells," *Phys. Rev.* ***B***, vol. 42, p. 7434, 1990.

[49] A. Lemaître, A. D. Ashmore, J. J. Finley, D. J. Mowbray, M. S. Skolnick, M. Hopkinson, and T. F. Krauss, "Enhanced phonon-assisted absorption in single InAs/GaAs quantum dots," *Phys. Rev.* ***B***, vol. 63, p. 161309, 2001.

[50] R. Heitz, M. Veit, N. N. Ledentsov, A. Hoffmann, D. Bimberg, V. M. Ustinov, P. S. Kop'ev, and Zh I. Alferov, "Energy relaxation by multiphonon processes in InAs/GaAs quantum dots," *Phys. Rev.* ***B***, vol. 56, p. 10435, 1997.

[51] H. Htoon, M. J. O'Connell, S. K. Doorn, and V. I. Klimov, "Single carbon nanotubes probed by photoluminescence excitation spectroscopy: The role of phonon-assisted transitions," *Phys. Rev. Lett.*, vol. 94, p. 127403, 2005.

[52] R. H. Dicke, "Coherence in spontaneous radiation processes," *Phys. Rev.*, vol. 93, p. 99, 1954.

[53] Nicholas E.Rehler and Joseph H.Eberly, "Superradiance," *Phys. Rev. **A***, vol. 3, p. 1735, 1971.

[54] P. Vledder, A. V. Akimov, and J. I. Dijkhuis, "Transport of superradiant excitons in GaAs single quantum wells", *Phys. Rev. **B***, vol. 56, p. 15282, 1997.

[55] J. Feldmann, G. Peter, E. O. Göbel, P. Dawson, K. Moore, C. Foxon, and R. J. Elliott, "Linewidth Dependence of radiative exciton Lifetimes in Quantum Wells," *Phys. Rev. Lett.*, vol. 60, pp. 243–243, 1988

[56] M. Scheibner, T. Schmidt, L. Worschech, A. Forchel, G. Bacher, T. Passow and D. Hommel, "Superradiance in quantum dots," *Nature Physics*, vol. 3, pp. 106 – 110, 2007

[57] S. H. Lim, T. G. Bjorklund, F. C. Spano and C. J. Bardeen, "Exciton delocalization and superradiance in Tetracene Thin film and Nanoaggregates," *Phys. Rev. Lett.*, vol. 92, p. 107402, 2004

[58] K. Baumann, C. Guerlin, F. Brennecke and T. Esslinger, "Dicke quantum phase transition with a superfluid gas in an optical cavity," *Nature*, vol. 464, p. 1301, 2010.

[59] S. De. Boer, K. J. Vink and D. A. Wiersma, "Optical dynamics of condensed molecular aggregates: an accumulated photon-echo and hole-burning study of the J-aggregate," *Chem. Phys. Lett.*, vol. 137, pp. 99-106, 1987.

[60] S. De. Boer and D. A. Wiersma, "Dephasing-induced damping of superradiant emission in J-Aggregates," *Chem. Phys. Lett.*, vol. 165, pp. 45-53, 1990.

[61] S. Inouye, A. P. Chikkatur, D. M. Stamper-Kurn, J. Stenger, D. E. Pritchard and W. Ketterle, "Superradiant Rayleigh Scattering from a Bose-Einstein Condensate," *Science*, vol. 285, pp. 571-574, 1999.

[62] G. Björk, S. Pau, J. Jacobson and Y. Yamamoto, "Wannier exciton superradiance in a quantum well microcavity," *Phys. Rev.* ***B***, vol. 50, p. 17336, 1994.

[63] G. Björk, S. Pau, J. Jacobson, H. Cao and Y. Yamamoto, "Excitonic superradiance to exciton-polariton crossover and the pole approximations," *Phys. Rev.* ***B***, vol. 52, p. 17310, 1995.

[64] J. Knoester, "Optical dynamics in crystal slabs: Crossover from superradiant excitons to bulk polaritons," *Phys. Rev. Lett.*, vol. 68, p. 654, 1992.

[65] A. V. Kavokin and J. J. Baumberg, "Exciton-light coupling in quantum wells: From motional narrowing to superradiance," *Phys. Rev.* ***B***, vol. 57, p. 12697, 1998.

[66] E. Akkermans, A. Gero and R. Kaiser, "Photon localization and Dicke superradiance in atomic gases," *Phys. Rev. Lett.*, vol. 101, p. 103602, 2008.

[67] C. Cao, H. Cao and Y. Liu, "Quantum statistical theory of fluorescence of low density Frenkel excitons in a crystal slab," *Phys. Rev.* ***B***, vol. 62, p. 16453, 2000.

[68] R. Bonifacio and L. A. Lugiato, "Cooperative radiation processes in two-level systems: superfluorescence," *Phys.Rev.* ***A***, vol. 11, pp. 1507-1521, 1975.

[69] V. V. Zheleznyakov, V. V. Kocharovskiĭ and V. V. Kocharovskiĭ, "Polarization waves and superradiance in active media," *Soviet physics uspekhi*, vol. 32, pp. 835-870, 1989.

[70] Y. D. Jho, X. Wang, J. Kono, D. H. Reitze, X. Wei, A. A. Belyanin, V. V. Kocharovsky, Vl. V. Kocharovsky and G. S. Solomon, "Cooperative Recombination of a Quantized High-Density Electron-Hole Plasma in Semiconductor Quantum Wells," *Phys. Rev. Lett.*, vol. 96, p. 237401, 2006.

[71] Y. D. Jho, X. Wang, D. H. Reitze, J. Kono, A. A. Belyanin, V. V. Kocharovsky, Vl. V. Kocharovsky, and G. S. Solomon, "Cooperative recombination of electron-hole pairs in semiconductor quantum wells under quantizing magnetic fields," *Phys. Rev.* ***B***, vol. 81, p. 155314, 2010.

[72] G. T. Noe II, J. H. Kim, J. Lee, Y. Wang, A. K. Wójcik, S. A. McGill, D. H. Reitze, A. A. Belyanin and J. Kono, "Giant superfluorescent bursts from a semiconductor magneto-plasma," *Nature Physics*, vol. 8, pp. 219-224, 2012.

[73] L. Allen and J. H. Eberly, "optical resonance and two-level atoms," John Wiley & Sons, New York, 1975.

[74] V. V. Temnov and U. Woggon, "Superradiance and subradiance in an inhomogeneously broadened ensemble of two-level systems coupled to a low-Q cavity," *Phys. Rev. Lett.*, vol. 95, p. 243602, 2005.

[75] D. Mobius and H. Kuhn, "Energy transfer in monolayers with cyanine dye Sheibe aggregates," *J. Appl. Phys.*, vol. 64, p. 5138, 1988.

[76] F. C. Spano, J. R. Kuklinski and S. Mukamel, "Temperature-dependent superradiant decay of excitons in small aggregates," *Phys. Rev. Lett.*, vol. 65, p. 211, 1990.

[77] M. Paillard, X. Marie, E. Vanelle, T. Amand, V. K. Kalevich, A. R. Kovsh, A. E. Zhukov and V. M. Ustinov, "Time-resolved photoluminescence in self-assembled

InAs/GaAs quantum dots under strictly resonant excitation," *Appl. Phys. Lett.*, vol. 76, pp. 76-78, 2000.

[78] A. Yamamoto, T. Kido, T. Goto, Y. Chen, T. Yao and A. Kasuya, "Time-resolved photoluminescence in ZnO epitaxial thin films studied by up-conversion method," J. Cryst. Growth, vol. 214–215, pp. 308-311, 2000.

[79] K. Shum, Y. Takiguchi, J. M. Mohaidat, R. R. Alfano, K. Adomi and H. Morkoc, "Effect of valence-subband structure on the energy relaxation dynamics of electrons in GaAs quantum wells grown on Si," *Phys. Rev.* ***B***, vol. 44, p. 4044, 1991.

[80] Kenichiro Tanaka, T. Takahashi, T. Kondo, T. Umebajashi, K. Asai, K. Ema, "Image charge effect on two-dimensional excitons in an inorganic-organic quantum-well crystal," *Phys. Rev.* ***B***, vol. 71, p. 045312, 2005.

[81] G. Lanty, J. S. Lauret, E. Deleporte, S. Bouchoule, and X. Lafosse, "UV polaritonic emission from a perovskite-based microcavity," *Appl. Phys. Lett.*, vol. 93, p. 081101, 2008.

[82] S. Zhang, G. Lanty, J. S. Lauret, E. Deleporte, P. Audbert, and L. Galmiche, "Synthesis and optical properties of novel organic–inorganic hybrid nanolayer structure semiconductors," *Acta Materialia*, vol. 57, p. 3301, 2009.